

**MODELING AND INVERSION OF SCATTERED
SURFACE WAVES**

**MODELING AND INVERSION OF SCATTERED
SURFACE WAVES**

Proefschrift

ter verkrijging van de graad van doctor
aan de Technische Universiteit Delft,
op gezag van de Rector Magnificus prof. dr. ir. J.T. Fokkema,
voorzitter van het College voor Promoties,
in het openbaar te verdedigen
op dinsdag 1 september 2005 om 15.30 uur

door

Christina Dwi RIYANTI

Magister Sains Matematika,
Institut Teknologi Bandung, Indonesië
geboren te Bantul, Yogyakarta, Indonesië.

Dit proefschrift is goedgekeurd door de promotor:

Prof. dr. ir. A.J. Hermans

Toegevoegd promotor:

Dr. ir. G. C. Herman

Samenstelling Promotiecommissie:

Rector Magnificus	voorzitter
Prof. dr. ir. A.J. Hermans	Technische Universiteit Delft, promotor
Dr. ir. G.C. Herman	Shell International & Technische Universiteit Delft, toegevoegd promotor
Prof. dr. ir. A.W. Heemink	Technische Universiteit Delft
Prof. dr. ir. C.P.A. Wapenaar	Technische Universiteit Delft
Prof. dr. W.A. Mulder	Shell International & Technische Universiteit Delft
Prof. dr. J. Virieux	Université de Nice-Sophia Antipolis, France
Dr. Wono Setya Budhi	Bandung Institute of Technology, Indonesia

Dit onderzoek is financieel ondersteund door STW

ISBN 90-8559-076-0

Copyright © 2005 by Christina Dwi Riyanti.

All rights reserved. No part of this publication may be reproduced, stored in a retrieval system or transmitted in any form or by any means, electronic, mechanical, photocopying, recording or otherwise, without the prior written permission of the author.

Typesetting system: L^AT_EX 2_ε

Printed in The Netherlands by: Optima Grafische Communicatie

to my parents

Contents

1	Introduction	1
1.1	Motivation	1
1.2	Seismic Wave Field Modeling	2
1.3	Inversion of (Scattered) Surface Waves	5
1.4	Our Approach	6
1.4.1	Modeling	6
1.4.2	Inversion	6
1.5	Outline of this Thesis	7
2	Propagation and Scattering in the Near Subsurface	9
2.1	Introduction	9
2.2	Geometry of the Problem	10
2.3	Integral Representation of the Wave Field	11
2.3.1	Elastodynamic Equations in the Space-Frequency Domain	11
2.3.2	Reciprocity Theorem	12
2.3.3	Domain-Integral Representation of the Wave Field	14
2.4	Numerical Solution of the Integral Equation	20
2.5	Acceleration of the Computation of the Green's Tensor	23
2.6	Parallel Computing Implementation	26
2.7	Summary and Conclusion	27
3	Numerical Results for the Scattering Problem and Comparison with Experimental Data	31
3.1	Validation of the Layered Half-Space Green's Tensor	32
3.2	Results for a Simple Model	34
3.3	Results for a Random Scattering Distribution	38
3.4	Results for a Thin Layer with a Random Scatterer Distribution	41
3.5	Results for High-Velocity Contrasts in a Low-Velocity Background	44
3.6	Results for a Source at the Surface	45
3.6.1	Result for Three Scatterers	45
3.6.2	Comparison with Laboratory Experiments	48
4	The Inverse Problem for Scattered Surface Waves	51
4.1	Introduction	51
4.2	Formulation of the Inverse Problem	51
4.3	Conjugate Gradient Method	54

4.4	Inversion Algorithm	56
5	Numerical Results for the Inverse Problem	59
5.1	Results for a Small-Contrast Model	59
5.1.1	Description of the Model	59
5.1.2	Inversion Using a Single Frequency versus Several Frequencies	61
5.1.3	Effect of Parameterization	63
5.2	Results for a Strong-Contrast Model	65
5.2.1	Description of the Model: Weak Contrast (Case 1) versus Strong Contrast (Case 2)	65
5.2.2	Inversion Using a Single Frequency versus Several Frequencies	65
5.2.3	Effect of Parameterization	68
5.2.4	Comparing the Results to the Born Approximation and the Effect of Interaction Between Different Components	70
5.3	Imaging Examples Using the Born Approximation	72
6	Conclusion and Discussion	77
	Bibliography	79
A	Fourier Transforms	85
B	Derivation of the Green's Tensor for a Layered Medium	87
B.1	Solution of the Differential Equation	90
C	The Expression of the Free-Space Green's Tensor in the Spatial and the Slowness Domain	93
D	Calculation of the Green Matrix	95
D.1	Evaluation of the Elements of $\mathbf{B}_{ik}^{(m,n)}$	95
D.2	Evaluation of the Elements of $\mathbf{A}_{ik}^{(m,n)}$	96
D.2.1	The Integration of the Green Matrix over the z -Direction.	97
D.2.2	Evaluation of the Non-Diagonal Elements of $\mathbf{A}_{ik}^{(m,n)}$	100
D.2.3	Evaluation of the Diagonal Elements of $\mathbf{A}_{ik}^{(m,m)}$	101
E	Derivation of the Adjoint Operator $G_{\mathcal{D}}^{\dagger}$	103
F	List of Symbols	105
	Summary	107
	Samenvatting	109
	Acknowledgements	111

Curriculum Vitae

113

Introduction

Seismic waves provide important information about the interior of the Earth on various scales. This information is used extensively for the exploration of oil and gas, to study the evolution of the Earth, and to predict earth quakes, for example. More recently, the use of seismic waves for near-subsurface characterization in the field of geotechnical engineering has gained increased interest.

In seismic exploration, an image is made of the subsurface structure, which may indicate possible occurrences of hydrocarbon reservoirs. In a similar way, seismic records in solid Earth seismology are used to infer the structure of the entire Earth. In essence, those problems are *inverse* problems. In inverse problems seismic data are used to infer certain properties of the medium through which the waves propagate.

Often, the complexity of the seismic wave field does not allow direct interpretation of the data. For this reason, *forward* modeling methods are used to understand and predict wave propagation in the Earth. In forward modeling, the response from a known model is determined to a known source wave field, using a mathematical model for wave propagation.

In this thesis we discuss both the modeling and inversion of seismic waves that are guided along the surface of the Earth and are scattered in the vicinity of the source or the receivers.

1.1 Motivation

In seismic exploration, measurements of the elastic wave field are used, measured at the surface of the Earth, to make inferences about the first few kilometers of the Earth's crust. The objective of these methods is to obtain a detailed image of the subsurface in order to locate possible hydrocarbon-bearing layers. To obtain an image of the target area (in the deeper subsurface) the information is used contained in body waves that have traveled through the medium to a reflector and have been reflected back to the surface.

The seismic wave field is excited by a source at (or close to) the surface. Consequently, most of the energy is converted into surface waves. Surface waves are waves that are guided along the surface of the Earth. Hence, by definition, these surface waves do not carry information about the deeper subsurface. Because emphasis is placed on body waves in seismic imaging, surface waves are considered to be noise. For this reason, (scattered) surface waves have extensively

been studied to identify their properties and formulate schemes to remove them (Regone, 1998; Blonk and Herman, 1994; Herman and Perkins, 2004).

Another cause of noise in seismic exploration is the near-surface region which is often heterogeneous. This heterogeneity causes time shifts and amplitude anomalies in upcoming reflection events, potentially diminishing the quality of the final image. If the heterogeneity is strong enough and close to the surface, surface waves can also be excited when upcoming body waves impinge on near-surface heterogeneities or nearby topography (Gilbert and Knopoff, 1960; Hudson, 1967; Snieder, 1987; Wagner and Langston, 1992; Aki and Richards, 2002; Campman et al., 2005). In this case, the scatterer acts as a source and excites secondary surface waves. While the body-to-surface wave scattering mechanism has been well-documented in global seismology (Bannister et al., 1990; Wagner and Langston, 1992, for example), it has gone fairly unnoticed in seismic exploration.

In the past decade, new acquisition hardware became available, such that it has become possible to record the wave field at many more locations (see Figure 1.1). The denser sampling of the wave field has provided new insights in the seismic wave field and offers greater flexibility in processing of the data. From studying densely sampled data, it has become clear that scattering close to the receivers causes diffractions that can be tracked along at least a few traces in the record. Berni and Roeber (1989) and Muyzert and Vermeer (2004) show that perturbations on an intra-array scale can reduce the high-frequency content of the traces after stacking. This potentially diminishes the maximum obtainable resolution in the final image of the deeper subsurface. To get more insight in the nature of the effect of heterogeneity close to the surface, to help developing methods to correct for it, we have developed a method to model near-receiver scattering problems described in the present thesis.

While, on the one hand this model allows us to identify the main properties of near-surface scattering, on the other it can be used as the starting point for an inversion algorithm. Instead of being noise, the scattered surface waves then provide information about certain properties of the near subsurface. Applications of inversion of scattered surface waves may be found in geotechnical engineering, archeology, or water exploration (for instance Kaslilar et al., 2005).

1.2 Seismic Wave Field Modeling

In general, there are several different methods for simulating wave propagation. Carcione et al. (2002) distinguish three commonly used approaches: direct methods (finite difference methods, pseudospectral methods, and finite-element methods), integral-equation methods and ray-tracing methods. Direct methods like finite-difference methods (Robertsson et al., 1994; Robertsson and Holliger, 1997; Carcione et al., 2002) and finite-element methods (Hughes, 1987; Padovani et al., 1994; Séron et al., 1990) can in principle handle any geometry, by including topography for example, but they can also be very expensive computationally. For instance, in the case of the modeling of small inclusions in shallow layers, as in near-surface scattering,

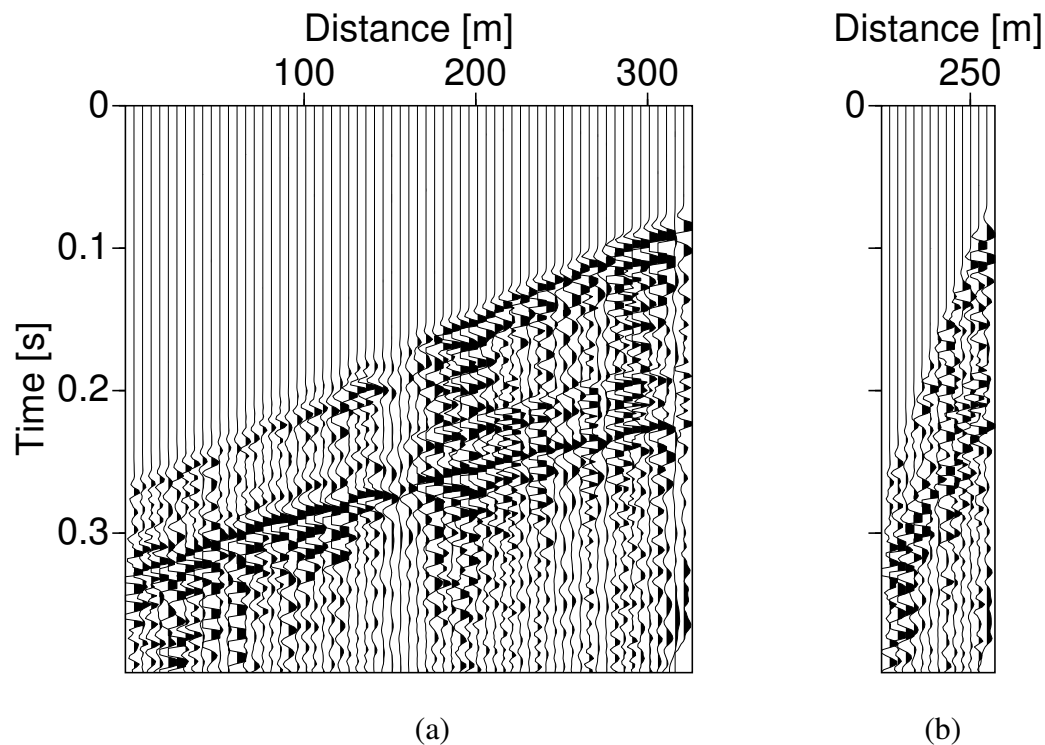


Figure 1.1: (a) Part of a single-receiver field record with dense spatial sampling. One can identify near-receiver scattering, showing up as the diffractions and interference between 125 and 175 m and around 40 m. (b) The same record, but representative for a conventional survey. This record was created from the one in (a) by summing five neighboring traces (group forming). Data courtesy of Schlumberger Cambridge Research/WesternGeco.

refining the grid can dramatically increase the computation time, especially in three dimensions. Asymptotic methods (e.g. Snieder, 1987; Blonk and Herman, 1994; Ernst and Herman, 1998) are very efficient, but when the scattering takes place close to the source or receivers, these methods are not accurate because they are based on a high-frequency approximation, which makes them only applicable for modeling problems in the far field.

Asymptotic methods are generally based on a single scattering approximation, which implies that the scattering objects have to be small compared to the dominant wavelength and that the contrast should be weak. Clearly, in a complex overburden, these conditions are not always met, which makes these methods unsuitable for this problem.

Seismic *surface* waves have been studied extensively in global seismology to explain certain arrivals in seismic records. They often dominate seismic recordings and can provide information about the near-surface structure of the Earth. In exploration seismology, surface waves are considered to be noise (Regone, 1998; Blonk and Herman, 1994; Herman and Perkins, 2004). In areas with rough topography (Hudson, 1967; Snieder, 1987; Aki and Richards, 2002) or with

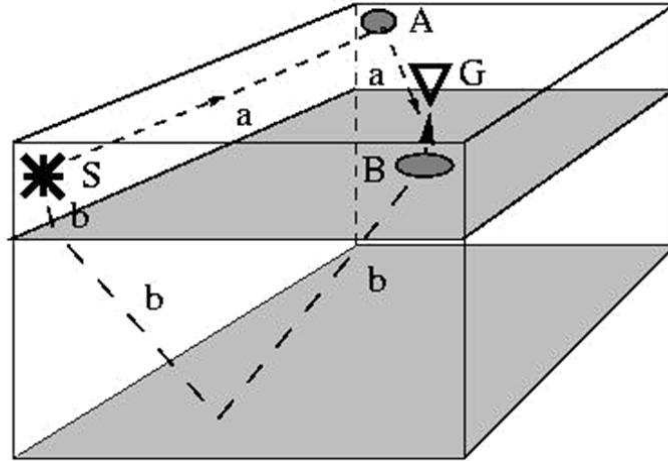


Figure 1.2: *Illustration of two types of near-surface scattering mechanisms. A is a heterogeneity far from the source, S, and receiver G; shot-generated surface waves travel along path a and are scattered at A. This is a form of side-scattered or additive noise. B is a heterogeneity directly beneath the receiver. Body waves travel along path b and are reflected by deeper layers. Each reflection recorded by G passes through B and excites (scattered) surface waves.*

a strongly heterogeneous shallow subsurface, these shot-generated guided waves can be scattered by near-surface heterogeneity or by surface topography.

In most cases, surface-wave scattering has been studied as a process independent from body waves. Up to date, surface-wave scattering has usually been studied assuming that the scattered waves are observed far away from the scattering domain (Snieder, 1987; Blonk and Herman, 1994; Ernst and Herman, 1998). However, when the scattering takes place close to the receiver, the behavior of the wave field close to the scatterer plays a more important role. It requires more computational effort to take this behavior into account. In this thesis, we develop a method that takes into account the near-field behavior of elastic scattering.

Furthermore, we look at the interaction between body waves and Rayleigh waves. This mechanism has been studied in the context of scattering of teleseismic P -waves that are converted into Rayleigh waves by topographical reliefs as observed in data from a dense array of seismometers in South Norway (Wagner and Langston, 1992). To explain this phenomenon, Clouser and Langston (1995) use the T-matrix method for a relatively simple 1D model with top-

graphical relief, while Hesttholm and Ruud (1998) use a finite difference method with explicit free-surface boundary conditions. Incorporation of the surface topography is not considered in this thesis; here we focus on body wave to surface wave scattering by near-surface heterogeneities. Combee (1994, 1995) discusses the scattering problem of scalar acoustic waves by such heterogeneities for a 2D near-surface model. The elliptical form of the scattering domain allowed him to present analytical solutions. While it is insightful from the point of view of statics estimation, his study does not include conversion of body waves into surface waves.

1.3 Inversion of (Scattered) Surface Waves

Most current methods for the inversion of surface waves are aimed at inverting dispersion curves. These methods are based on the dispersive property surface waves propagating in a layered medium, i.e. different frequencies travel with different phase velocities (Aki and Richards, 2002). One of the inherent assumptions of such analysis is that the waves propagate in a laterally homogeneous (flat layered) medium. While this is often a reasonable approximation of the Earth's structure (considering the wavelengths involved), at shallower depths, these assumptions can be violated due to the complexity of the near-surface region. Because of this plane-layer assumption, dispersion methods are not directed at characterizing local heterogeneities.

More recently, scattered surface waves have been used for imaging near-surface heterogeneities. On a global seismic scale, Snieder (1987) formulated a method to image scattered surface waves. A similar approach was taken by Blonk and Herman (1994). Snieder (1987) and Blonk and Herman (1994) showed that it is possible to image large surface obstacles far away from the sources and receivers using scattered surface waves.

Often, one is interested in heterogeneities in the shallow subsurface. To this end, methods have been developed that exploit certain effects of scattering on the surface wave (in order to infer the location of underground tunnels, for example). Park et al. (1998) use the fact that heterogeneities cause a different phase velocity and attenuation in a linear ground roll event to identify heterogeneities. Leparoux et al. (2000) apply the same type of processing but also try to bring out the scattered Rayleigh wave, to use it as a direct indicator of the spatial location of heterogeneity. A method based on wave theory was proposed by Herman et al. (2000) and extended by Campman et al. (2005) to actually image heterogeneities close to a receiver line or areal grid, by spatial and temporal deconvolution of scattered surface waves. While seismic reflection techniques are not designed for shallow imaging, surface waves require less dense sampling, which makes them potentially more suitable for near-surface characterization. Because near-surface heterogeneities can be close to the receivers, for these we also need to take into account the near-field behavior of the elastic Green's function.

1.4 Our Approach

1.4.1 Modeling

In this thesis we are interested in the modeling and inversion of surface waves scattered close to the receivers. In this case, the near-field behavior of the Green's function has to be taken into account, making the problem unsuitable for high-frequency asymptotic analysis. In Section 1.2, we identified two problems associated with conventional methods: accuracy and efficiency.

Although the use of integral equation methods is somewhat more limited than the above mentioned methods, they are known to be especially efficient and accurate for specific geometries, such as bounded objects in a (laterally) homogeneous embedding (Herman, 1982; De Hoop, 1995; Muijres and Herman, 2000; Carcione et al., 2002; Van den Berg, 2002).

For this reason, we use an integral-equation formulation in the frequency domain. Using elastic reciprocity, we derive an integral representation for the scattered field. The integral representation contains the Green's function of a layered embedding medium. We derive this Green's tensor in the slowness domain. To obtain the wave field in the spatial domain, we subject the Green's tensor to an inverse spatial Fourier transformation. To avoid a double spatial Fourier transformation, we use cylindrical symmetry to express the Green's function in terms of one slowness parameter. When the source and receiver locations are close to each other, the Fourier integral can converge slowly due to the slowly oscillating integrand. This problem is overcome by subtracting a function with the same asymptotic behavior as the layered medium Green's tensor from the slowness domain representation. In this way, the wavenumber range of integration is drastically reduced. We use the free-space Green's tensor for this purpose. Because we formulate our algorithm in the frequency domain, it is well suited for parallelization.

This algorithm serves as the point of departure for our inversion algorithm.

1.4.2 Inversion

Using the forward modeling scheme developed in this thesis, we formulate an inversion algorithm for scattered surface waves. We use a conjugate gradient method to update the contrast such that it minimizes a cost functional that consists of the actual scattered data and the scattered data calculated with our forward model. We use this algorithm to study sensitivities and the potential for retrieving actual parameters of the contrasting domain. Furthermore, we compare it to a similar algorithm which is based on the Born approximation and a seismic data processing algorithm that uses an approximation to the elastic wavefield.

1.5 Outline of this Thesis

The first objective of this thesis is to develop an efficient and accurate modeling method for scattering of elastic waves by $3D$ near-surface heterogeneities close to the observers. The second is to develop an inversion scheme for determining properties of near-surface heterogeneities in a given background model using scattered surface waves.

The outline of this thesis can be summarized as follows: The current chapter, **Chapter 1**, serves to introduce the subject of near-surface scattering of elastic waves and to motivate our research.

Chapter 2 is concerned with the general concepts of wave propagation and scattering of elastic waves in a laterally homogeneous embedding in which bounded objects with contrasting elastic properties are present. We derive an integral representation of the wave field using elastodynamic reciprocity. The integral representation can be expressed as a superposition of the wave field in the background without heterogeneity (the incident wave field) and a term that accounts for the presence of the heterogeneity (the scattered wave field). For positions inside the scattering domain, this leads to a domain integral equation of the second kind, involving the impulse response (Green's tensor) of the embedding, a contrast function, and the unknown field in the domain occupied by the scatterer. The field at any position can be calculated after solving the domain integral equation numerically using the method of moments.

In **Chapter 3**, we validate the Green's tensor for a horizontally layered medium by comparing it to that for a homogeneous half space. After validation of the Green's tensor, some numerical results illustrating scattering by near-surface heterogeneities are shown. We also validate our results, comparing them to experimental data collected on a laboratory-scale model.

Chapter 4 addresses the non-linear inverse problem for scattered surface waves. It is our objective to estimate the properties of near-surface heterogeneity, given the scattered field at the surface. The inversion is based on minimizing an error function consisting of the squared difference between the actual scattered field and that calculated with the integral representation developed in Chapter 2. The inverse problem is non-linear because the wave field in the scattering domain depends on the properties of the heterogeneity. We apply the conjugate-gradient method for estimating the properties of the heterogeneity (contrast function) by iteratively minimizing the cost functional.

In **Chapter 5**, we present numerical results of the inversion algorithm developed in Chapter 4. We address issues relating to the number of frequencies taken into account during the minimization and to the depth resolution of the inversion results. We compare the results obtained with our algorithm with those obtained with algorithms that use approximations to the scattered elastic wave field. Finally, we present imaging examples using the Born approximation inversion approach.

Finally, in **Chapter 6**, we give general conclusions concerning the forward modeling method and the inversion method. This chapter also recommends possible extensions of the inversion method for large-scale scattering problems.

The appendices in this thesis are mainly related to the theory as presented in Chapter 2 and

Chapter 4. In **Appendix A**, the definition of the Fourier transformations is introduced as a starting point for solving the near-surface scattering problem. **Appendix B** addresses the derivation of the Green's tensor for particle displacement $u_{ij}^G(\mathbf{x}, \mathbf{x}^s)$ for a horizontally layered medium with a source at location \mathbf{x}^s . In **Appendix C** we derive the expression of the free-space Green's tensor in the slowness domain, which we need to accelerate the computation of the Green's tensor. In **Appendix D**, we show in detail how to calculate the elements of the Green matrix $\mathbf{G}_{ik}^{(m,n)}$, discussed in Chapter 2. Finally, in **Appendix E**, we derive the adjoint operator, which is required in the conjugate-gradient scheme.

Propagation and Scattering in the Near Subsurface

2.1 Introduction

Wave propagation in the near subsurface can be described in terms of the particle displacement and stress in an elastic, three-dimensional, traction-free, layered half space. The particle displacement and stress satisfy the equation of motion and the equation of deformation of a solid. We consider propagation and scattering of elastic waves in a laterally homogeneous embedding in which bounded objects with contrasting elastic properties are present.

The wave field is represented as a superposition of the wave field in the embedding (or background) without heterogeneity (the incident wave field) and a term that accounts for the presence of the heterogeneity (the scattered wave field). Inside the scattering domain, this leads to a domain-integral equation of the second kind, involving the Green's tensor of the embedding, a contrast function and the unknown field in the domain occupied by the scatterer. We use the method of moments to determine the wave field inside the scattering domain. The wave field at the surface can then be calculated from the discretized integral representation.

In order to solve the integral equation efficiently, we first derive the slowness-domain Green's tensor for a layered half space in terms of Bessel functions (Kennett, 1983, 2001). By carrying out a slowness transformation, we obtain the space-time domain of the Green's tensor. We accelerate the convergence of the computation of the Green's tensor by subtracting a term that can be integrated analytically from the Green's tensor. Since the problem is formulated in the frequency domain, it is well suited for straightforward parallelization on a multi-processor system. A parallel computing approach can reduce the calculation time for solving the integral equation by distributing the calculation over different CPUs. The implementation was done in a Fortran program with MPI message passing (Gropp et al., 1994; Pacheco, 1997).

2.2 Geometry of the Problem

We use coordinates $\mathbf{x} = (x_1, x_2, x_3) \equiv (x, y, z)$ with respect to the origin O to locate a point in a stationary reference frame. The unit vectors along the coordinate axes are given by $\mathbf{i}_1, \mathbf{i}_2, \mathbf{i}_3$. The subscript notation is used for vectors and tensors. For repeated lower subscripts, the summation convention is understood, e.g., $x_i y_i = x_1 y_1 + x_2 y_2 + x_3 y_3$. Furthermore, ∂_i indicates the partial derivative with respect to the x_i -coordinate, where $i = \{1, 2, 3\}$. The time of observation is denoted by t , and the partial derivative with respect to t is denoted by ∂_t (no summation).

We consider propagation and scattering of elastic waves in a laterally homogeneous embedding in which bounded objects with contrasting elastic properties are present. The embedding (background) consists of a stack of L horizontal layers overlying a homogeneous, isotropic, elastic half-space. It occupies the domain Ω , given by $\Omega = \{\mathbf{x} = (x_1, x_2, x_3) \in \mathbb{R}^3 \mid -\infty < x_1, x_2 < \infty, x_3 \geq 0\}$. The unit vector \mathbf{i}_3 is directed vertically downwards. The surface of Ω is bounded by a traction-free surface ($x_3 = 0$), which is denoted by \mathcal{S} . The geometry of the problem is shown in Figure 2.1. This figure shows a 3D near-surface model with heterogeneity. The heterogeneity occupies the domain $\mathcal{D} = \{(x_1, x_2, x_3) \in \mathbb{R}^3 \mid x_1^0 \leq x_1 \leq x_1^0 + W_x, x_2^0 \leq x_2 \leq x_2^0 + W_y, 0 \leq x_3 \leq H, (x_1^0, x_2^0) \in \mathbb{R}^2\}$, with H the depth and W_x, W_y the length and width of the scatterer, respectively.

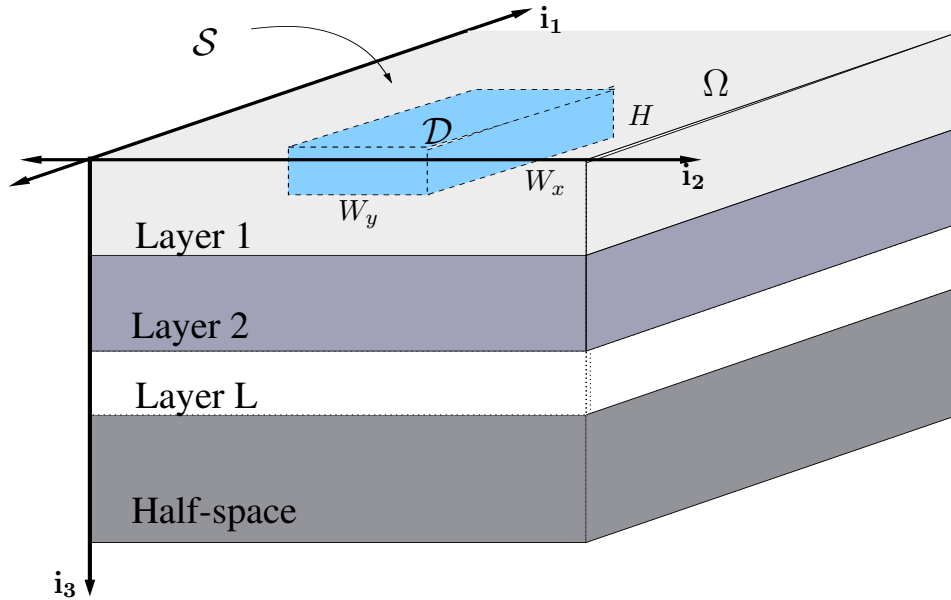


Figure 2.1: The geometry of the problem of a 3D near-surface model with an embedded heterogeneity \mathcal{D} in the layered half space.

2.3 Integral Representation of the Wave Field

We start with the equation of motion and the equation of deformation of the elastic solid. We assume that the changes in the elastic medium due to wave propagation are small enough for the medium to behave linearly. We first derive an elastodynamic reciprocity theorem from these linearized equations. The reciprocity theorem interrelates two non-identical elastodynamic states occupying the same domain. We then choose the actual wave field and the Green's state for the first and second states, respectively. The Green's state is the wave field in the embedding caused by an impulsive point force. The result of the interrelation between the actual and the Green's state is a domain-type integral representation for the particle displacement of the wave field.

2.3.1 Elastodynamic Equations in the Space-Frequency Domain

The basic equations consist of the equation of motion and the equation of deformation of an elastic solid (Kennett, 1983; De Hoop, 1995; Aki and Richards, 2002). In the time domain, their linearized form is given by:

$$\Delta_{ijpq} \partial_j \tau_{pq}(\mathbf{x}, t) - \rho(\mathbf{x}) \partial_t^2 u_i(\mathbf{x}, t) = -f_i(\mathbf{x}, t), \quad (2.1)$$

$$\Delta_{ijpq} \partial_p u_q(\mathbf{x}, t) - s_{ijpq}(\mathbf{x}) \tau_{pq}(\mathbf{x}, t) = -h_{ij}(\mathbf{x}, t). \quad (2.2)$$

where

- $u_j(\mathbf{x}, t)$: particle displacement (m),
- $\tau_{ij}(\mathbf{x}, t)$: stress tensor (Pa),
- $\rho(\mathbf{x})$: volume density of mass of the elastic solid (kg/m^3),
- $s_{ijpq}(\mathbf{x})$: compliance tensor of the elastic solid (Pa^{-1}),
- $f_j(\mathbf{x}, t)$: volume density of the body force (N/m^3),
- $h_{ij}(\mathbf{x}, t)$: volume density of deformation rate (dimensionless).

In equation (2.1), Δ_{ijpq} is the symmetrical unit tensor of rank four, defined as (De Hoop, 1995):

$$\Delta_{ijpq} = \frac{1}{2}(\delta_{ip}\delta_{jq} + \delta_{iq}\delta_{jp}), \quad (2.3)$$

with δ_{ij} the Kronecker delta symbol given by:

$$\delta_{ij} = \begin{cases} 1 & \text{if } i = j, \\ 0 & \text{if } i \neq j. \end{cases} \quad (2.4)$$

These equations are supplemented with the traction-free boundary condition:

$$n_j \tau_{ij}(\mathbf{x}, t) = f_i^S(\mathbf{x}, t) \quad \mathbf{x} \in \mathcal{S} \quad (i = 1, 2, 3), \quad (2.5)$$

where n_j is the unit vector along the normal pointing away from the medium.

The i -th component of the particle velocity is given by

$$v_i(\mathbf{x}, t) = \partial_t u_i(\mathbf{x}, t) \quad (i = 1, 2, 3). \quad (2.6)$$

Furthermore, as there are no sources at infinity, the wavefield at large distances from the sources (f_i , f_i^S and h_{ij}) consists only of waves propagating away from the sources.

Applying the Fourier transformation (given in Appendix A) to equation (2.1)-(2.2), we obtain:

$$\Delta_{ijpq} \partial_j \widehat{\tau}_{pq}(\mathbf{x}, \omega) + \omega^2 \rho(\mathbf{x}) \widehat{u}_i(\mathbf{x}, \omega) = -\widehat{f}_i(\mathbf{x}, \omega), \quad (2.7)$$

$$\Delta_{ijpq} \partial_p \widehat{u}_q(\mathbf{x}, \omega) - s_{ijpq}(\mathbf{x}) \widehat{\tau}_{pq}(\mathbf{x}, \omega) = -\widehat{h}_{ij}(\mathbf{x}, \omega), \quad (2.8)$$

where ω [rad/s] denotes angular frequency. In these equations, $\widehat{\tau}_{pq}$, \widehat{u}_i , \widehat{f}_i and \widehat{h}_{ij} are the frequency-domain counterparts of τ_{pq} , u_i , f_i and h_{ij} , respectively.

The stress-free boundary condition in the frequency-domain is given by

$$n_j \widehat{\tau}_{ij}(\mathbf{x}, \omega) = \widehat{f}_i^S(\mathbf{x}, \omega) \quad (\mathbf{x} \in \mathcal{S}). \quad (2.9)$$

The particle velocity in the frequency domain is given by

$$\widehat{v}_i(\mathbf{x}, \omega) = -j\omega \widehat{u}_i(\mathbf{x}, \omega). \quad (2.10)$$

From now on, we will consider frequency-domain quantities and omit the hat over the field quantities for convenience.

2.3.2 Reciprocity Theorem

Following Fokkema and Van den Berg (1993) and De Hoop (1995), we employ the Betti-Rayleigh reciprocity theorem of the convolution type. The domain Ω is bounded by the boundary surface $\partial\Omega$ (see Figure 2.2). The reciprocity theorem serves as a starting point for our derivation of the domain-type integral representation of the wave field in terms of the particle displacement, generated by a source at position \mathbf{x}^s and observed at position \mathbf{x} . We introduce two different states inside the domain, referred to as state A and state B. Table 2.1 shows how each state is characterized by the elastodynamic wave field quantities (τ_{ij}, u_j), the constitutive parameters (ρ, s_{ijpq}) and the source terms (f_i, h_{ij}).

Let state A be the state corresponding to the equations

$$\Delta_{ijpq} \partial_j \tau_{pq}^A(\mathbf{x}, \omega) + \omega^2 \rho^A(\mathbf{x}) u_i^A(\mathbf{x}, \omega) = -f_i^A(\mathbf{x}, \omega), \quad (2.11)$$

$$\Delta_{ijpq} \partial_p u_q^A(\mathbf{x}, \omega) - s_{ijpq}^A(\mathbf{x}) \tau_{pq}^A(\mathbf{x}, \omega) = -h_{ij}^A(\mathbf{x}, \omega), \quad (2.12)$$

supplemented with the boundary condition

$$n_j \tau_{ij}^A(\mathbf{x}, \omega) = f_i^{S,A}(\mathbf{x}, \omega) \quad (\mathbf{x} \in \mathcal{S}). \quad (2.13)$$

	State A	State B
Field State	τ_{ij}^A, u_i^A	τ_{ij}^B, u_i^B
Material state	ρ^A, s_{ijpq}^A	ρ^B, s_{ijpq}^B
Source state	f_i^A, h_{ij}^A	f_i^B, h_{ij}^B
Boundary condition	$f_i^{\mathcal{S},A}$	$f_i^{\mathcal{S},B}$
Domain Ω		

Table 2.1: States A and B of the elastodynamic reciprocity theorem.

Similarly, let state B be the state corresponding to the equations

$$\Delta_{ijpq} \partial_j \tau_{pq}^B(\mathbf{x}, \omega) + \omega^2 \rho^B(\mathbf{x}) u_i^B(\mathbf{x}, \omega) = -f_i^B(\mathbf{x}, \omega), \quad (2.14)$$

$$\Delta_{ijpq} \partial_p u_q^B(\mathbf{x}, \omega) - s_{ijpq}^B(\mathbf{x}) \tau_{pq}^B(\mathbf{x}, \omega) = -h_{ij}^B(\mathbf{x}, \omega), \quad (2.15)$$

supplemented with the boundary condition

$$n_j \tau_{ij}^B(\mathbf{x}, \omega) = f_i^{\mathcal{S},B}(\mathbf{x}, \omega) \quad (\mathbf{x} \in \mathcal{S}). \quad (2.16)$$

Let $\partial_i (\tau_{pq}^A u_j^B - \tau_{pq}^B u_j^A)$ be the local interaction quantity between elastodynamic states A and B in a solid occupying domain Ω . Using standard rules for spatial differentiation, we can write the interaction quantity as

$$\begin{aligned} \Delta_{ijpq} \partial_i (\tau_{pq}^A u_j^B - \tau_{pq}^B u_j^A) &= (\Delta_{ijpq} \partial_i \tau_{pq}^A) u_j^B + \tau_{pq}^A (\Delta_{ijpq} \partial_i u_j^B) \\ &\quad - (\Delta_{ijpq} \partial_i \tau_{pq}^B) u_j^A - \tau_{pq}^B (\Delta_{ijpq} \partial_i u_j^A). \end{aligned} \quad (2.17)$$

After substituting equations (2.11)-(2.15) into (2.17) and using the symmetry properties of the stress tensor ($\tau_{pq} = \tau_{qp}$), one obtains:

$$\begin{aligned} \partial_j (\tau_{ij}^A u_i^B - \tau_{ij}^B u_i^A) &= \omega^2 (\rho^B - \rho^A) u_i^A u_i^B + (s_{ijpq}^B - s_{pqij}^A) \tau_{ij}^A \tau_{pq}^B \\ &\quad - f_i^A u_i^B + f_i^B u_i^A + h_{ij}^B \tau_{ij}^A - h_{ij}^A \tau_{ij}^B. \end{aligned} \quad (2.18)$$

This relation is the local form of the reciprocity theorem.

Integrating the above equation over the domain Ω , which is bounded by $\partial\Omega$, and employing Gauss's divergence theorem, we obtain the global form of the reciprocity theorem of the

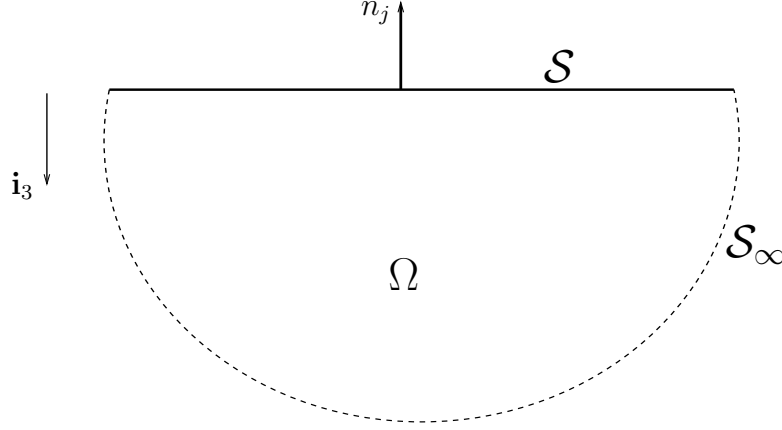


Figure 2.2: Configuration of domain Ω for the application of the reciprocity theorem. The boundary $\partial\Omega = \mathcal{S} \cup \mathcal{S}_\infty$.

convolution type

$$\int_{\partial\Omega} n_j \left[\tau_{ij}^A u_i^B - \tau_{ij}^B u_i^A \right] dA = \int_{\Omega} \left[\omega^2 (\rho^B - \rho^A) u_i^A u_i^B + (s_{ijpq}^B - s_{pqij}^A) \tau_{pq}^B \tau_{ij}^A - f_i^A u_i^B + f_i^B u_i^A + h_{ij}^B \tau_{ij}^A - h_{ij}^A \tau_{ij}^B \right] dV, \quad (2.19)$$

where the normal n_j is pointing outward (see Figure 2.2).

The boundary $\partial\Omega$ consists of two parts, i.e., the boundary surface \mathcal{S} and the boundary of the semi-sphere \mathcal{S}_∞ (Figure 2.2). As there are no sources at infinity, the boundary integral over \mathcal{S}_∞ vanishes at infinity. This is commonly referred to as the radiation condition (see Tan (1975), for example). On account of the radiation condition, we can replace $\partial\Omega$ by \mathcal{S} in the boundary integral of relation (2.19). Substituting the boundary conditions (2.13) and (2.16) into relation (2.19), we obtain

$$\int_{\mathcal{S}} \left[f_i^{\mathcal{S},A} u_i^B - f_i^{\mathcal{S},B} u_i^A \right] dA = \int_{\Omega} \left[\omega^2 (\rho^B - \rho^A) u_i^A u_i^B + (s_{ijpq}^B - s_{pqij}^A) \tau_{pq}^B \tau_{ij}^A - f_i^A u_i^B + f_i^B u_i^A + h_{ij}^B \tau_{ij}^A - h_{ij}^A \tau_{ij}^B \right] dV, \quad (2.20)$$

which is also known as the Betty-Rayleigh reciprocity theorem. This theorem is the basis of our derivation of the domain-integral representation of the wave field.

2.3.3 Domain-Integral Representation of the Wave Field

The reciprocity theorem discussed in the previous section provides a relation between displacements, traction components and body forces for two different states. We now derive the domain-integral representation of the wave field of the layered elastic half space using the reciprocity

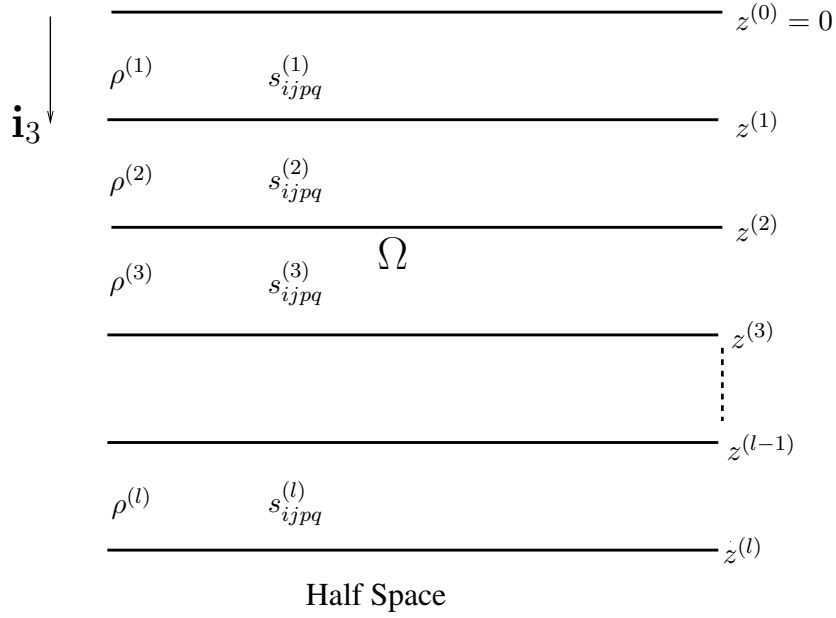


Figure 2.3: Configuration of layered embedding medium Ω for the application of the reciprocity theorem. The density and the compliance tensor of the l -th layer are denoted by $\rho^e(\mathbf{x}) = \rho^e(z) = \rho^{(l)}$ and $s_{ijpq}^e(\mathbf{x}) = s_{ijpq}^e(z) = s_{ijpq}^{(l)}$ for $z^{(l-1)} < z < z^{(l)}$, respectively.

theorem.

We first consider the embedding (background) consisting of a stack of L horizontal layers overlying a homogeneous, isotropic, elastic half space as shown in Figure 2.3. For each of these L layers, propagation of disturbances is governed by the equation of motion and the equation of deformation given in equations (2.7) and (2.8). By taking $h_{ij}(\mathbf{x}, \omega) = 0$, we obtain

$$\Delta_{ijpq} \partial_j \tau_{pq}(\mathbf{x}, \mathbf{x}^s, \omega) + \omega^2 \rho^e(\mathbf{x}) u_i(\mathbf{x}, \mathbf{x}^s, \omega) = -f_i(\mathbf{x}, \mathbf{x}^s, \omega), \quad (2.21)$$

$$\Delta_{ijpq} \partial_p u_q(\mathbf{x}, \mathbf{x}^s, \omega) - s_{ijpq}^e(\mathbf{x}) \tau_{pq}(\mathbf{x}, \mathbf{x}^s, \omega) = 0, \quad (2.22)$$

where \mathbf{x}^s is the position of the source.

For a horizontally stratified medium, the density and the compliance tensor are written as (see Figure 2.3):

$$\rho^e(\mathbf{x}) = \rho^e(z) = \rho^{(l)} \quad (z^{(l-1)} < z < z^{(l)}), \quad (2.23)$$

$$s_{ijpq}^e(\mathbf{x}) = s_{ijpq}^e(z) = s_{ijpq}^{(l)} \quad (z^{(l-1)} < z < z^{(l)}). \quad (2.24)$$

where l indicates the layer index ($l = 1, 2, \dots, L$), and the density and the compliance tensor of the l -th layer are denoted by $\rho^{(l)}$ and $s_{ijpq}^{(l)}$, respectively.

For isotropic elastic media, the compliance tensor $s_{ijpq}^{(l)}$ is expressed in terms of the Lamé

parameters $\lambda^{(l)}$ and $\mu^{(l)}$ (see Achenbach (1973) and De Hoop (1995)):

$$s_{ijpq}^{(l)} = -\frac{\lambda^{(l)}}{2\mu^{(l)}(3\lambda^{(l)} + 2\mu^{(l)})}\delta_{ij}\delta_{pq} + \frac{1}{4\mu^{(l)}}(\delta_{ip}\delta_{jq} + \delta_{iq}\delta_{jp}). \quad (2.25)$$

The stiffness tensor is related to the compliance tensor through:

$$c_{rsij}^{(l)}s_{ijpq}^{(l)} = \Delta_{rspq}, \quad (2.26)$$

where Δ_{rspq} is given by equation (2.3). The stiffness can be then expressed as:

$$c_{rsij}^{(l)} = \lambda^{(l)}\delta_{rs}\delta_{ij} + \mu^{(l)}(\delta_{ir}\delta_{js} + \delta_{is}\delta_{jr}). \quad (2.27)$$

Applying the symmetrical unit tensor of rank four given by equation (2.3) to equations (2.21) and (2.22) and multiplying equation (2.22) with the isotropic stiffness tensor $c_{pqij}^{(l)}$ for each layer, we obtain the equation of motion and a constitutive relation for the stress tensor (Kennett, 1983). In the frequency domain, these take the form:

$$\partial_i \tau_{ij}(\mathbf{x}, \mathbf{x}^s, \omega) + \omega^2 \rho^{(l)}(\mathbf{x}) u_j(\mathbf{x}, \mathbf{x}^s, \omega) = -f_j(\mathbf{x}, \mathbf{x}^s, \omega), \quad z^{(l-1)} < z < z^{(l)} \quad (2.28)$$

$$\tau_{ij}(\mathbf{x}, \mathbf{x}^s, \omega) = \lambda^{(l)} \delta_{ij} \partial_k u_k(\mathbf{x}, \mathbf{x}^s, \omega) + \mu^{(l)} (\partial_i u_j(\mathbf{x}, \mathbf{x}^s, \omega) + \partial_j u_i(\mathbf{x}, \mathbf{x}^s, \omega)), \quad (2.29)$$

where $\rho^{(l)}$ denotes the density of the l -th layer, while the Lamé parameters of the l -th layer are denoted by $\lambda^{(l)}$ and $\mu^{(l)}$ (for $l = 1, \dots, L$). The summation convention for lower subscripts is understood.

Pao and Varatharajulu (1976) and Lee and Mal (1995) have derived the integral representation for elastic scattering in a homogeneous medium in which the scattering objects differ from the embedding in both Lamé parameters and density. In this thesis, we concentrate on a layered embedding medium and only consider a density contrast. In this case, we have $s_{ijpq} = s_{ijpq}^e$. The method developed here, however, is also applicable to contrasts in Lamé parameters (*mutatis mutandis*).

Now, in order to derive a wave field representation from relation (2.19), we choose state A as the actual wave field ($u_j^A = u_j$, $\tau_{ij}^A = \tau_{ij}$, ρ) generated by a vertical stress source at location $\mathbf{x}^s = (x^s, y^s, z^s)$. These quantities satisfy the equations:

$$\Delta_{ijpq} \partial_j \tau_{pq}(\mathbf{x}, \mathbf{x}^s, \omega) + \omega^2 \rho^e(\mathbf{x}) u_i(\mathbf{x}, \mathbf{x}^s, \omega) = -f_i^A(\mathbf{x}, \mathbf{x}^s, \omega), \quad (2.30)$$

$$\Delta_{ijpq} \partial_p u_q(\mathbf{x}, \mathbf{x}^s, \omega) - s_{ijpq}^e(\mathbf{x}) \tau_{pq}(\mathbf{x}, \mathbf{x}^s, \omega) = 0, \quad (2.31)$$

where $f_i^A = (\rho(\mathbf{x}) - \rho^e(\mathbf{x}))\omega^2 u_i(\mathbf{x}, \mathbf{x}^s, \omega)$, with $\rho^e(\mathbf{x})$ the density of the embedding layered medium.

The boundary condition is given by:

$$n_j \tau_{ij}(\mathbf{x}, \mathbf{x}^s, \omega) = f_i^S(\mathbf{x}, \mathbf{x}^s, \omega) \quad (\mathbf{x} \in \mathcal{S}), \quad (2.32)$$

where

$$f_i^S(\mathbf{x}, \mathbf{x}^s, \omega) = W(\omega) \delta_{i3} \delta(x - x^s) \delta(y - y^s), \quad (2.33)$$

and where $W(\omega)$ denotes the source waveform. Apart from the boundary source, there are no volume sources present in state A.

State B represents the Green's state, which is the wave field in the embedding layered medium due to an impulsive point source at position $\mathbf{x}^r = (x^r, y^r, z^r)$. The Green's wave field quantities, (u_{ik}^G, τ_{ijk}^G) for $k = 1, 2, 3$, satisfy the equations:

$$\Delta_{ijpq} \partial_j \tau_{pqk}^G(\mathbf{x}, \mathbf{x}^r, \omega) + \omega^2 \rho^e(\mathbf{x}) u_{ik}^G(\mathbf{x}, \mathbf{x}^r, \omega) = -f_{ik}^G(\mathbf{x}, \mathbf{x}^r, \omega), \quad (2.34)$$

$$\Delta_{ijpq} \partial_p u_{qk}^G(\mathbf{x}, \mathbf{x}^r, \omega) - s_{ijpq}^e(\mathbf{x}) \tau_{pqk}^G(\mathbf{x}, \mathbf{x}^r, \omega) = 0, \quad (2.35)$$

where

$$f_{ik}^G(\mathbf{x}, \mathbf{x}^r, \omega) = \begin{cases} 0 & (\mathbf{x}^r \in \mathcal{S}), \\ \delta_{ik} \delta(x - x^r) \delta(y - y^r) \delta(z - z^r) & (\mathbf{x}^r \in \Omega). \end{cases} \quad (2.36)$$

The boundary condition is given by:

$$n_j \tau_{ijk}(\mathbf{x}, \mathbf{x}^r, \omega) = f_{ik}^{S,G}(\mathbf{x}, \mathbf{x}^r, \omega) \quad (\mathbf{x} \in \mathcal{S}), \quad (2.37)$$

where

$$f_{ik}^{S,G}(\mathbf{x}, \mathbf{x}^r, \omega) = \begin{cases} \delta_{ik} \delta(x - x^r) \delta(y - y^r) & (\mathbf{x}^r \in \mathcal{S}), \\ 0 & (\mathbf{x}^r \in \Omega). \end{cases} \quad (2.38)$$

The properties of the states A and B are summarized in Table 2.2.

Substituting state A and B into the reciprocity theorem (2.20) gives the following relation:

$$\begin{aligned} \int_{\mathbf{x} \in \mathcal{S}} \left[f_i^S(\mathbf{x}, \mathbf{x}^s) u_{ik}^G(\mathbf{x}, \mathbf{x}^r) - f_{ik}^{S,G}(\mathbf{x}, \mathbf{x}^r) u_i(\mathbf{x}, \mathbf{x}^s) \right] dA &= \int_{\mathbf{x} \in \Omega} \left[-f_i^A(\mathbf{x}, \mathbf{x}^s) \right. \\ &\quad \left. \times u_{ik}^G(\mathbf{x}, \mathbf{x}^r) + f_{ik}^G(\mathbf{x}, \mathbf{x}^r) u_i(\mathbf{x}, \mathbf{x}^s) \right] dV. \end{aligned} \quad (2.39)$$

In the above equation, for brevity we omit the dependence on ω of the field quantities and the source.

Substituting the source state and the boundary conditions for state A and B shown in Table 2.2 into the equation (2.39) yields for $\mathbf{x}^r \in \mathcal{S}$,

$$\begin{aligned} \int_{\mathbf{x} \in \mathcal{S}} \left[W(\omega) \delta_{i3} \delta(x - x^s) \delta(y - y^s) u_{ik}^G(\mathbf{x}, \mathbf{x}^r) - \delta_{ik} \delta(x - x^r) \delta(y - y^r) \right. \\ \left. u_i(\mathbf{x}, \mathbf{x}^s) \right] dA = \int_{\mathbf{x} \in \Omega} \left[-(\rho(\mathbf{x}) - \rho^e(\mathbf{x})) \omega^2 u_i(\mathbf{x}, \mathbf{x}^s) u_{ik}^G(\mathbf{x}, \mathbf{x}^r) \right] dV, \end{aligned} \quad (2.40)$$

	State A	State B
Field State	$\{\tau_{ij}, u_i\}(\mathbf{x}, \mathbf{x}^s, \omega)$	$\{\tau_{ijk}^G, u_{ik}^G\}(\mathbf{x}, \mathbf{x}^r, \omega)$
Material state	$\rho^e(\mathbf{x}), s_{ijpq}^e(\mathbf{x})$	$\rho^e(\mathbf{x}), s_{ijpq}^e(\mathbf{x})$
Source state	$f_i(\mathbf{x}, \mathbf{x}^s, \omega) = f_i^A$	$f_{ik}^G(\mathbf{x}, \mathbf{x}^r, \omega)$
Boundary condition	$f_i^S(\mathbf{x}, \mathbf{x}^s, \omega)$	$f_{ik}^{S,G}(\mathbf{x}, \mathbf{x}^r, \omega)$
Domain Ω		

Table 2.2: The actual state (A) and the Green's state (B) in the elastodynamic reciprocity theorem: $f_i^A = (\rho(\mathbf{x}) - \rho^e(\mathbf{x}))\omega^2 u_i(\mathbf{x}, \mathbf{x}^s, \omega)$ and $f_{ik}^G(\mathbf{x}, \mathbf{x}^r, \omega)$, $f_i^S(\mathbf{x}, \mathbf{x}^s, \omega)$ and $f_{ik}^{S,G}(\mathbf{x}, \mathbf{x}^r, \omega)$ are given by equations (2.36), (2.33) and (2.38), respectively.

and for $\mathbf{x}^r \in \Omega$, we have

$$\begin{aligned}
& \int_{\mathbf{x} \in \mathcal{S}} \left[W(\omega) \delta_{i3} \delta(x - x^s) \delta(y - y^s) u_{ik}^G(\mathbf{x}, \mathbf{x}^r) \right] dA = \\
& \int_{\mathbf{x} \in \Omega} \left[-(\rho(\mathbf{x}) - \rho^e(\mathbf{x}))\omega^2 u_i(\mathbf{x}, \mathbf{x}^s) u_{ik}^G(\mathbf{x}, \mathbf{x}^r) + \delta_{ik} \delta(\mathbf{x} - \mathbf{x}^r) u_i(\mathbf{x}, \mathbf{x}^s) \right] dV.
\end{aligned} \tag{2.41}$$

Furthermore, by employing the sifting property of the Dirac Delta function (Brigham, 1988) in the above equations, we arrive at the following integral representation:

$$\begin{aligned}
u_k(\mathbf{x}^r, \mathbf{x}^s) &= W(\omega) u_{k3}^G(\mathbf{x}^r, \mathbf{x}^s) + \omega^2 \int_{\mathbf{x} \in \Omega} (\rho(\mathbf{x}) - \rho^e(\mathbf{x})) \\
&\quad \times u_{ki}^G(\mathbf{x}^r, \mathbf{x}) u_i(\mathbf{x}, \mathbf{x}^s) dV, \quad (\mathbf{x}^r \in \Omega \cup \mathcal{S}).
\end{aligned} \tag{2.42}$$

Here, we have also used the symmetry relation (De Hoop, 1995):

$$u_{ik}^G(\mathbf{x}^s, \mathbf{x}^r) = u_{ki}^G(\mathbf{x}^r, \mathbf{x}^s). \tag{2.43}$$

From relation (2.42), we obtain the following representation for the wave field generated by a vertical stress source at position \mathbf{x}^s and recorded at position \mathbf{x} ($\mathbf{x} \in \Omega \cup \mathcal{S}$):

$$u_i(\mathbf{x}, \mathbf{x}^s) = W(\omega)u_{i3}^G(\mathbf{x}, \mathbf{x}^s) + \omega^2 \int_{\mathbf{x}' \in \Omega} (\rho(\mathbf{x}') - \rho^e(\mathbf{x}'))u_{ik}^G(\mathbf{x}, \mathbf{x}')u_k(\mathbf{x}', \mathbf{x}^s) dV. \quad (2.44)$$

Let

$$u_i^{inc}(\mathbf{x}, \mathbf{x}^s) = W(\omega)u_{i3}^G(\mathbf{x}, \mathbf{x}^s), \quad (2.45)$$

$$u_i^{sc}(\mathbf{x}, \mathbf{x}^s) = \omega^2 \int_{\mathbf{x}' \in \Omega} (\rho(\mathbf{x}') - \rho^e(\mathbf{x}'))u_{ik}^G(\mathbf{x}, \mathbf{x}')u_k(\mathbf{x}', \mathbf{x}^s) dV. \quad (2.46)$$

With these definitions, we can write the integral representation (2.44) as:

$$u_i(\mathbf{x}, \mathbf{x}^s) = u_i^{inc}(\mathbf{x}, \mathbf{x}^s) + u_i^{sc}(\mathbf{x}, \mathbf{x}^s). \quad (2.47)$$

The quantity u_i^{inc} is the incident wave field generated by the source in the layered embedding (without heterogeneity). The i^{th} component of the displacement, due to an impulsive point source pointing in the vertical direction, is denoted by u_{i3}^G . The quantity $u_i^{sc}(\mathbf{x}, \mathbf{x}^s)$ is the scattered wave field that accounts for the presence of the heterogeneity \mathcal{D} . Since the density contrast $\rho(\mathbf{x}') - \rho^e(\mathbf{x})$ vanishes outside \mathcal{D} , the integral (2.47) can be restricted to \mathcal{D} . Therefore, we get

$$u_i^{sc}(\mathbf{x}, \mathbf{x}^s) = \omega^2 \int_{\mathbf{x}' \in \mathcal{D}} (\rho(\mathbf{x}') - \rho^e(\mathbf{x}'))u_{ik}^G(\mathbf{x}, \mathbf{x}')u_k(\mathbf{x}', \mathbf{x}^s) dV. \quad (2.48)$$

Equation (2.48) is a domain-integral representation of the scattered wave field over the contrasting (scatterer) domain $\mathcal{D} \subset \Omega$. The density of the medium occupying the domain \mathcal{D} is denoted by $\rho(\mathbf{x}')$ and $\rho^e(\mathbf{x}')$ is the density of the embedding. The quantity $u_{ik}^G(\mathbf{x}, \mathbf{x}')$ denotes the Green's displacement tensor for the embedding medium. The derivation, as well as expressions for $u_{ik}^G(\mathbf{x}, \mathbf{x})$, are given in Appendix B.

The domain-type integral representation for the total wave field u_i can now be expressed as:

$$u_i(\mathbf{x}, \mathbf{x}^s) = u_i^{inc}(\mathbf{x}, \mathbf{x}^s) + \omega^2 \int_{\mathbf{x}' \in \mathcal{D}} \Delta\rho(\mathbf{x}')u_{ik}^G(\mathbf{x}, \mathbf{x}')u_k(\mathbf{x}', \mathbf{x}^s) dV, \quad (2.49)$$

where the contrast is $\Delta\rho(\mathbf{x}') = \rho(\mathbf{x}') - \rho^e(\mathbf{x}')$ and $\mathbf{x}, \mathbf{x}^s \in \Omega \cup \mathcal{S}$. Equation (2.49) is a Fredholm equation of the second kind.

From equation (2.49) it follows that, to determine the total wave field outside the scattering region, we first need to calculate the total wave field inside \mathcal{D} . To do so, we take $\mathbf{x} \in \mathcal{D}$ in equation (2.49), obtaining an integral equation of the second kind for the unknown field u_k .

In general, this integral equation can only be solved approximately with the aid of numerical techniques. One of these techniques is the method of moments (Harrington, 1968; Jarem, 1986; Rius et al., 1997), which is discussed in the next section.

2.4 Numerical Solution of the Integral Equation

With the aid of the properties of Dirac delta function, we can rewrite the integral equation (2.49) (with $\mathbf{x} \in \mathcal{D}$) in an integral operator form:

$$\mathcal{L}_{ik}u_k = u_i^{inc}, \quad (2.50)$$

where u_i^{inc} is the known function, u_k is the function to be determined, and \mathcal{L}_{ik} is an integral operator acting on a function u_k through the relation

$$\mathcal{L}_{ik}u_k = \int_{\mathbf{x}' \in \mathcal{D}} [\delta_{ik}\delta(\mathbf{x} - \mathbf{x}') - \omega^2 \Delta \rho(\mathbf{x}') u_{ik}^G(\mathbf{x}, \mathbf{x}')] u_k(\mathbf{x}', \mathbf{x}^s) dV, \quad (2.51)$$

where δ is the Dirac delta distribution, and δ_{ik} is the Kronecker delta.

The first step in applying the method of moments is discretization of the unknown field, u_k , in a sequence of expansion functions, $u^{(n)}$ with unknown coefficients $\{\alpha_k^{(n)}\}$:

$$u_k \approx u_k^{(M)} = \sum_{n=1}^M \alpha_k^{(n)} u^{(n)} \quad (k = 1, 2, 3). \quad (2.52)$$

Because the expansion of the wave field is truncated after M terms, a discretization error is introduced. Denoting the error between the left- and right-hand side of equation (2.50) by the residual $r_i^{(M)}$, we have

$$r_i^{(M)} = \mathcal{L}_{ik}u_k^{(M)} - u_i^{inc}. \quad (2.53)$$

We require the residual to be orthogonal to the test functions, $w^{(m)}$, i.e.,

$$\langle r_i^{(M)}, w^{(m)} \rangle = 0, \quad (m = 1, 2, \dots, M, i = 1, 2, 3), \quad (2.54)$$

where the inner product is defined as the integration of the product of two integrable functions, f and g , over the domain \mathcal{D} and is given by

$$\langle f, g \rangle = \int_{\mathbf{x} \in \mathcal{D}} f(\mathbf{x}) \bar{g}(\mathbf{x}) d\mathbf{x}, \quad (2.55)$$

where the overbar denotes complex conjugate.

After substituting equation (2.53) into equation (2.54) and using the properties of the inner product, we obtain a system of linear equations for the unknown $\{\alpha_k^{(n)}\}$ in the following form:

$$\sum_{n=1}^M \mathbf{G}_{ik}^{(m,n)} \alpha_k^{(n)} = h_i^{(m)} \quad m = 1, 2, \dots, M, \quad (2.56)$$

where

$$\mathbf{G}_{ik}^{(m,n)} = \langle \mathcal{L}_{ik}u^{(n)}, w^{(m)} \rangle, \quad (2.57)$$

and

$$h_i^{(m)} = \langle u_i^{inc}, w^{(m)} \rangle. \quad (2.58)$$

Now the coefficients $\{\alpha_k^{(n)}\}$ can be obtained by solving the system (2.56).

In order to calculate the matrix elements $\mathbf{G}_{ik}^{(m,n)}$ and the vector elements $h_i^{(m)}$, we first divide the scattering domain \mathcal{D} into subdomains, $\mathcal{D}^{(n)}$, with widths of Δ_x , Δ_y and Δ_z in the x , y and z directions, respectively:

$$\mathcal{D}^{(n)} = \left\{ (x, y, z) \in \mathbb{R}^3 \mid x^{(n)} - \frac{1}{2}\Delta_x < x < x^{(n)} + \frac{1}{2}\Delta_x, \right. \\ \left. y^{(n)} - \frac{1}{2}\Delta_y < y < y^{(n)} + \frac{1}{2}\Delta_y, z^{(n)} - \frac{1}{2}\Delta_z < z < z^{(n)} + \frac{1}{2}\Delta_z \right\}. \quad (2.59)$$

The discretization of the scattering domain \mathcal{D} is shown in Figure 2.4.

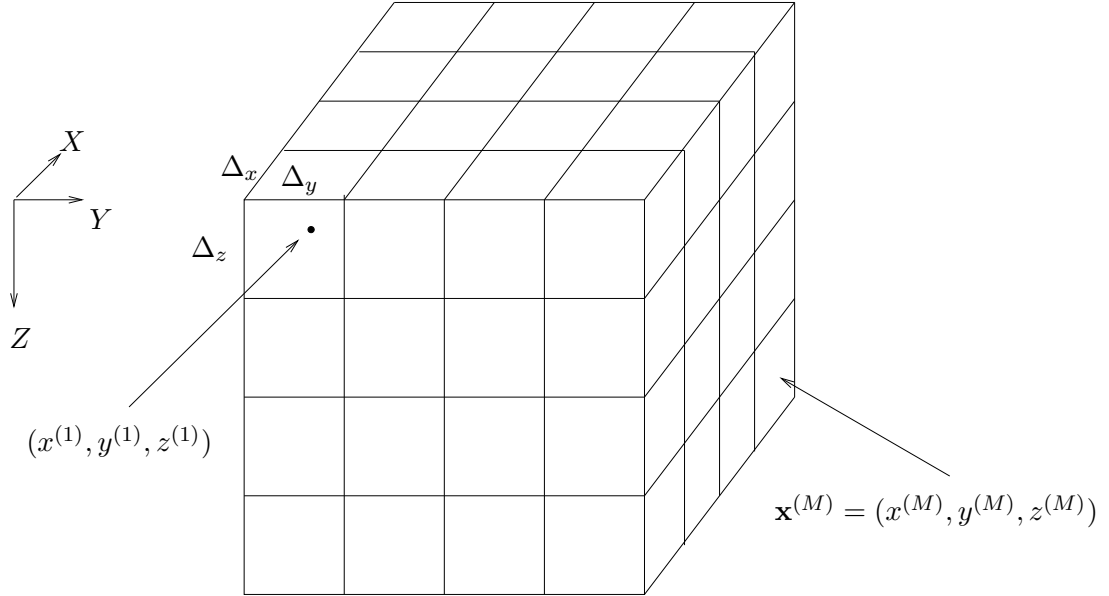


Figure 2.4: Discretization of the scattering domain \mathcal{D} .

In each subdomain $\mathcal{D}^{(n)}$, with center points at $\mathbf{x}^{(n)}$ ($n = 1, 2, \dots, M$), we assume the contrast $\Delta\rho$ to be piecewise constant:

$$\Delta\rho(\mathbf{x}) = \Delta\rho^{(n)} \quad (\mathbf{x} \in \mathcal{D}^{(n)}). \quad (2.60)$$

We now define the expansion function $u^{(n)}$ as

$$u^{(n)}(\mathbf{x}) = \begin{cases} 1 & (x, y, z) \in \mathcal{D}^{(n)}, \\ 0 & \text{otherwise,} \end{cases} \quad (2.61)$$

and the test functions $w^{(m)}$ ($m = 1, 2, \dots, M$) as

$$w^{(m)}(\mathbf{x}) = \delta(\mathbf{x} - \mathbf{x}^{(m)}). \quad (2.62)$$

Inserting $w^{(m)}$ from equation (2.62) into equations (2.57) and (2.58) and applying the definition of the inner product, given by equation (2.55), we can express the matrix elements and the vector elements in the following form:

$$\mathbf{G}_{ik}^{(m,n)} = \delta_{ik}\delta_{mn} - \omega^2 \Delta \rho_n \int_{\mathbf{x}' \in \mathcal{D}_n} u_{ik}^G(\mathbf{x}^{(m)}, \mathbf{x}') dx' dy' dz', \quad (2.63)$$

and

$$h_i^{(m)} = W_s(\omega) u_{i3}^G(\mathbf{x}^{(m)}, \mathbf{x}^s), \quad (2.64)$$

for $m, n = 1, 2, \dots, M$.

In equation (2.63), $u_{ik}^G(\mathbf{x}^{(m)}, \mathbf{x}')$ is the Green's tensor of the embedding medium in the space-frequency domain ($i, k = 1, 2, 3$).

An explicit expression for the Green's tensor, \tilde{u}_{ik}^G , for a layered half-space was derived by Ditzel et al. (2001) in the slowness-frequency domain using Cartesian slowness coordinates (p_1 and p_2). Subjecting this slowness-frequency domain Green's tensor, \tilde{u}_{ik}^G , to an inverse Fourier transform (see Appendix A) yields in the space-frequency domain the Green's tensor:

$$u_{ik}^G(\mathbf{x}^{(m)}, \mathbf{x}') = \frac{\omega^2}{4\pi^2} \int_{p_1} \int_{p_2} \tilde{u}_{ik}^G(p_1, p_2, z, \omega, z') e^{j\omega[p_1(x^{(m)}-x') + p_2(y^{(m)}-y')]} dp_1 dp_2. \quad (2.65)$$

Inserting the above equation into equation (2.63), we can numerically compute the integral over p_1 and p_2 , but the computation time is large due to the double integration over p_1 and p_2 (Riyanti and Herman, 2003). We can reduce this to one single integration using rotational symmetry. By introducing cylindrical coordinates related to (p_1, p_2) , Kennett (1983) derived the Green's tensor, \tilde{u}_{ik}^G , in terms of Bessel functions. This form of the Green's tensor can be found in Appendix B. Following Kennett, we can therefore rewrite in the form

$$\mathbf{G}_{ik}^{(m,n)} = \delta_{ik}\delta_{mn} - \omega^2 \Delta \rho_n \int_{\mathbf{x}' \in \mathcal{D}_n} \int_{p=0}^{\infty} \tilde{u}_{ik}^G(p; z^{(m)}; \omega; z') p dp dx' dy' dz', \quad (2.66)$$

with $\tilde{u}_{ik}^G(p; z^{(m)}; \omega; z')$ given by equations (B.45)-(B.47).

The use of the Green's tensor in terms of Bessel functions is the first step to accelerate the computation of the system matrix elements.

2.5 Acceleration of the Computation of the Green's Tensor

When the observation and the scatterer points are located close to each other, the integral (2.66) converges slowly because the integrand can decay slowly in the p -domain (Hisada, 1994). This could slow down the integration of the Green's tensor over the p -domain. To avoid this, we accelerate the computation of the Green's tensor by subtracting a term with the same behavior for large p , i.e., with the same asymptotic behavior, but which can be integrated analytically. We choose the free-space Green's tensor for this purpose (Zwamborn and Van den Berg, 1997). The analytical expression for the free-space Green's tensor is known both in the spatial domain (Harris, 2001) and slowness domain (Appendix C). By subtracting the free-space Green's tensor from the layered half-space Green's tensor in the slowness domain, the integrand decays more rapidly to zero. Consequently, the range of the integration can be significantly reduced. Adding the free-space Green's tensor in the spatial domain gives the same result as using equation (2.66).

The Green matrix can then be rewritten as follows:

$$\begin{aligned} \mathbf{G}_{ik}^{(m,n)} &= \delta_{ik}\delta_{mn} \\ &- \omega^2 \Delta \rho_n \int_{\mathbf{x}' \in \mathcal{D}_n} \left\{ \int_{p=0}^{\infty} [\tilde{u}_{ik}^G(p; z^{(m)}; \omega; z') - \tilde{g}_{ik}(p; z^{(m)}; \omega; z')] p dp \right. \\ &\left. + g_{ik}(\mathbf{x}^{(m)}; \omega; \mathbf{x}') \right\} dx' dy' dz', \end{aligned} \quad (2.67)$$

where g_{ij} is the free-space Green's tensor in the spatial domain given by equations (C.1)-(C.3), and \tilde{g}_{ij} is the free-space Green's tensor in the slowness domain given by equations (C.4)-(C.9).

To illustrate the acceleration of our method for the numerical computation of the layered medium Green's tensor in the p -domain, we consider a layered model that contains a layer overlying a half space. The properties of the layer and half space are summarized in Table 2.3.

	c_S (m/s)	c_P (m/s)	ρ (kg/m ³)	h (m)
Layer 1	1000	3000	1500	400
Half space	3100	6000	3000	∞

Table 2.3: *The parameters of the model.*

The thickness of the layer is 400 m. The observation point is located at 10 m depth, while the source point is located at 10.5 m depth. With this small depth separation, calculating the elements of the layered Green's tensor, \tilde{u}_{ik}^G , with equation (2.66) results in an integrand with

slowly decreasing amplitude (as observed by Hisada, 1994). This is shown in Figure 2.5(a)-(f) by the solid line. In the same Figure, we have plotted the free-space Green's tensor, \tilde{g}_{ik} , with the same material properties as the layer that includes the source. For large p values, these functions have the same behavior. The dashed line in Figure 2.5(a)-(f) represents the difference between the Green's tensor for the layered medium and the free-space Green's tensor, $\tilde{u}_{ik}^G - \tilde{g}_{ik}$, which is referred to as "difference". This difference occurs in the p -integral as the integrand in equation (2.67). The difference goes to zero after a p value of about 3 ms/m and therefore the p -integration can be reduced to a much smaller value than the one that would be required if equation (2.66) was used.

After evaluating $\mathbf{G}_{ik}^{(m,n)}$ (given in Appendix D) and $h_i^{(m)}$ in equation (2.64), we can solve the system of linear equations (equation (2.56)), from which we determine the expansion coefficients $\alpha_k^{(n)}$. Once we have obtained these coefficients, the total wave field inside the scatterer follows from the following relation:

$$u_k(\mathbf{x}) = \sum_{n=1}^M \alpha_k^{(n)} u^{(n)}(\mathbf{x}). \quad (2.68)$$

Finally, we can evaluate the total wave field at any location by evaluating the integral representation (2.49) with the aid of the midpoint rule.

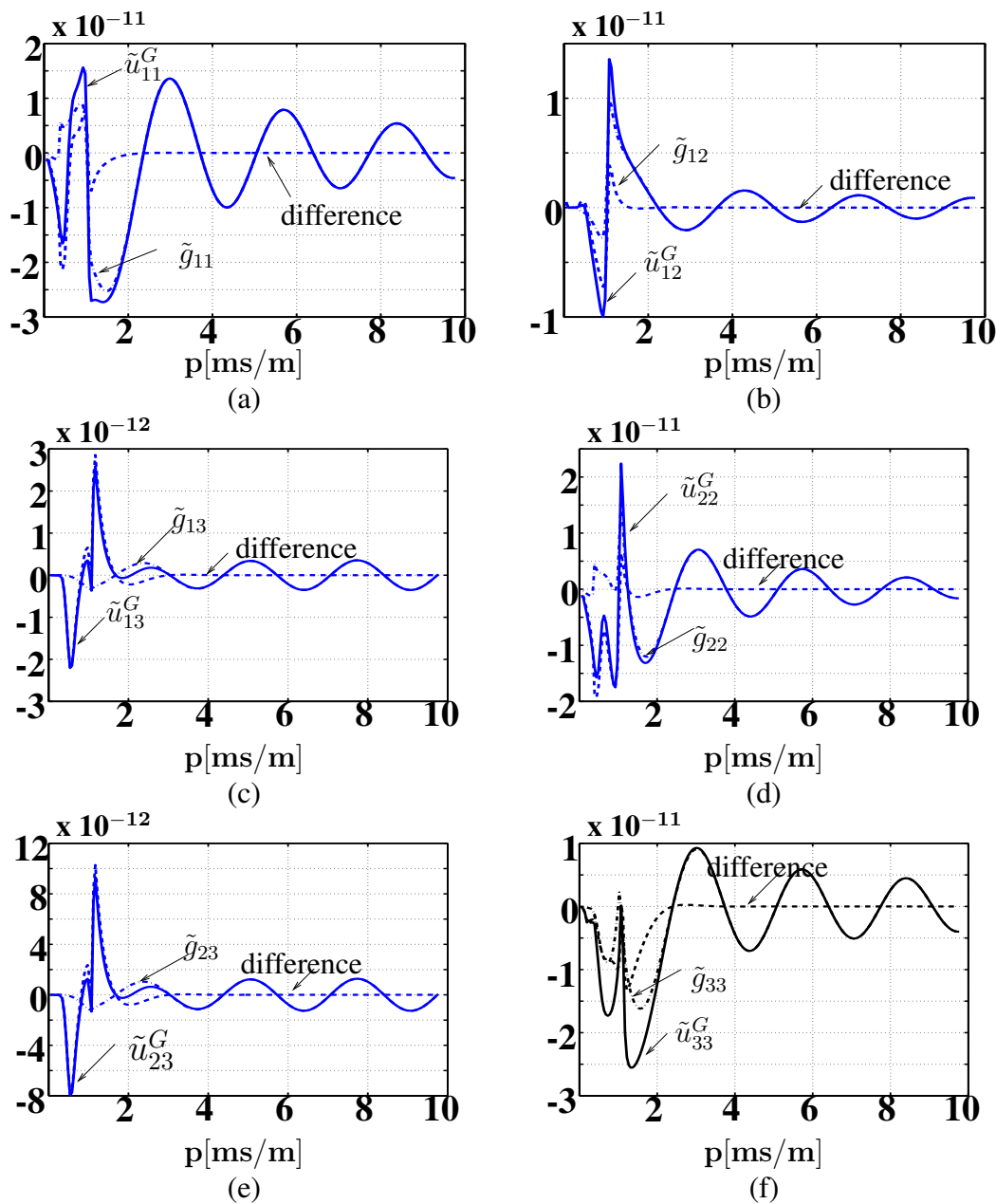


Figure 2.5: The Green's tensor elements 11 (a), 12 (b), 13(c), 22(d), 23(e), and 33(f) as functions of the slowness p for the frequency $f = 25$ Hz. The difference between the Green's tensor of the layered medium, \tilde{u}^G , and the free-space tensor, \tilde{g} , is represented by the dashed line. The free-space Green's tensor has the same material properties as the layer that includes the source. The observation point is located at 10 m depth, while the source point is located at 10.5 m depth.

2.6 Parallel Computing Implementation

We now focus on how to solve the system of linear equations efficiently. We have formulated the problem in the frequency domain, so that the method is well suited for straightforward parallelization on a multi-processor system. We can rewrite the system of linear equations for the unknown coefficients $\alpha_k^{(n)}$ (2.56) for each frequency as follows:

$$\sum_{n=1}^M \mathbf{G}_{ik}^{(m,n)} \alpha_k^{(n)} = h_i^{(m)} \quad n = 1, 2, \dots, M, \quad (2.69)$$

where $\mathbf{G}_{ik}^{(m,n)}$ is the Green matrix containing the elements of the Green's tensor (2.67) and $h_i^{(m)}$ is the vector containing the incident wave field (2.64). Directly storing and evaluating the Green matrix $\mathbf{G}_{ik}^{(m,n)}$ and solving for the unknown coefficients for all frequencies is very compute intensive if the number of cells is too large. In order to reduce the computation time needed to solve the equation, we now describe a parallel algorithm to solve this problem.

In the parallel implementation of the program, we supplemented the existing Fortran Code with MPI (Message-Passing Interface)-routines (Pacheco, 1997). Our algorithm is based on the master-slave paradigm (Rizk, 2003). If there are P processors and N_{freq} frequencies, then each processor computes the Green's tensor and the solution of the system's matrix for $n_p = \frac{N_{freq}}{P}$ frequencies. One processor (P_0) is the master and P_s , for $0 < s < P$, are the slaves. The master sends the input data to the slaves and receives the solution for $n_p(P-1)$ frequencies back from the slaves. By collecting the results from the slaves, we obtain the solution of the system for all frequencies.

The following pseudo-code gives an outline of the parallel computing algorithm:

```

if MASTER then
  do s=1,P-1
    send the input data to procesors  $P_s$  (slaves)
    receive the solution for  $n_p$  frequencies from each slave
  end do
  compute the Green's tensor and solve the system for  $n_p$  frequencies
  assemble the solution for all frequencies ( $N_{freq} = n_p \cdot P$ )
else if SLAVE then
  receive the input data from the MASTER
  compute the Green's tensor and solve the system for  $n_p$  frequencies
  send the solution of the system to the MASTER
end if
stop

```

The configuration of the cluster in this case is given in Figure 2.6.

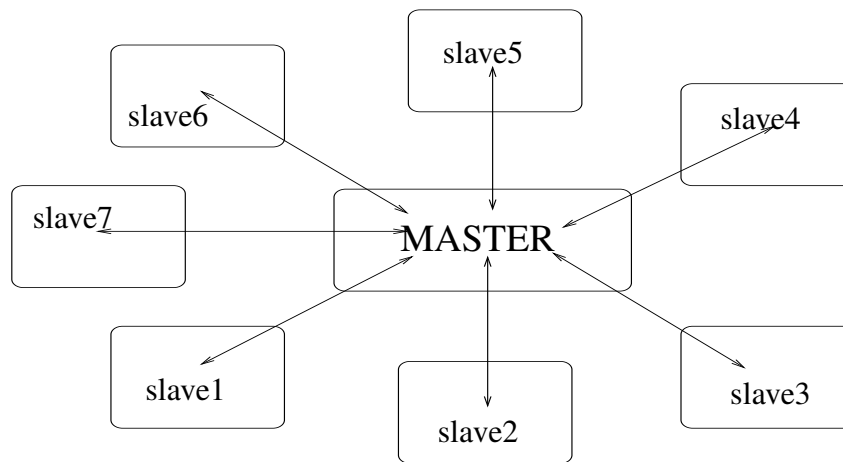


Figure 2.6: *The configuration used in the parallel version of the program.*

In order to illustrate the implementation of the parallel approach, we have calculated the Green's tensor in the slowness-frequency domain (given by equation (2.65)) using the same parameters as given in Table 2.3. The number of frequencies taken into account, is $N_{freq} = 48$. We use 8 AMD Athlon (TM) XP +2600 1.9 G processors. By increasing the number of processors, we compute the Green's tensor in the space-frequency domain with the help of the 2D Fast Fourier transform. First, we use $P = 1$, then $P = 2$, $P = 3$, $P = 4$, $P = 6$, and $P = 8$, respectively. Each processor calculates the Green's tensor for $n_p = \frac{N_{freq}}{P}$ frequencies. Parallel performance for 1 – 8 processors is shown in Figure 2.7. One can see from Figure 2.7 that as the number of processors increases, the computational time decreases linearly with $1/P$. However, for large number of processors ($P > 8$) linearity is usually not retained due to the increase of communication time between the nodes.

2.7 Summary and Conclusion

We have discussed a numerical method for solving the domain-integral equation for the wave field scattered by heterogeneities close to the surface of the Earth. We first expressed the wave field as a superposition of the incident wave field (without heterogeneity) and the scattered wave

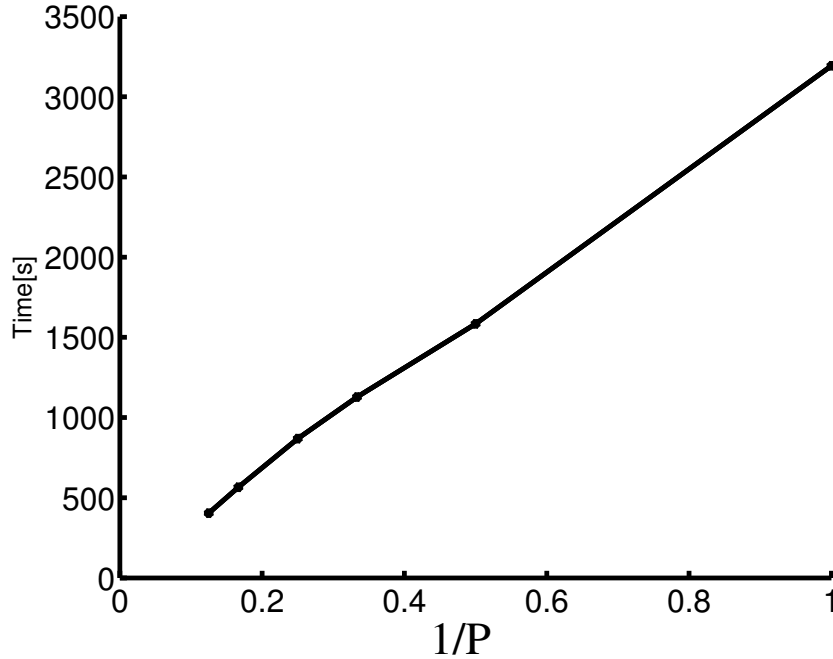


Figure 2.7: Parallel performance of the calculation of the Green's tensor in the space-time domain for 1 – 8 processors. The number of processors is denoted by P .

field that accounts for the presence of the heterogeneity.

For observation points inside the scattering domain, we obtained a domain-integral equation of the second kind, involving the impulse response (Green's tensor) of the embedding, a contrast function and the unknown wave field in the domain occupied by the scatterer. We applied the method of moments to solve this domain integral equation.

For each frequency, we obtained a system of linear equations for the unknown coefficients $\{\alpha_k^{(n)}\}$ in the following form,

$$\sum_{n=1}^M \mathbf{G}_{ik}^{(m,n)} \alpha_k^{(n)} = h_i^{(m)} \quad n = 1, 2, \dots, M, \quad (2.70)$$

where $\mathbf{G}_{ik}^{(m,n)}$ is the Green matrix containing the elements of the Green's tensor (2.66) and $h_i^{(m)}$ is the vector containing the incident wave field (2.64). We reduced the time for calculating the system matrix by considering the Green's tensor in terms of Bessel functions. We also presented a method for accelerating the convergence of the computation of the Green's tensor by subtracting the free-space Green's tensor when the observation and the scatterer points are located close to each other.

For each frequency, the coefficients $\{\alpha_k^{(n)}\}$ can be obtained by solving the system of linear

equations (2.70). The resulting frequency-domain method can be run very efficiently on a cluster of workstations since each frequency is computed independently. We have made a parallel implementation of the program, using MPI. This parallel approach not only reduced the computation time; it can also handle larger scattering problems.

Numerical Results for the Scattering Problem and Comparison with Experimental Data

In this chapter, we present numerical results illustrating scattering by near-surface heterogeneities. We calculate the vertical component of the particle velocity at the surface for various near-surface scattering models. The particle velocity of the wave field can be obtained by solving the integral equation with the computational method discussed in Chapter 3. In the calculation of the wave field, the Green's tensor for a layered half space plays a key role. Therefore, before we present the numerical results of the wave field for different scattering models, we first validate the layered half-space Green's tensor by comparing it to the Green's tensor for a homogeneous half space (Blonk and Herman, 1994).

We then consider a relatively simple model, with a horizontal plane-wave source at depth and a scatterer at the surface. This model allows us to qualitatively compare our results to experimental data collected at the surface of a similar laboratory scale model. These experimental data have been collected in collaboration with the PAL (Physical Acoustics Laboratory) at Colorado School of Mines, Golden, Colorado.

We also calculate the wave field for larger models in which the scattering domain consists of a random distribution of scatterers. In these models, we increase the size and the depth of the scattering domain.

Finally, we show results for the particle velocity of the wave field when the source is located at the surface. We compare these results to experimental data collected using the same geometry. Because we also roughly know the parameters of the scatterer, this allows us to make a quantitative comparison. This last section is the point-of-departure for the next chapter where the data will serve as input for an inverse scattering method for surface waves.

3.1 Validation of the Layered Half-Space Green's Tensor

In order to validate the layered half-space Green's displacement tensor derived in Appendix B, we excite a source at the surface, while the depth of observation is 2.5 m. We consider one layer overlying a half space with the same properties (the densities, P- and S-wave speeds of the layers are the same), so that the layered half space reduces to a homogeneous half space. The homogeneous half space Green's tensor in the slowness-frequency domain was derived by Blonk and Herman (1994). The properties of the model are given as follows: $\rho = 1800 \text{ kg/m}^3$, $c_S = 600 \text{ m/s}$, $c_P = 400 \text{ m/s}$, respectively.

We use a source waveform containing temporal frequencies between 0 Hz and 48 Hz. The central frequency is 25 Hz. The amplitude spectrum W of the source and its time-domain waveform are shown in Figure 3.1.

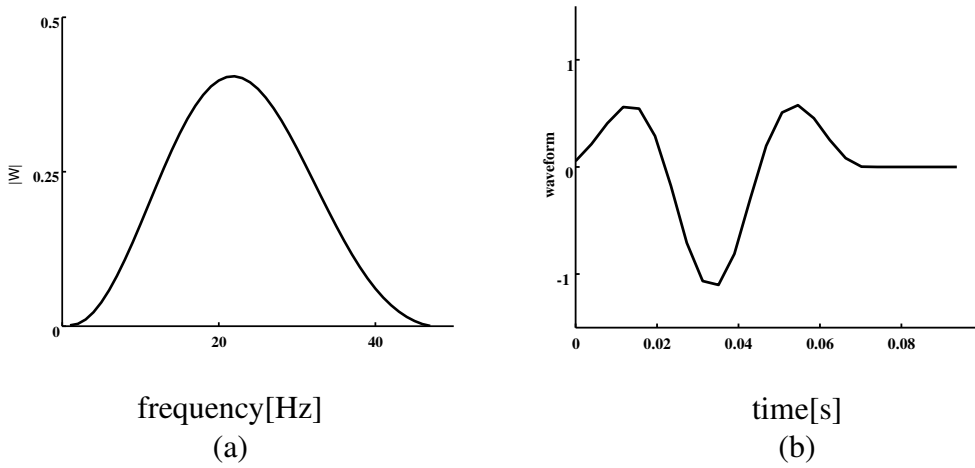


Figure 3.1: The waveform W in the frequency domain (a) and the time domain (b).

Using the Fourier transform (given in Appendix A), the space-time domain Green's tensor is calculated. We now compare the time-domain counterparts of Wu_{ij}^G and $Wu_{ij}^{G,hf}$ (the time-domain Green's tensor convolved with the source waveform) where Wu_{ij}^G is the space-time domain Green's tensor derived in Appendix B, while $Wu_{ij}^{G,hf}$ is the space-time domain Green's tensor derived by Blonk and Herman. The results are shown in Figures 3.2(a)-(d).

In these figures, the horizontal distance between the source and the receiver is 5 m. The results indicate that the solution for each element using the scattering matrix method (as discussed in Appendix B, equations (B.33)-(B.35)) agrees well with the method of Blonk and Herman.

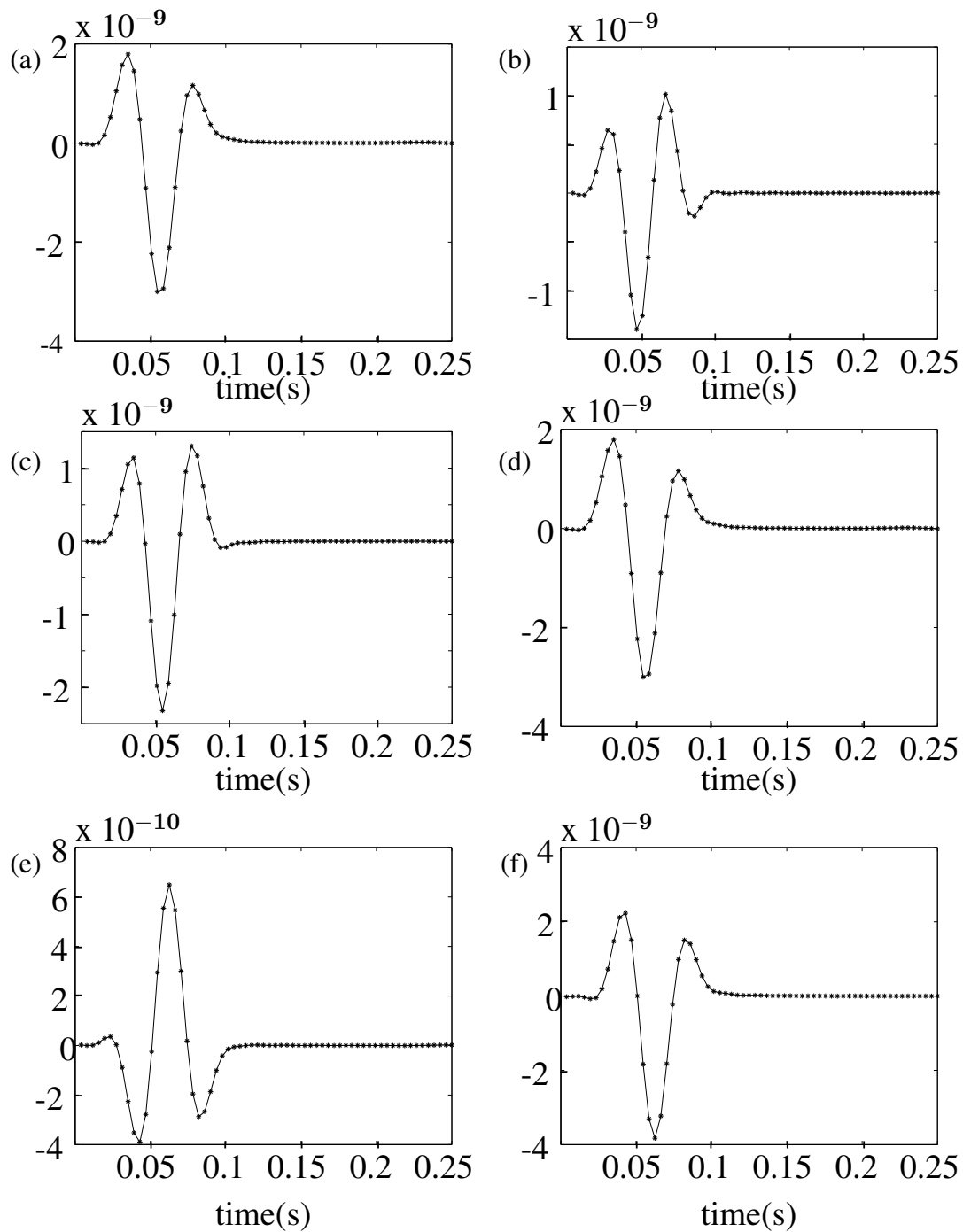


Figure 3.2: Comparison between the Green's tensor as a function of time (s). The solid line denotes the result for the elements of the Green's tensor, $W_{ij}^{G,hf}$, derived by Blonk and Herman (1994); the symbol * represents the result of our Green's tensor, W_{ij}^G , based on equation (B.33)-(B.35).

3.2 Results for a Simple Model

In order to illustrate the method discussed in the previous chapter, we first consider a relatively simple model and compute the vertical component of the particle velocity of the wave field at the surface. We want to investigate in which way scattering by heterogeneities close to the surface of the Earth affect upcoming reflections. This problem is relevant in exploration seismology where near-receiver scattering can be a cause of poor data quality, which is reflected in the quality of the final image of the subsurface. Analogously, near-receiver scattering can be a source of noise in teleseismic receiver-function analysis (Kennett, 2002). To make the situation realistic, we include a free surface, because we expect that surface waves will be excited when the incident field (an upcoming reflection event) hits a shallow scatterer.

The model is shown in Figure 3.3, where the scattering domain \mathcal{D} is located in the homogeneous half-space medium and at a depth of 5 m below the surface. The size of the scattering domain D is $30 \text{ m} \times 30 \text{ m} \times 30 \text{ m}$.

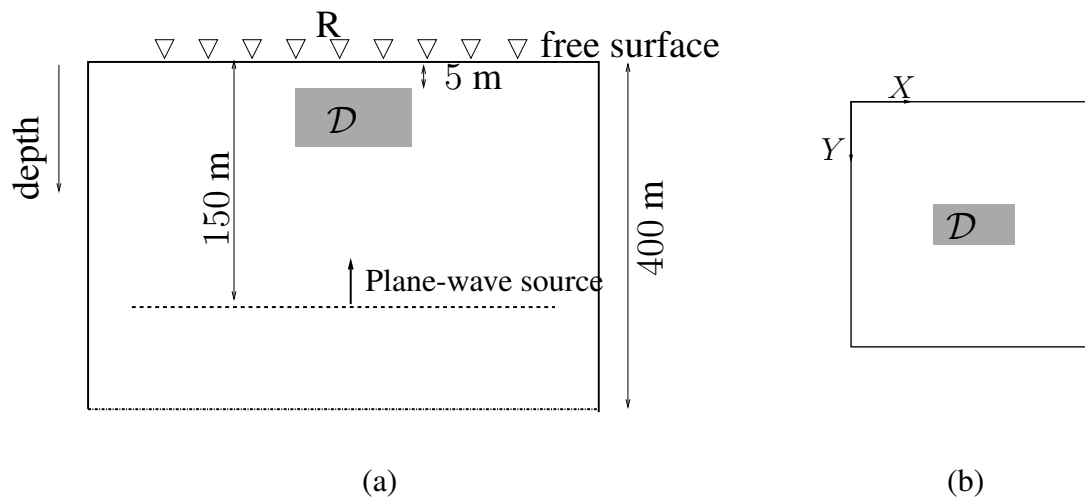


Figure 3.3: (a) Cross section of 3D near-surface model with a heterogeneity close to the surface. The plane-wave source is located at 150 m depth; the receivers R are at the surface; D is the scatterer domain at a depth of 5 m below the surface. The plane-wave source generates the upcoming plane compressional wave. (b) Topview of the model.

A horizontal plane-wave source is excited at 150 m depth to simulate an upcoming compressional wave, reflected from the deeper subsurface. Receivers are located at the surface. The parameters of the model are given as follows: $\rho^e = 1500 \text{ kg/m}^3$, $c_S = 1000 \text{ m/s}$, $c_P = 3000 \text{ m/s}$, respectively. The density of the scattering domain (ρ^D) equals 3500 kg/m^3 . The waveforms in the frequency- and the time-domain are given in Figure 3.1. The peak frequency of the source is

about 25 Hz. The wavelength for the dominant frequency, i.e the shear-wavelength, is $\lambda_s \approx 40$ m which is also roughly the size of the scatterer.

To investigate the convergence of our method, we first compute the solution of the vertical component of the particle velocity of the scattered wave field for different discretizations of the scatterer domain. The receiver position is located in the center of the scatterer domain. The scatterer domain is subdivided into equally-sized cells with sides, $\Delta x = \Delta y = \Delta z = 15$ m $\approx 0.4\lambda_s$ (8 grid points), $\Delta x = \Delta y = \Delta z = 10$ m $= 0.25\lambda_s$ (27 grid points), $\Delta x = \Delta y = \Delta z = 7.5$ m $\approx 0.2\lambda_s$ (64 grid points), respectively. The results using 8 grid points, 27 grid points and 64 grid points are shown in Figure 3.4 by the plus line, the dotted line and the solid line, respectively. The result for 27 and 64 points almost coincide. Hence, the result has converged and we choose the cell size $0.25\lambda_s$ in subsequent calculations.

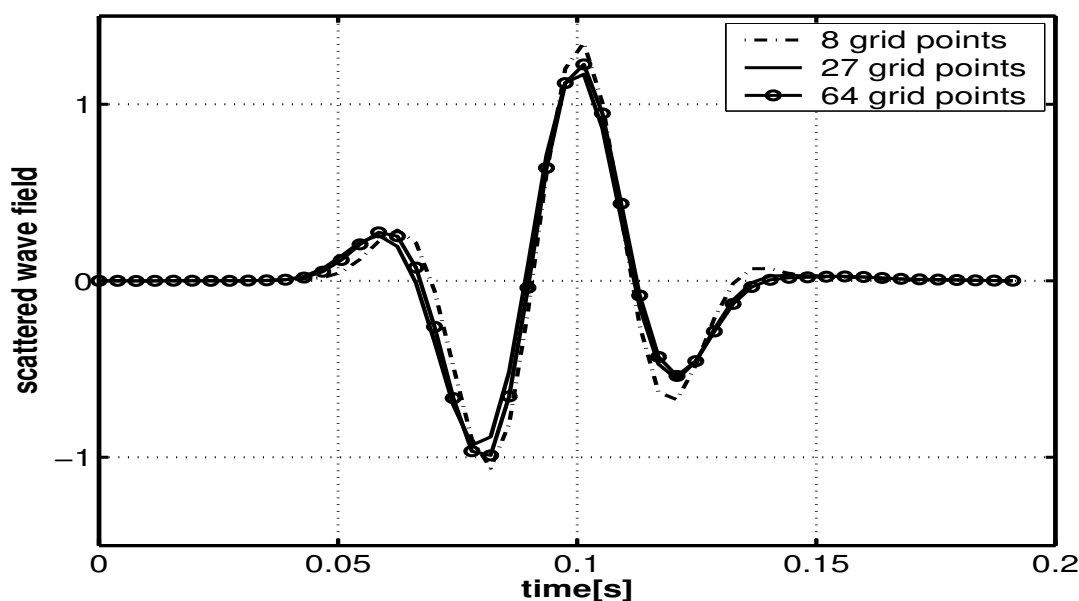


Figure 3.4: *The vertical component of the scattered wave field of the numerical solution of the integral equation using the method of moments for different discretizations of the scattering domain. The model is shown in Figure 3.3. The receiver position is taken at position $x = 64$ m, $y = 64$ m and $z = 0$ above the center of the scattering domain. The result using a cell size of $0.4\lambda_s$ (8 grid points) is given by the plus line. The dotted line denotes the result using a cell size of $0.25\lambda_s$ (27 grid points). The solid line denotes the result using a cell size of $0.2\lambda_s$ (64 grid points). The results for 27 and 64 points almost coincide. The result has thus converged and we choose the cell size $0.25\lambda_s$.*

In Figure 3.5, we display the vertical component of the particle velocity of the incident wave (in the background medium) as a function of time and receiver position.

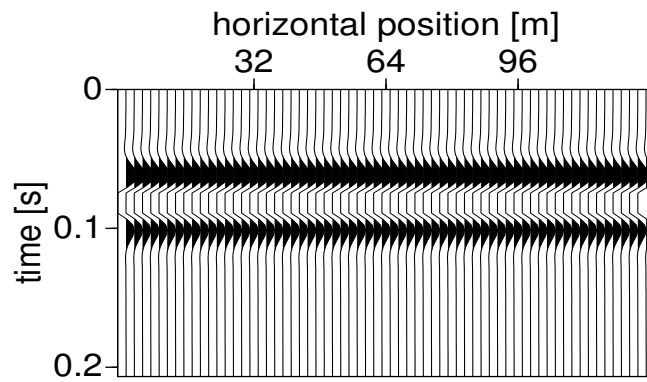


Figure 3.5: *The compressional plane-wave field in the absence of the heterogeneity (the incident wave field).*

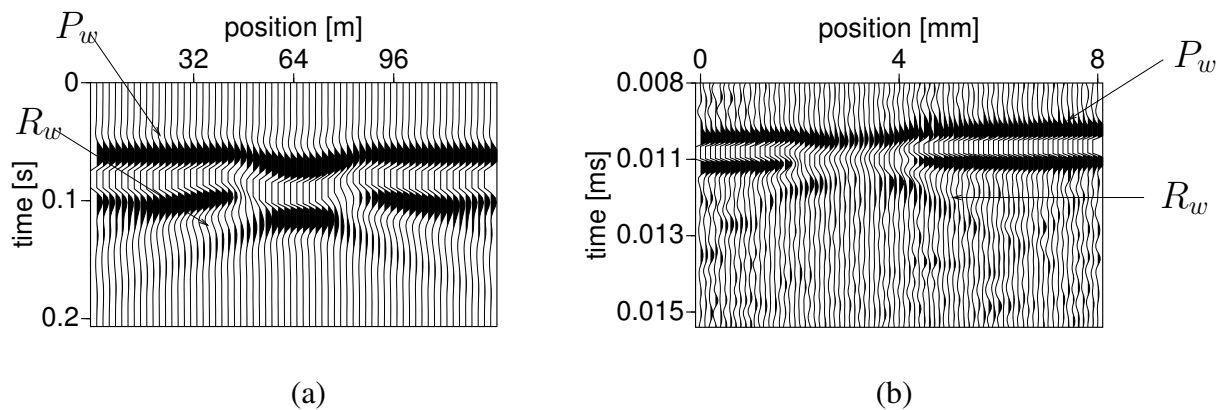


Figure 3.6: *The total wave field obtained by solving the integral equation (a) and from experimental data recorded in the Physical Acoustics Lab. (b). The P-wave is denoted by P_w , and the Rayleigh wave by R_w . We conclude that similar effects are found in both our theoretical result and the experimental data.*

In Figure 3.6(a), the vertical component of the total wave field is shown as a function of time and receiver position. In this figure, one can observe a delay in the arrival time of the P -wave above the anomaly of about 7 ms; this is commonly referred to as the static time shift (Yilmaz, 1988; Cox, 1999) and is due to the difference in travel time through the embedding and the scatterer. The time shift calculated using a statics model (Taner et al., 1974) is about 5 ms. From the figure it is clear that this statics model only predicts the observed shifts in the data in an approximate way (the shift varies above the anomaly). This may be attributed to the fact that the anomaly has a strong contrast with the background and it is not smooth compared to the wavelength, so that scattering and diffraction become important. Moreover, one can observe a scattered Rayleigh wave (labeled with R_w in the figure), excited by the incident P -wave and scattered by the anomaly. The scatterer acts as a secondary (scattering) source and since it is close to the surface, most of the scattered energy is converted into a surface (Rayleigh) wave (Wagner and Langston, 1992).

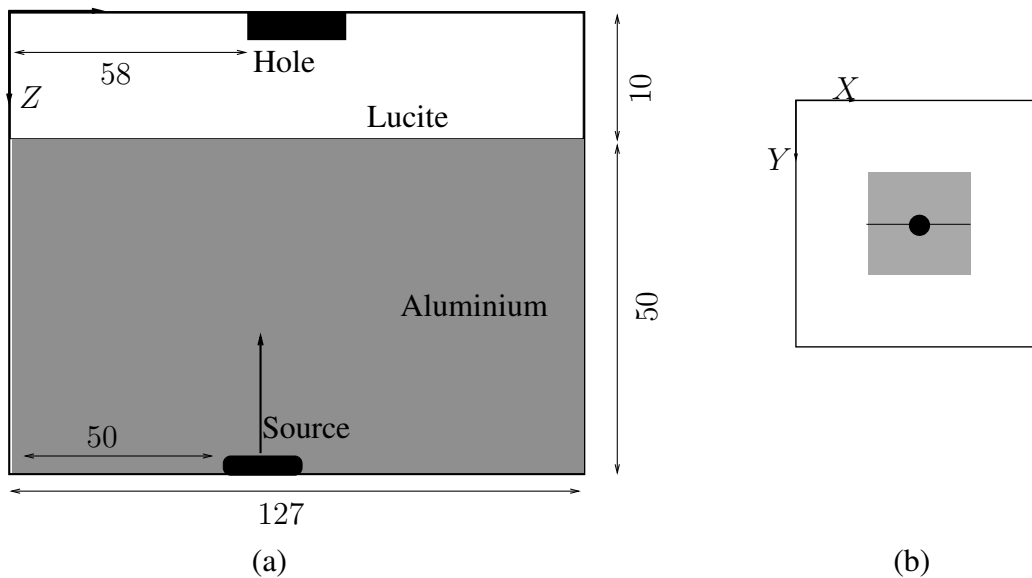


Figure 3.7: (a) Side- and (b) Top view of the two-layered model with cavity. All dimensions are given in mm.

These observations are confirmed by measurements of the wave field at the surface of a laboratory model (Campman et al., 2005). The geometry of the laboratory model given in Figure 3.7(a). As shown in Figure 3.7(a), the geometry of the laboratory model and our numerical model given in Figure 3.3(a) are comparable. The cross section of the laboratory model (Figure 3.7(b)) is also similar to the one shown in Figure 3.3(b). However the parameters are different.

The laboratory model consists of an aluminum block topped by a Lucite layer, in which a hole was drilled a 2-mm wide and 3-mm deep cavity. The dimensions of the cavity are about one wavelength. A body wave was generated by a point source at the bottom of a two-layered model and as it reached the surface it was scattered by the cavity. The wave field was recorded in a 4-cm² region, at 0.1-mm intervals. To model the scatterer we used a scatterer domain with a density of $\rho^D = 3500 \text{ kg/m}^3$, while the actual scatterer is a cavity filled with air. This choice of ρ only makes a qualitative comparison possible. For the embedding medium we have used roughly the parameters of Lucite (see Bodet et al. (2004) for example).

In Figure 3.6(b) we show the first upcoming body wave. Here, the P -wave has a time delay above the cavity and, like in the modeled data, one can observe a scattered Rayleigh wave traveling outward from the anomaly. From this figure, it is clear that similar effects are found in both our theoretical result and the experimental data.

3.3 Results for a Random Scattering Distribution

In the second test, we consider a similar geometry as described above (Figure 3.3), but now containing a random distribution of scatterers. The densities of the scattering domains are chosen from a uniform random distribution on the interval between 0 and 4000 kg/m³ (displayed in Figure 3.8). The size of the scattering domain (\mathcal{D}) is $60 \times 60 \times 60 \text{ m}^3$ (i.e. $\approx 1.5\lambda_s$). The size of the scattering domain is now two times larger than in the previous example.

The vertical component of the particle velocity of the total wave field is shown in Figure 3.9. In the calculation, the cell size of the discretization of the scatterer domain is about $0.25\lambda_s$, and the total amount of grid points equals 216. In this figure, we again observe time shifts and scattered Rayleigh waves. Now, the Rayleigh waves excited by different scatterers produce interference patterns, producing a complex coda.

In Figure 3.10 we show the top view of the vertical component of the total wave field at $t = 120 \text{ ms}$ and $t = 160 \text{ ms}$, respectively, which is about the time it takes for the incident wave to go through one cycle. From Figure 3.10 it is clear how the wave front is disturbed due to scattering. Comparing Figures 3.10(a)-(b) we observe that the maximum amplitudes do not remain in the same spatial positions (of the scatterers) as we would expect without interference. However, due to constructive and destructive superposition of the scattered waves, the peaks can occur at different spatial positions, at different times.

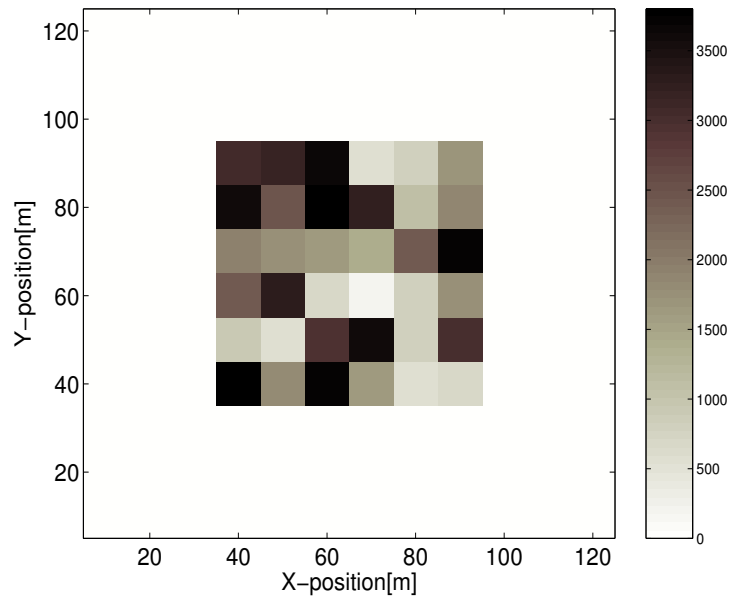


Figure 3.8: Top view of the model of \mathcal{D} (with size $1.5\lambda_s \times 1.5\lambda_s \times 1.5\lambda_s$).

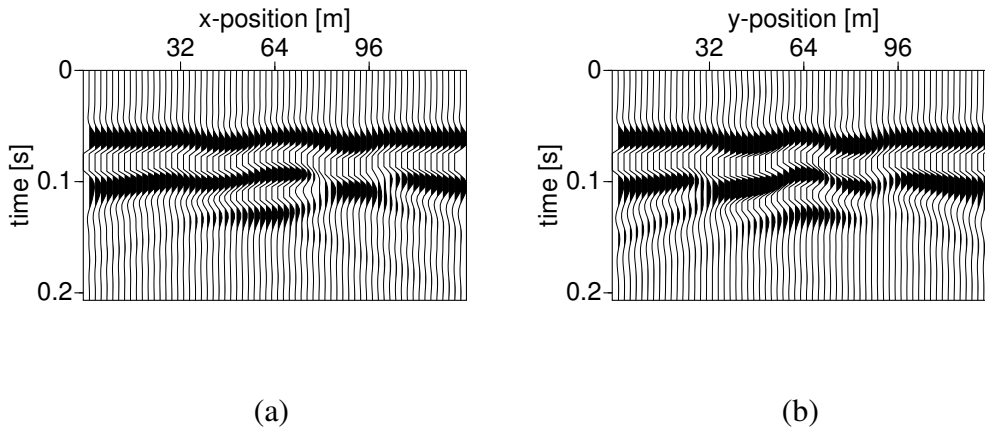


Figure 3.9: The vertical particle velocity along two perpendicular lines for the random model shown in Figure 3.8. We observe complex interference patterns due to the scattered Rayleigh waves.

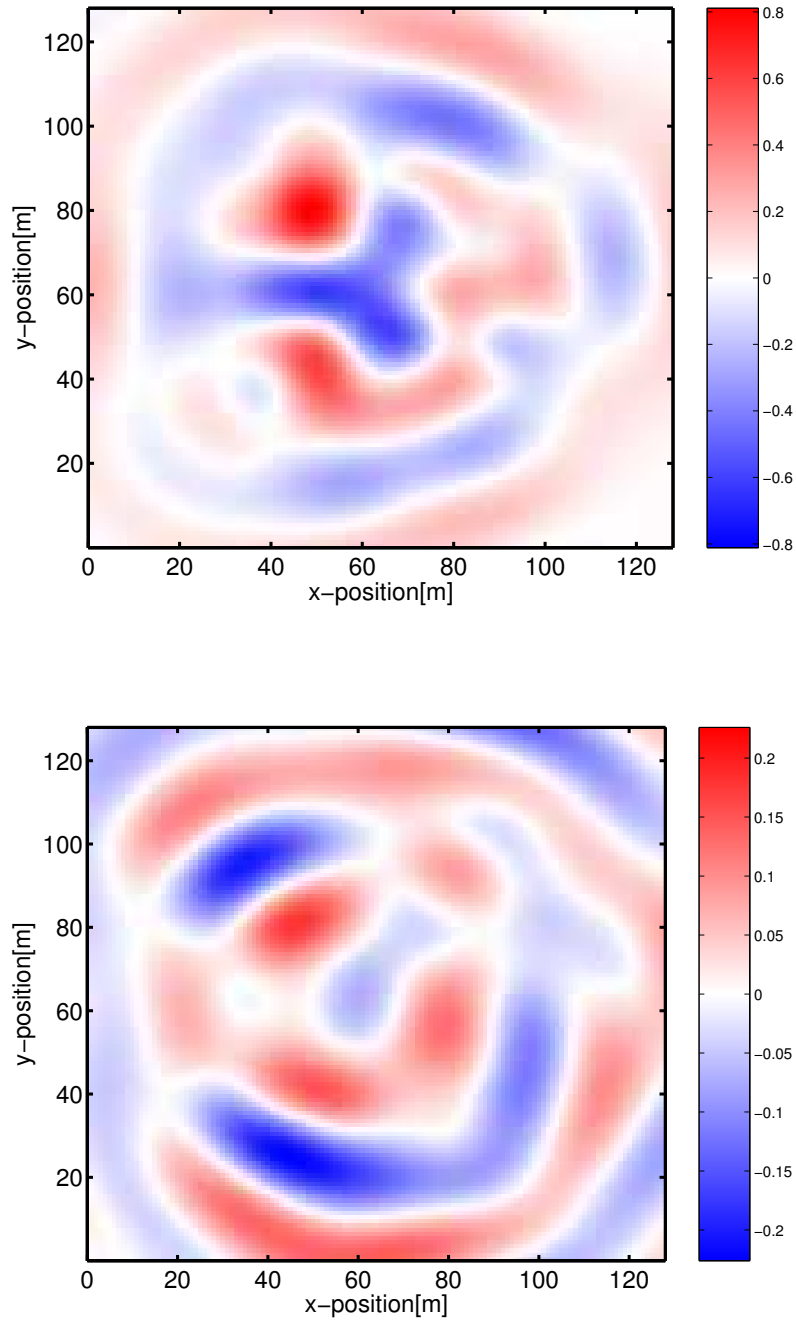


Figure 3.10: Top view of the vertical component of the total wave field for the random model of Figure 3.9 at $t = 120$ ms and 160 ms, respectively.

3.4 Results for a Thin Layer with a Random Scatterer Distribution

Finally, we consider the same geometry as in the previous case (Figure 3.3), but with a thin layer containing a random scatterer distribution. The size of the total scattering domain (\mathcal{D}) is about $4\lambda_s \times 4\lambda_s \times \frac{1}{4}\lambda_s$. The topview of the model is shown in Figure 3.11. The scattering domain is subdivided into equal-sized cells with side lengths, $\Delta_x = \Delta_y = \Delta_z = \frac{1}{4}\lambda_s$. Hence, we have 256 discretization points in the x - and y -directions and 1 point in the z direction, and the total amount of grid points equals 256.

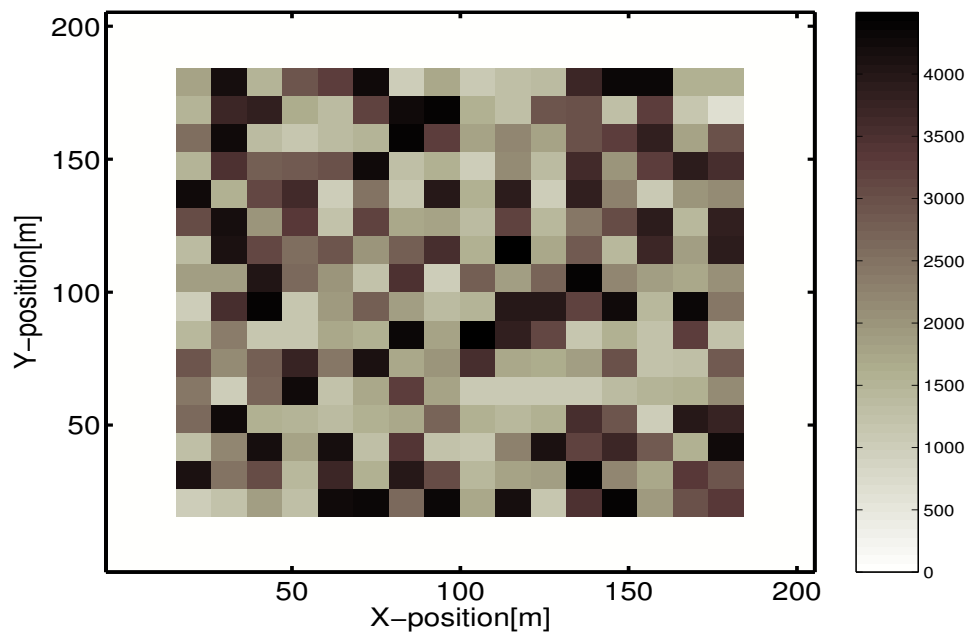
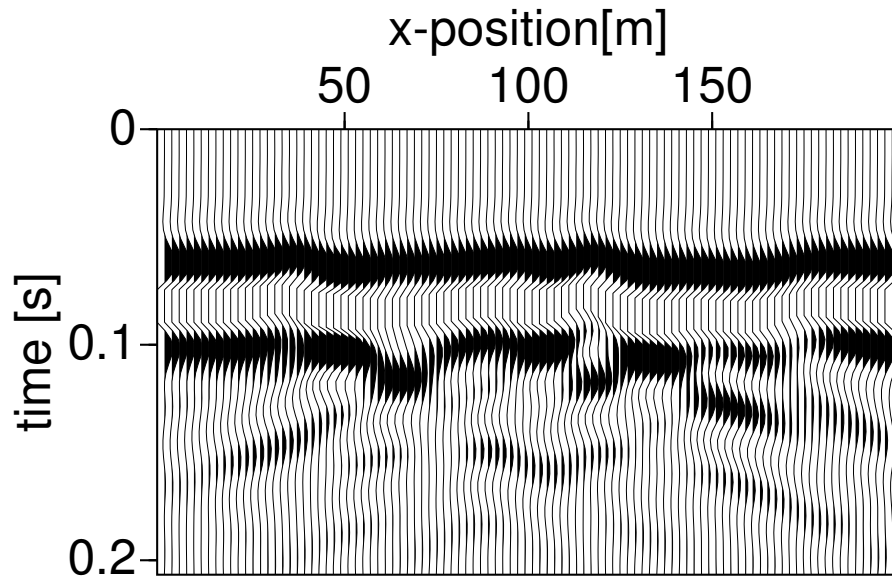


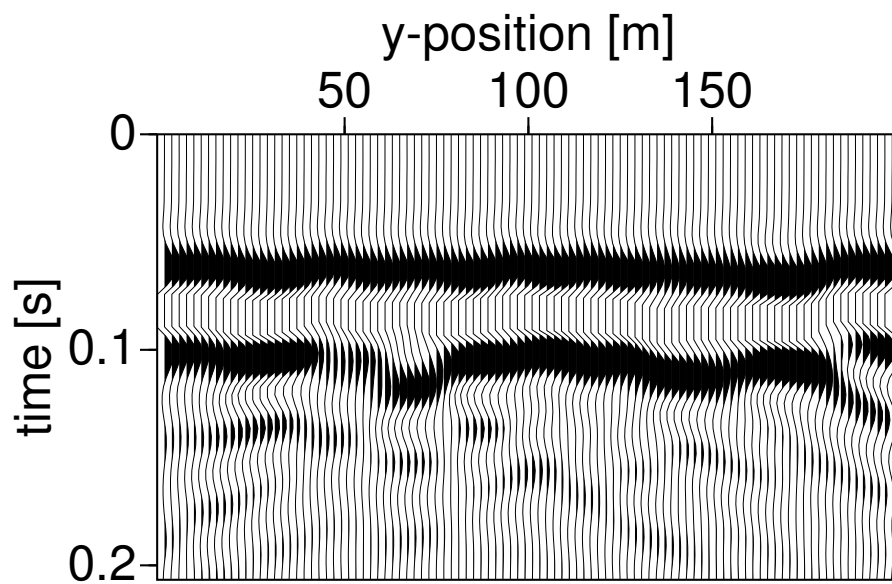
Figure 3.11: Top view of the model of \mathcal{D} (with size $4\lambda_s \times 4\lambda_s \times \frac{1}{4}\lambda_s$).

Figure 3.12 shows the vertical component of the particle velocity of the total wave field along two perpendicular lines. In this case, the scattered wave field becomes increasingly complex. At several places (in Figure 3.12(a) around 100 ms and between 140 and 180 m and in Figure 3.12(b) at 100 ms around 50 m), one can observe strong destructive interference, which degrades the continuity of the upcoming wave field.

In Figure 3.13(a)-(b) we show again the top view of the vertical component of the total wave field at $t = 160$ ms and at $t = 200$ ms, respectively. Here, interference produces a very complicated wave field. Again, the amplitude peaks shift location as a function of time. Such complex wave fields are typically observed in land seismic data containing large amounts of near surface scattering (Herman and Perkins, 2004, for example).



(a)



(b)

Figure 3.12: *The vertical component of the total wave field along two perpendicular lines through the center of Figure 3.11.*

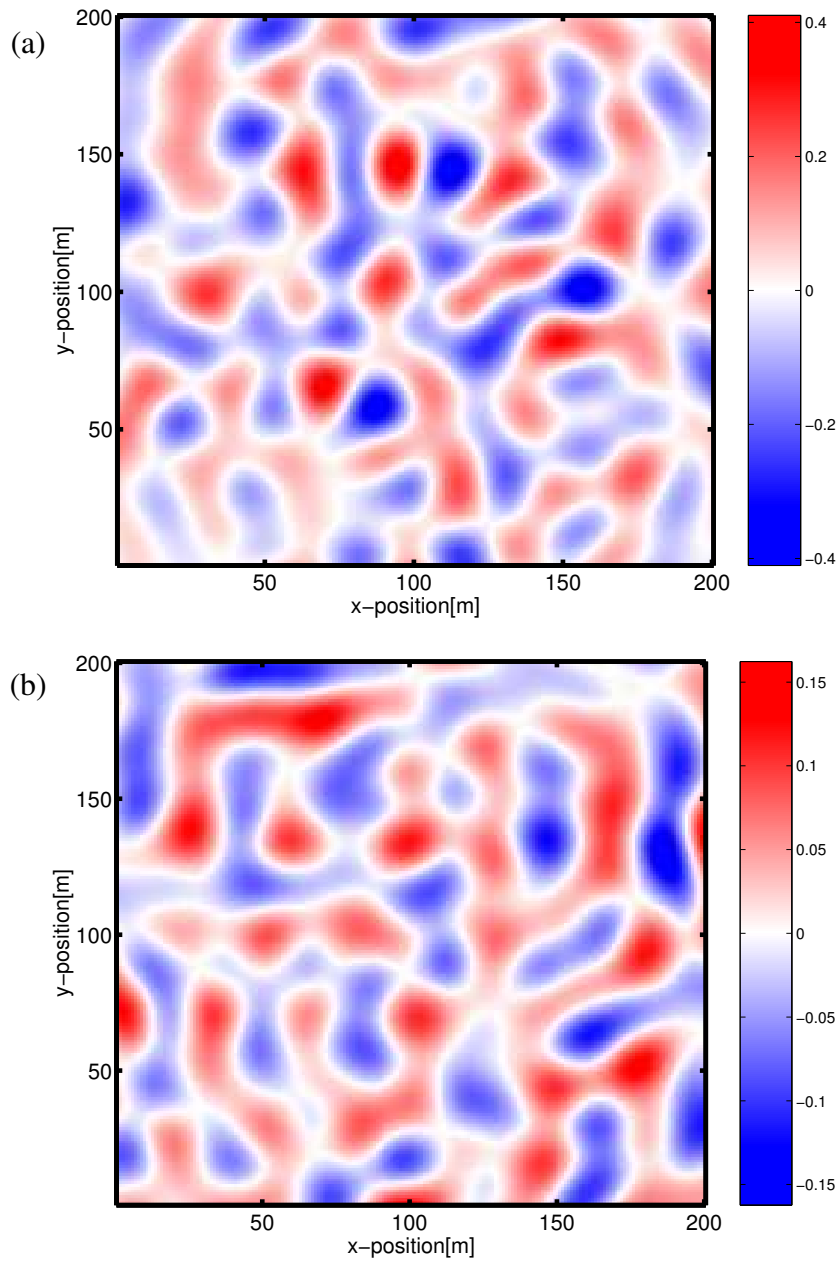


Figure 3.13: Top view of the vertical component of the total wave field for the thin layer of Figure 3.12 at $t = 160$ ms (a) and $t = 200$ ms (b), respectively.

3.5 Results for High-Velocity Contrasts in a Low-Velocity Background

While the previous problems are illustrative of karsting in carbonate surface layers in deserts, for example, another problem in seismic exploration is permafrost. In areas with permafrost, the background may be unevenly frozen giving rise to high velocity contrasts in a low-velocity background (Abma, 1994, 2002). In this case, we consider the density of the scattering domain lower compared to the background medium. In order to see if our method can also handle this type of problems, we again consider one scatterer close to the surface, but the scatterer now has a significantly higher velocity than the background. In this case, we consider a size of the scattering domain D of $30 \times 30 \times 80 \text{ m}^3$. A horizontal plane-wave source is excited at 250 m depth to simulate an upcoming reflection from the deeper subsurface. Receivers are located at the surface. The geometry of the model is the same as shown in Figure 3.3. The parameters of the model are given as follows: $\rho^e = 3500 \text{ kg/m}^3$, $c_S = 1600 \text{ m/s}$, and $c_P = 3200 \text{ m/s}$. The density of the scattering domain (ρ^D) is 700 kg/m^3 . The Rayleigh wavelength is about 64 m.

Using the same waveform as given in Figure 3.1, we calculate the vertical velocity for the wave field at the surface. The numerical result for the vertical velocity at the surface is shown in Figure 3.14. From this figure, we observe a forward time-shift, which we expect from an analysis with rays (Combee, 1994). This is known as a 'pull-up' in the exploration industry (Cox, 1999), and is typically associated with permafrost topography (Abma, 2002). One can also observe a scattered Rayleigh wave, excited by the incident P -wave and scattered by the anomaly.

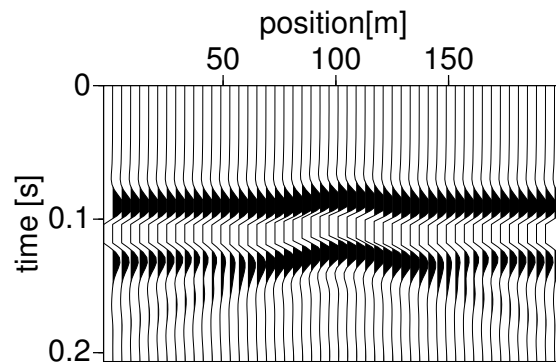


Figure 3.14: *The vertical component of the total wave field for a high-velocity anomaly.*

3.6 Results for a Source at the Surface

So far, we located the source at depth to simulate an upcoming reflection from the deeper subsurface. We now consider a point source located at the surface which mainly generates surface waves.

Surface waves play an important role in the seismic method (Snieder, 1986, 1987; Blonk et al., 1995). By placing the source at the surface, the bulk of the seismic energy is contained in the surface wave. Now, we mainly have surface-to-surface wave interaction.

3.6.1 Result for Three Scatterers

In this model, the source is excited at position $x = 0, y = 0$ m at the surface of the model, with a dominant frequency of about 25 Hz. The vertical velocity of the total wave field is calculated at 1 m intervals at the surface of a 120×120 m² area. The embedding medium here consists of a homogeneous half space. The S -wave velocity of the embedding medium is 1000 m/s, its P -wave velocity and density (ρ^e) are 3000 m/s and 1500 kg/m³, respectively. The Rayleigh wavelength is about 40 m.

We consider three scatterers located 5 m below the surface, namely \mathcal{D}_1 , \mathcal{D}_2 and \mathcal{D}_3 (Figure 3.15). The area of the scatterers is 10×10 m², while the vertical extent is 20 m and the densities of the scatterers are given by 3500, 3750 and 4000 kg/m³, respectively. A top view of this model is shown in Figure 3.15. The waveforms in the frequency- and the time-domain are given in Figure 3.1.

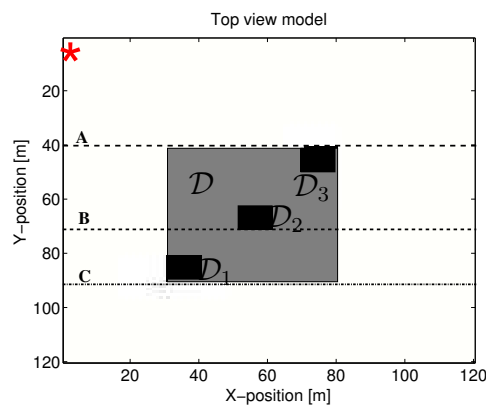


Figure 3.15: Top view of the model used to calculate the vertical velocity of the wave field. The density of the scattering domain \mathcal{D} is 1500 kg/m³ (equal to the embedding), while the densities of the scattering domain \mathcal{D}_1 , \mathcal{D}_2 and \mathcal{D}_3 are 3500 kg/m³, 3750 kg/m³ and 4000 kg/m³, respectively.

In order to calculate the vertical velocity of the wave field, we consider the scattering domain \mathcal{D} containing the three scatterers \mathcal{D}_1 , \mathcal{D}_2 , \mathcal{D}_3 (displayed in Figure 3.15).

The vertical velocity of the wave field is plotted in Figure 3.16(a)-(c). In these figures, we show three seismograms of the vertical velocity of the wave field along the lines of **A**, **B**, and **C** illustrated in Figure 3.15. Figure 3.16(a) corresponds to the line **A**, while Figures 3.16(b) and (c) correspond to the lines **B** and **C**, respectively. From these figures, a disturbance in the incident wave field is visible and we observe a small time-delay in the wavefront above the scatterers. Also, we observe that scattered Rayleigh waves are visible.

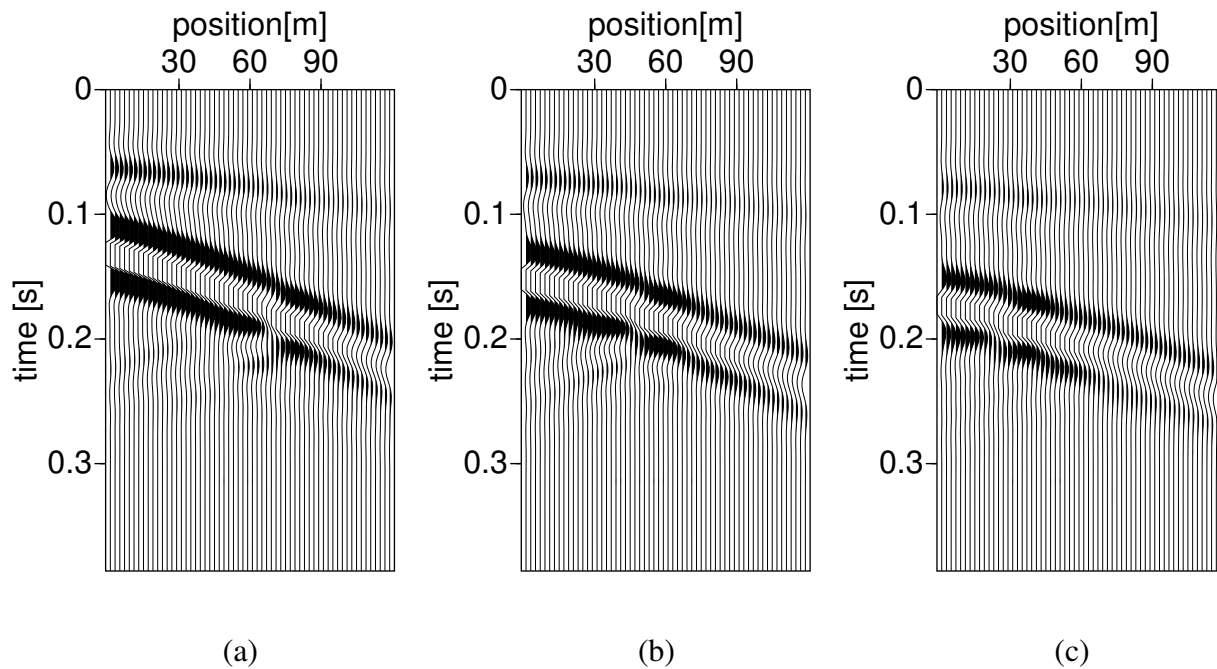


Figure 3.16: *The vertical velocity of the wave field along lines **A**, **B** and **C** of Figure 3.15.*

Figure 3.17 shows the top view of the incident wave field and the total wave field at $t = 0.117$, $t = 0.156$, 0.195 , 0.234 s, respectively. The left-hand side of this figure is the top view of the incident wave field, while the right-hand side is the topview of the total wave field.

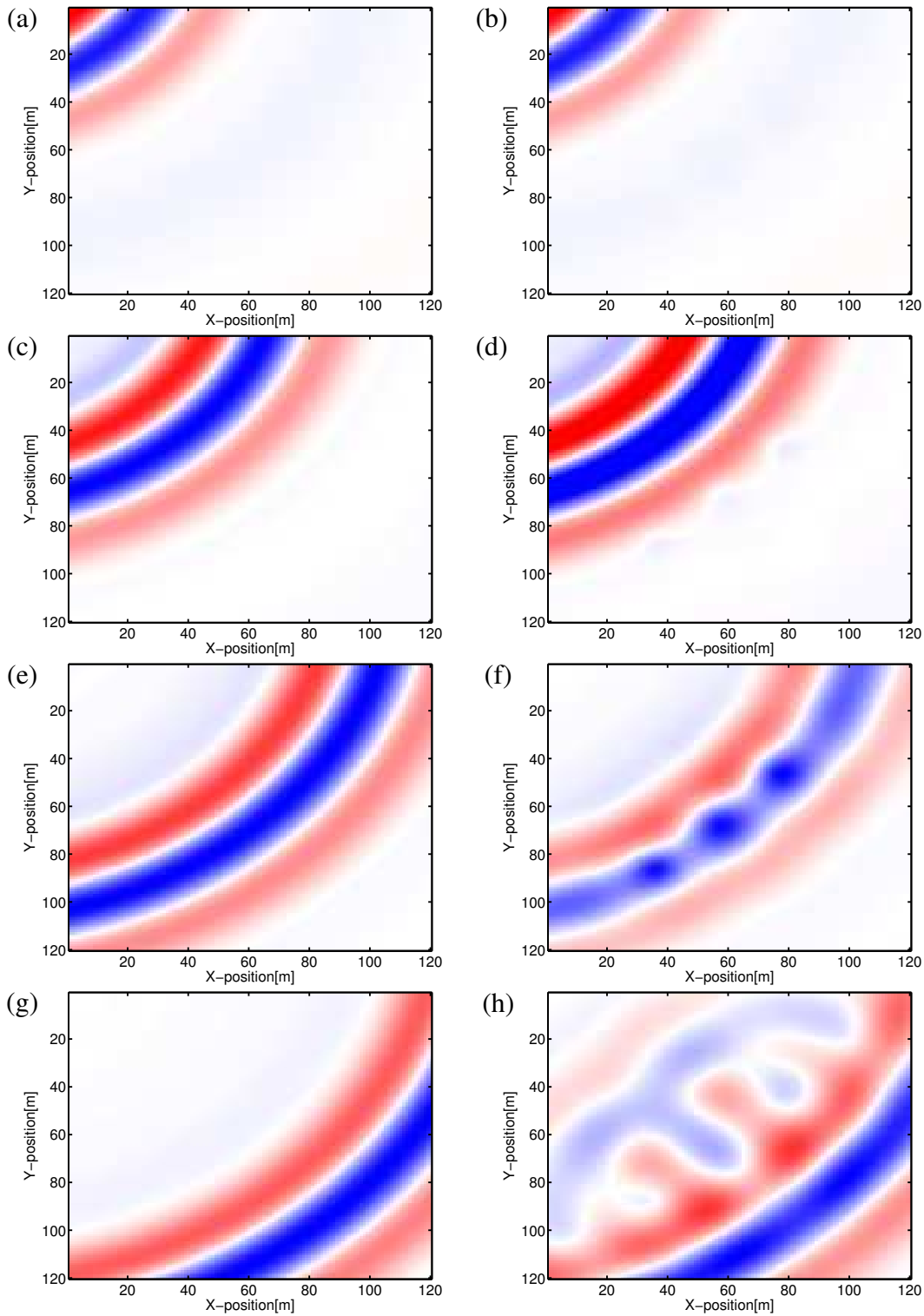


Figure 3.17: Top view of the incident wave field ((a), (c), (e) and (g)) and the total wave field ((b), (d), (f), and (h)) at $t = 0.117$ s, $t = 0.156$ s, $t = 0.195$ s and $t = 0.234$ s, respectively.

3.6.2 Comparison with Laboratory Experiments

Now, we compare the particle velocity of the wave field computed from our method to experimental data collected for the same geometry. Because we roughly know the parameters of the scatterer, this allows us to make a quantitative comparison.

In the experiment, we have a dominant frequency of 0.6 MHz. The geometry of the model is similar to the one shown in Figure 3.7(a), but now the anomaly \mathcal{D} is located in a homogeneous half-space medium and we consider a source at the surface. Scattered surface waves are excited by a circular scattering object with a diameter of 3 mm and a depth of 4 mm, which is comparable to the Rayleigh wavelength. Receivers are located at the surface at 0.6 mm intervals. In total we have 51 by 51 receiver positions. The top view of the model is illustrated in Figure 3.18. The parameters of the background medium are: $c_s = 3000$ m/s, $c_p = 5700$ m/s and $\rho^e = 2700$ kg/m³. The dominant Rayleigh wavelength (λ_R) is then 5 mm. The density of the scatterer object, $\rho = 7000$ kg/m³. The shot position is located at position $x = 0$, $y = 30$ mm at the surface of the model.

In Figure 3.20(a), we plot experimental data recorded from the dataline indicated in Figure 3.18.

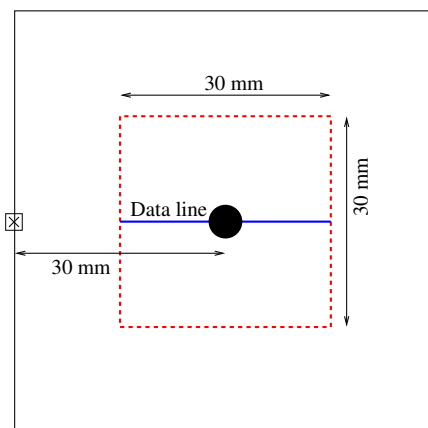


Figure 3.18: Topview of the geometry of the aluminium block. The source S is denoted by the star. The receivers R are located at the surface (denoted by the dashed line). The scatterer domain \mathcal{D} is indicated in black.

In order to compute the wave field using our method, we have to know the source waveform. To estimate it, we first consider one trace from the experimental data. The spectrum of this trace is given by W_{II} in Figure 3.19. From this figure, we can create a similar source waveform assuming it can be approximated by a Ricker wavelet using the same bandwidth. It is illustrated by W_I in Figure 3.19.

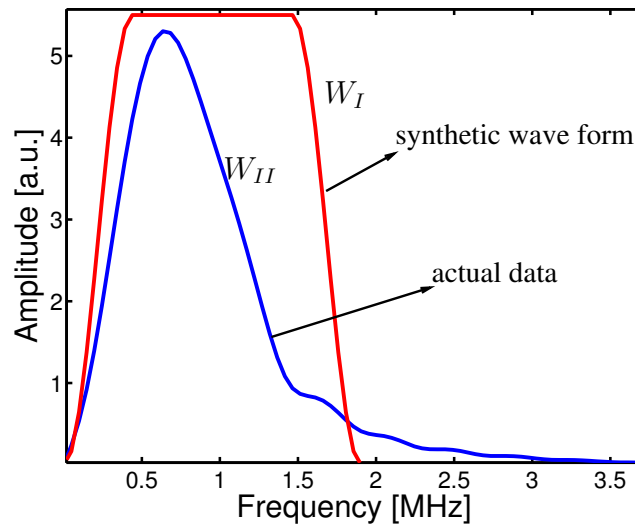


Figure 3.19: The source waveform (denoted by W_I) used to calculate the model data, while W_{II} is the waveform taken from the experimental data.

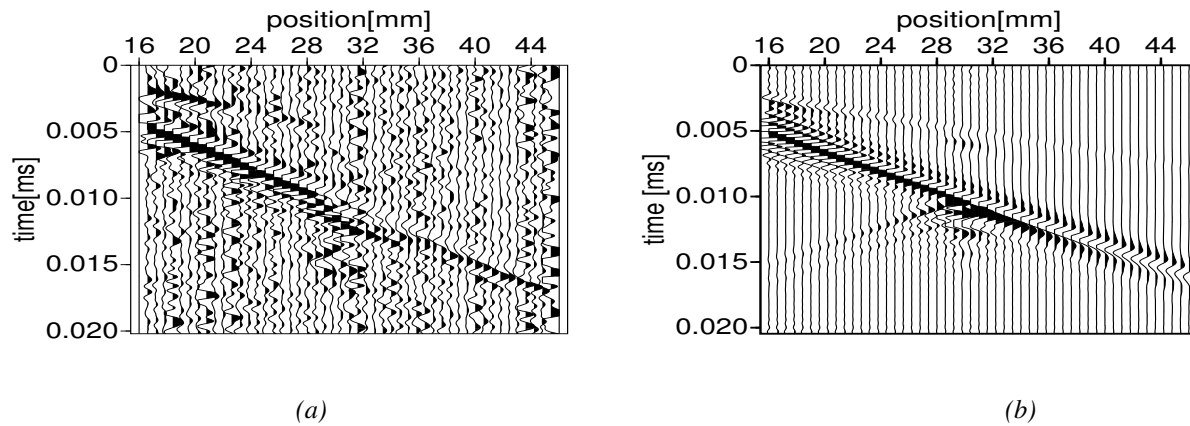


Figure 3.20: (a) The total wave field obtained from the experimental data recorded along the data line shown in Figure 3.18. (b) Our solution of the integral equation. We conclude that similar effects are found in both our theoretical result and the experimental data.

Using the same properties as used in the experimental data, we compute the vertical velocity of the total wave field. In Figure 3.20(b), we show the numerical result along the dataline

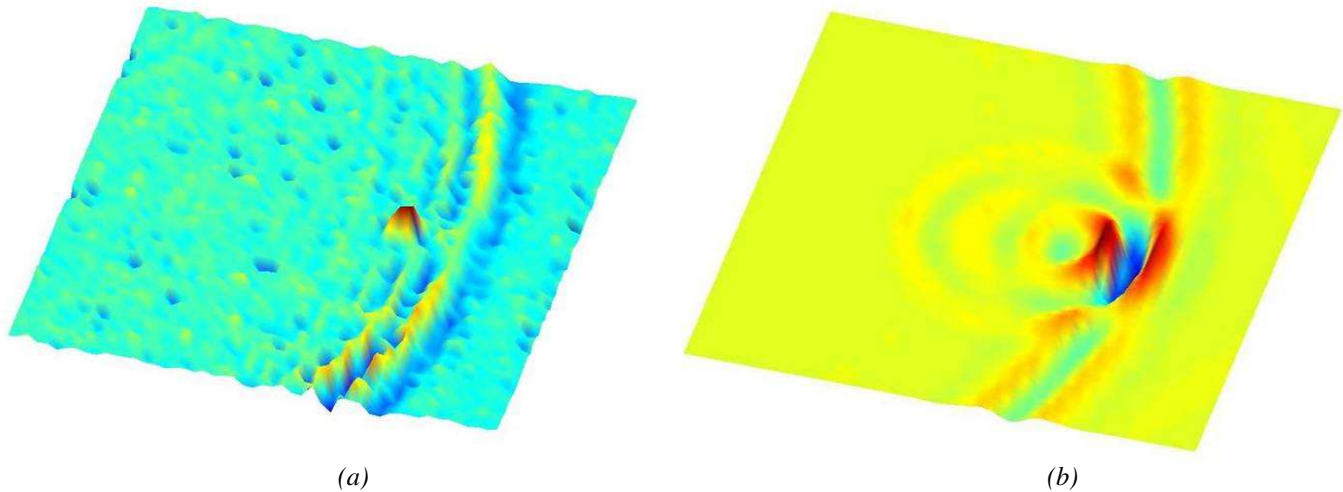


Figure 3.21: Snapshots (time-slices) of the wave field obtained from the experimental data (a) and our theoretical result (b) at $t = 0.014$ ms.

indicated in Figure 3.18. Figure 3.21(a)-(b) show the snapshots of the total wave field obtained from the experimental data and our theoretical result at $t = 0.014$ ms, respectively.

From Figure 3.20(a)-(b), we conclude that the comparison of the numerical result obtained using our computational method with experimental data shows good qualitative and quantitative agreement.

The laboratory data were acquired with a Laser-Doppler vibrometer (van Wijk et al., 2002). At each data point we record a number of traces that are then stacked to form one output trace. This operation reduces the amount of noise due to the limited reflectivity of the sample in the measured traces. In the data shown here, we have stacked the traces only a few times to reduce the time needed to acquire the data. However, this results in more noisy traces, as is clear from Figure 3.20(a).

The Inverse Problem for Scattered Surface Waves

4.1 Introduction

Based on the integral representation discussed in Chapter 2 we formulate the inverse problem for scattered surface waves. It is our objective to estimate the properties of near-surface heterogeneity, given the scattered field at the surface. The inversion is based on minimizing an error function consisting of the squared difference between the actual scattered field and the scattered field calculated with the integral representation developed in Chapter 2.

We assume that the wave field in the absence of the heterogeneity (the incident wave field in the background medium) is known. Both the total wave field in the scattering domain and the contrast function are unknown. The inverse problem is non-linear because the wave field in the scattering domain depends on the properties of the heterogeneity.

4.2 Formulation of the Inverse Problem

In order to formulate the inverse problem, we repeat equation (2.47) of the particle displacement of the total wave field generated by a vertical source at position \mathbf{x}^s and recorded at points $\mathbf{x} \in \mathcal{S}$:

$$u_i(\mathbf{x}, \mathbf{x}^s) = u_i^{inc}(\mathbf{x}, \mathbf{x}^s) + u_i^{sc}(\mathbf{x}, \mathbf{x}^s), \quad (4.1)$$

where u_i^{inc} is the particle displacement of the incident wave field generated by the force in the embedding, layered, half space (without heterogeneity) and u_i^{sc} is the particle displacement of the scattered wave field that accounts for the presence of the heterogeneity. In the above equation, we have omitted the dependence on ω of the wave field.

The particle displacement of the scattered wave field, u_i^{sc} , at location \mathbf{x} , is expressed as an integral representation over the scattering domain \mathcal{D} . It reads (see also equation 2.48)

$$u_i^{sc}(\mathbf{x}, \mathbf{x}^s) = \omega^2 \int_{\mathbf{x}' \in \mathcal{D}} \sigma(\mathbf{x}') u_{ik}^G(\mathbf{x}, \mathbf{x}') u_k(\mathbf{x}', \mathbf{x}^s) dV, \quad (4.2)$$

where $\sigma(\mathbf{x}')$ is the contrast function, u_k is the wave field inside the scattering domain \mathcal{D} and $u_{ik}^G(\mathbf{x}, \mathbf{x}')$ is the Green's tensor for the layered embedding in the spatial domain. The expression for the Green's tensor can be found in Appendix B.

In seismic exploration, geophones measure the particle velocity of the wave field. For practical reasons, we therefore consider the expression of our integral representation in terms of particle velocity by differentiating the particle displacement of the wave field with respect to time. In the frequency domain, the i -th particle velocity of the wave field is then given by:

$$v_i(\mathbf{x}, \mathbf{x}^s) = -j\omega u_i(\mathbf{x}, \mathbf{x}^s). \quad (4.3)$$

In this thesis, we only consider the vertical component of the velocity of the scattered wave field, $v_3^{sc} = v^{sc}$. We can then rewrite the integral representation of the vertical velocity of the scattered wave field, v^{sc} , at position \mathbf{x} in the following operator form:

$$v^{sc} = \mathbf{G}_S \sigma, \quad (4.4)$$

where the operator \mathbf{G}_S is defined by

$$\{\mathbf{G}_S \sigma\}(\mathbf{x}) = \omega^2 \int_{\mathbf{x}' \in \mathcal{D}} u_k^G(\mathbf{x}, \mathbf{x}') v_k(\mathbf{x}', \mathbf{x}^s) \sigma(\mathbf{x}') dV, \quad \mathbf{x} \in \mathcal{S}. \quad (4.5)$$

In order to simplify the notation, we used $u_k^G(\mathbf{x}, \mathbf{x}') = u_{3k}^G(\mathbf{x}, \mathbf{x}')$, representing the third component of the wave field generated by a source in the k -direction.

For numerical evaluation of this integral, we approximate it with the aid of the midpoint rule, yielding:

$$\{\mathbf{G}_S \sigma\}(\mathbf{x}) = \omega^2 dx dy dz \sum_{m=1}^M \sum_{k=1}^3 u_k^G(\mathbf{x}, \mathbf{x}^{(m)}) v_k(\mathbf{x}^{(m)}, \mathbf{x}^s) \sigma(\mathbf{x}^{(m)}), \quad (4.6)$$

where $\mathbf{x}^{(m)}$ is the center point in the subdomains $\mathcal{D}^{(m)}$, for $m = 1, 2, 3, \dots, M$.

Note that the domain \mathcal{S} is the domain containing the receivers at the surface, whereas the domain \mathcal{D} is the domain containing the scattering objects.

In the forward problem discussed in Chapter 2, the contrast function is assumed to be a known function. In the inverse problem, however, the scattered wave field is known at the location of the receivers, while both the contrast function σ and the wave field in the scattering domain are unknown (as illustrated in Figure 4.1).

The inverse problem is non-linear because the wave field in the scattering domain depends on the contrast function. Several techniques exist to solve the inverse problem. One of these methods is the conjugate-gradient method (Polak, 1971; Tarantola, 1984; Kleinman and van den Berg, 1991; Van den Berg, 2002). In this thesis we apply the conjugate-gradient method (Polak-Ribière algorithm) for estimating the properties of the heterogeneity (contrast function) by iteratively minimizing a cost functional.

First, we introduce definitions of the inner product, norm and the adjoint operator on the

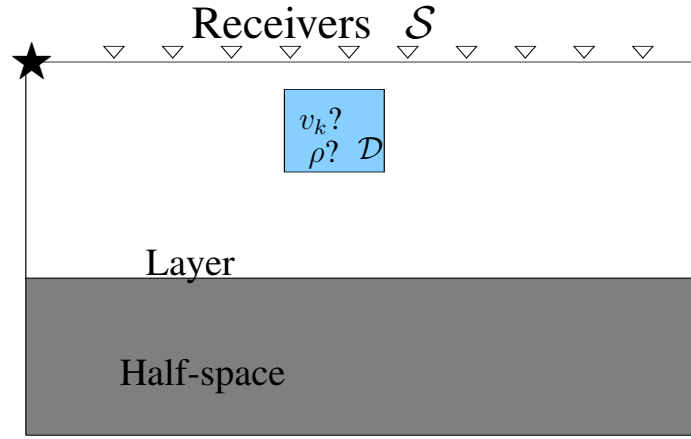


Figure 4.1: The geometry of the inverse problem for a 3D near-surface model with a heterogeneity \mathcal{D} embedded in a layered half space. The particle velocity v_k , for $k = 1, 2, 3$, and ρ are unknown functions in the scatterer. The scattered wave field is measured at the receivers \mathcal{S} . The symbol \star denotes the source.

domains \mathcal{S} and \mathcal{D} . The inner product on the domain \mathcal{D} is defined through the relation:

$$\langle \tau, v \rangle_{\mathcal{D}} = \int_{\mathbf{x} \in \mathcal{D}} \int_{\omega \in \mathcal{W}} \tau(\mathbf{x}, \omega) \bar{v}(\mathbf{x}, \omega) d\omega d\mathbf{x}, \quad (4.7)$$

where the overbar denotes complex conjugate, and τ and v are integrable functions on the domains \mathcal{D} and \mathcal{W} . Here, the domain \mathcal{W} is the frequency domain.

Similarly, the inner product on the domain \mathcal{S} is defined through the relation:

$$\langle \tau_1, v_1 \rangle_{\mathcal{S}} = \int_{\mathbf{x} \in \mathcal{S}} \int_{\omega \in \mathcal{W}} \tau_1(\mathbf{x}, \omega) \bar{v}_1(\mathbf{x}, \omega) d\omega d\mathbf{x}, \quad (4.8)$$

where τ_1 and v_1 are integrable functions on the domains \mathcal{S} and \mathcal{W} .

These inner products can be discretized as

$$\langle \tau, v \rangle_{\mathcal{D}} = 2\pi df dx dy dz \sum_{m=1}^M \sum_f \tau(\mathbf{x}^m, \omega) \bar{v}(\mathbf{x}^m, \omega), \quad (4.9)$$

$$\langle \tau_1, v_1 \rangle_{\mathcal{S}} = 2\pi df dx_s dy_s \sum_r \sum_f \tau_1(\mathbf{x}_H^r, \omega) \bar{v}_1(\mathbf{x}_H^r, \omega), \quad (4.10)$$

where $\omega = 2\pi f df$, with f is the frequency index, df is the frequency interval, $\mathbf{x}_H^r = (x_1^r, x_2^r) \in \mathcal{S}$ and dx_s and dy_s are the discretization x - and y -intervals of the domain \mathcal{S} . The positions at the

surface are denoted by r .

The norms on \mathcal{D} and \mathcal{S} follow as

$$\|\tau\|_{\mathcal{D}}^2 = \langle \tau, \tau \rangle_{\mathcal{D}}, \quad (4.11)$$

and

$$\|\tau_1\|_{\mathcal{S}}^2 = \langle \tau_1, \tau_1 \rangle_{\mathcal{S}}. \quad (4.12)$$

In our inversion algorithm we will also need the adjoint counterpart of equation (4.5). The adjoint operator, $\mathbf{G}_{\mathcal{D}}^\dagger$, is defined through the relation

$$\langle \mathcal{E}, \mathbf{G}_{\mathcal{S}}\sigma \rangle_{\mathcal{S}} = \langle \mathbf{G}_{\mathcal{D}}^\dagger \mathcal{E}, \sigma \rangle_{\mathcal{D}}, \quad (4.13)$$

where the functions \mathcal{E} and σ are not in the same vector space. The function \mathcal{E} is defined on the domain \mathcal{S} and σ is defined on the domain \mathcal{D} .

Substituting the expression of the operator $\mathbf{G}_{\mathcal{S}}\sigma$ in equation (4.5) into the left-hand side of equation (4.13), and interchanging the order of integration, the adjoint operator $\mathbf{G}_{\mathcal{D}}^\dagger$ is obtained in the following form (for a derivation, see Appendix F):

$$\{\mathbf{G}_{\mathcal{D}}^\dagger \mathcal{E}\}(\mathbf{x}') = \omega^2 \bar{v}_k(\mathbf{x}', \mathbf{x}^s) \int_{\mathbf{x} \in \mathcal{S}} \bar{u}_k^G(\mathbf{x}, \mathbf{x}') \mathcal{E}(\mathbf{x}) d\mathbf{x}, \quad \mathbf{x}' \in \mathcal{D}. \quad (4.14)$$

Since the domain \mathcal{S} is at the surface, the above equation can be written as follows:

$$\{\mathbf{G}_{\mathcal{D}}^\dagger \mathcal{E}\}(\mathbf{x}') = \omega^2 \bar{v}_k(\mathbf{x}', \mathbf{x}^s) \int_{\mathbf{x}_H \in \mathcal{S}} \bar{u}_k^G(\mathbf{x}_H, \mathbf{x}') \mathcal{E}(\mathbf{x}_H) d\mathbf{x}_H, \quad \mathbf{x}' \in \mathcal{D}, \quad (4.15)$$

where $\mathbf{x}_H = (x_1, x_2)$.

4.3 Conjugate Gradient Method

The objective of the inversion is to determine the contrast function $\sigma(\mathbf{x}')$, for $\mathbf{x}' \in \mathcal{D}$. Due to non-linearity, we also need to calculate the particle velocity of the wave field v_k for $k = 1, 2, 3$ in the scattering subdomains \mathcal{D} .

Let v^d denote the actual scattered field in the space-frequency domain and let v^{sc} denote the scattered field evaluated from the equation (4.4).

In each iteration j , we define the difference between the actual scattered field, v^d , and the scattered field evaluated from equation (4.4), v^{sc} , as follows:

$$\begin{aligned} \mathcal{E}^{(j)} &= v^d - v^{sc,(j)}, \\ &= v^d - \mathbf{G}_{\mathcal{S}}\sigma^{(j)}. \end{aligned} \quad (4.16)$$

The norm then follows as:

$$\|\mathcal{E}^{(j)}\|_{\mathcal{S}}^2 = \sum_f \sum_r |v^d - \mathbf{G}_{\mathcal{S}}\sigma^{(j)}|^2, \quad (4.17)$$

where f denotes the frequency index, r denotes the positions of the receivers.

We introduce the normalized cost functional as

$$\mathcal{F}^{(j)} = \frac{\|v^d - \mathbf{G}_S \sigma^{(j)}\|_S^2}{\|v^d\|_S^2} + \beta \|\sigma^{(j)}\|_D^2. \quad (4.18)$$

The first term in the equation is the normalized error, and the second term for stabilization of the inversion. The regularization parameter β optimizes the trade-off between the best fit and the stability of the inversion (Hansen, 1997).

We seek a minimum of the functional (4.18). To do so, we apply the conjugate gradient method that consists of an algorithm to construct sequences for the contrast function σ which iteratively reduce the value of the cost functional defined in equation (4.18).

We construct a sequence $\{\sigma^{(j)}\}$, for $j = 0, 1, 2, 3, \dots$ by updating the contrast functions $\sigma^{(j)}$ as follows:

$$\sigma^{(0)} = 0, \quad (4.19)$$

$$\sigma^{(j)} = \sigma^{(j-1)} + \alpha^{(j)} w^{(j)} \quad (j \geq 1), \quad (4.20)$$

where $\alpha^{(j)}$ is the *step size* and $w^{(j)}$ is the *update direction*. This parameter $\alpha^{(j)}$ and update direction $w^{(j)}$ are chosen such that the residual error $\mathcal{E}^{(j)}$, is minimized.

We select the *Polak-Ribière update direction* $w^{(j)}$ (Polak, 1971; Kleinman and van den Berg, 1991) as follows:

$$w^{(1)} = g^{(1)}, \quad (4.21)$$

$$w^{(j)} = g^{(j)} + \gamma^{(j)} w^{(j-1)} \quad (j \geq 2), \quad (4.22)$$

where $\gamma^{(j)}$ is defined as

$$\gamma^{(j)} = \frac{Re \langle g^{(j)} - g^{(j-1)}, g^{(j)} \rangle_D}{\|g^{(j-1)}\|_D^2}, \quad (4.23)$$

and $g^{(j)}$ is the gradient of the cost functional $F^{(j)}$ with respect to the contrast $\sigma^{(j)}$.

The gradient $g^{(j)}$ is given by (Kleinman and van den Berg, 1991; Zhdanov, 2002):

$$g^{(j)} = -\frac{\mathbf{G}_D^\dagger \mathcal{E}^{(j-1)} + \beta \sigma^{(j-1)}}{\|v^d\|_S^2}, \quad (4.24)$$

where the operator $\mathbf{G}_D^\dagger \mathcal{E}^{(j-1)}$ can be found in equation (4.15). The residual error $\mathcal{E}^{(j-1)}$ is given in equation (4.16).

Once we have obtained the new contrast function $\sigma^{(j)}$, we can update the wave field $v_k^{(j)}$ inside the scattering domain \mathcal{D} by solving the integral equation (2.50).

In order to determine the *step size* $\alpha^{(j)}$, we substitute equation (4.20) into equation (4.18), upon which minimizing for variation of $\alpha^{(j)}$ leads to

$$\frac{Re \langle \varepsilon^{(j-1)} - \alpha^{(j)} \mathbf{G}_S w^{(j)}, \mathbf{G}_S w^{(j)} \rangle_S + \beta \|\sigma^{(j)}\|^2}{\|v^d\|_S^2} = 0. \quad (4.25)$$

From the above relation, we obtain,

$$\alpha^{(j)} = \frac{\langle \varepsilon^{(j-1)}, \mathbf{G}_S w^{(j)} \rangle_S}{\|\mathbf{G}_S w^{(j)}\|_S^2 + \beta \|w^{(j)}\|_D^2}. \quad (4.26)$$

4.4 Inversion Algorithm

A flow diagram of our inversion method is depicted in Figure 4.2.

In summary, our iterative inversion scheme can be described as follows:

- Input (step 1)
 - Compute the scattered wave field v^d in the frequency domain by taking the Fourier transform of the observed time domain data.
 - Choose the initial contrast ($\sigma^{(0)} = 0$).
- Inversion
 - Perform the computation (step 2) of:
 - * the wave field in the scattering domain \mathcal{D} .
 - * the scattered wave field v^{sc} at the receivers (at \mathcal{S}).
 - Evaluate the residual error using equation (4.18).
 - Check if $\frac{\|v^d - G_S \sigma^{(j)}\|^2}{\|v^d\|^2}$ is small enough (step 3); if not:
 - Calculate the step size $\alpha^{(j)}$ and direction $w^{(j)}$ with equation (4.26) and (4.21).
 - Determine the new contrast, $\sigma^{(j)} = \sigma^{(j-1)} + \alpha^{(j)} w^{(j)}$ and go back to step 2.
 - If the residual is small enough, the iterative process is terminated and the current value is accepted as the estimate.
- Output: Contrast estimate.

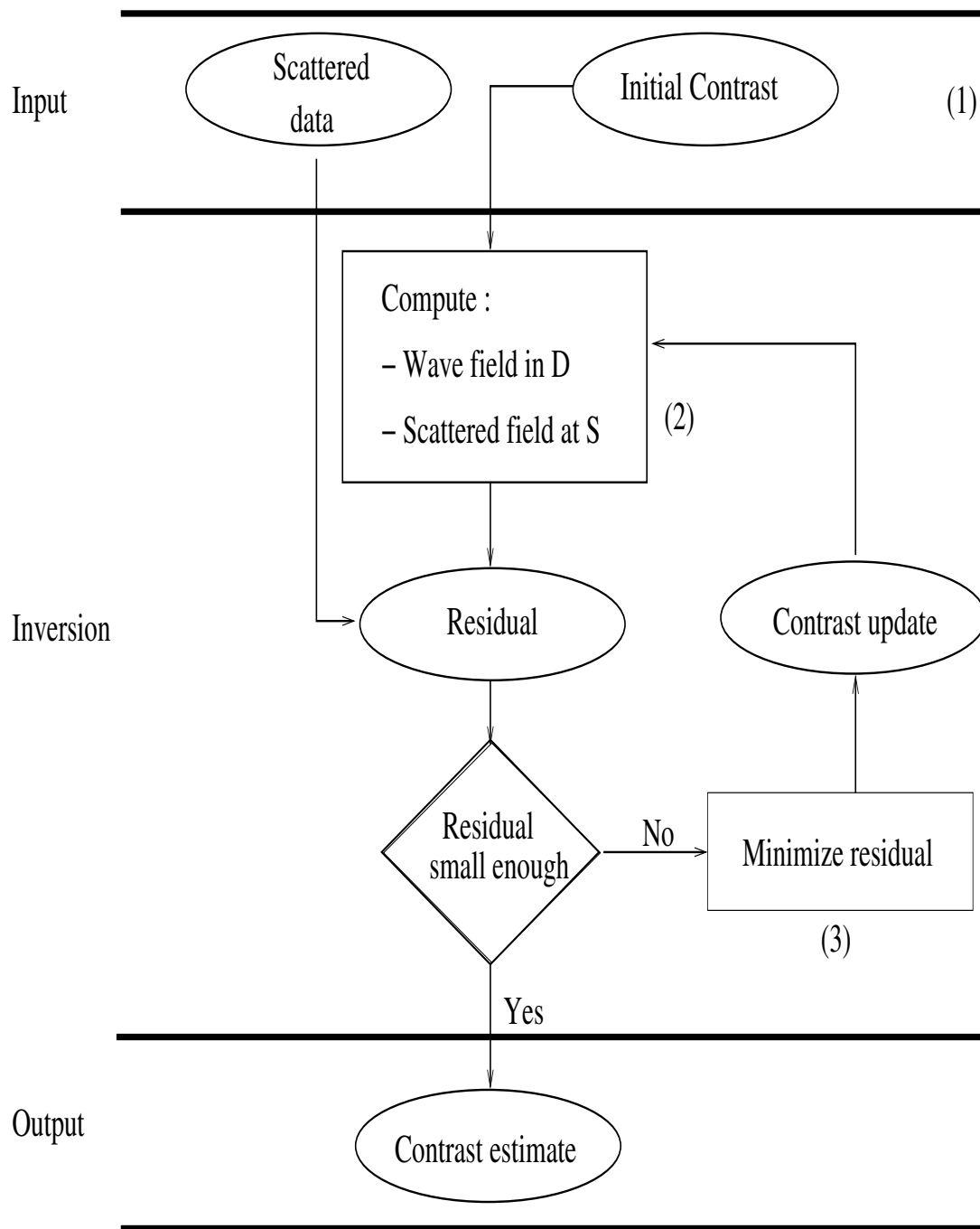


Figure 4.2: A flow diagram of the inversion scheme.

Numerical Results for the Inverse Problem

The inversion algorithm discussed in the previous chapter is aimed at the reconstruction of scattering medium parameters from scattered surface waves. In this chapter, we apply the inversion algorithm to synthetic scattered data computed with the integral-equation method discussed in Chapter 2. The model used to generate synthetic data contains a scatterer placed at different depths.

Because the Rayleigh wave attenuates with depth, our main interest is to investigate up to what depth we can resolve the parameters. As the inversion is time consuming, we restrict ourselves to considering a small scattering object.

Our inversion scheme is quite general as it takes into account the full elastic wave field and it does not rely on the Born approximation. This makes it useful for comparing it to schemes that are based on the Born approximation or that use approximations to the elastic wave field. Such comparisons are presented at the end of this chapter.

5.1 Results for a Small-Contrast Model

In principle, vertical structure can be inferred from the modal amplitudes of surface waves, because different modes sample different parts of the subsurface. In global seismology this property is used to construct upper-mantle shear-velocity structure models (for example Nolet, 1977), while in engineering geophysics this is used to obtain stiffness profiles (Stokoe et al., 1994; Bodet et al., 2004). In this section, we investigate if we can resolve the depth of a scatterer near the surface from inversion of *scattered* surface waves.

5.1.1 Description of the Model

We expect a strong relationship with the number of frequencies that we use in the algorithm and therefore, we start with a relatively simple test model. This model is shown in Figure 5.1.

The source is excited at position $x = 0, y = 0$ m at the surface of the model. We have a dominant frequency of 25 Hz. The S - and P -velocities of the embedding medium are 1000 m s^{-1}

and 3000 m s^{-1} , respectively, and its density is $\rho^0 = 1500 \text{ kg m}^{-3}$. The dominant Rayleigh wavelength is 40 m. The top of the scattering domain is located 5 m below the surface. This domain is divided into three cells at different depths ($\sigma_1, \sigma_2, \sigma_3$). The volume of each cell is $10 \times 10 \times 10 \text{ m}^3$ and the densities are $\rho_1^e = \rho_2^e = 1500 \text{ kg m}^{-3}$ for the first and second scatterers (no contrast in these domains, $\sigma_1 = \sigma_2 = 0$) and $\rho_3^e = 1600 \text{ kg m}^{-3}$ for the third scatterer (i.e. the contrast function $\sigma_3 = 100$).

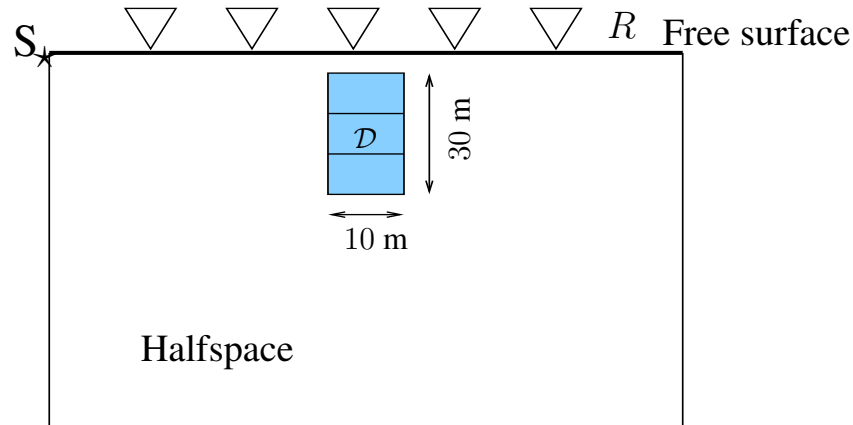


Figure 5.1: Cross section of 3D near-surface model with heterogeneity in (layered) half space. The source S is located at the origin. The receivers R are located at the surface. The scattering domain \mathcal{D} is divided into 3 cells at different depths.

The vertical velocity of the scattered wave field is calculated using the integral-equation method discussed in Chapter 2. Figure 5.2(a) shows the vertical velocity of the total wave field as a function of time and receiver position. From this figure, we cannot clearly see the scattered surface wave. This is because the scattered surface wave field is weak compared to the incident wave. If we subtract the incident wave field from the total wave field, we obtain the scattered wave field. The result of the scattered wave field is displayed in Figure 5.2(b), where we have scaled the result to show the scattered wave field more clearly.

Using these synthetic data, we determine the properties of the near-surface heterogeneities with the help of the inversion scheme discussed in Chapter 4.

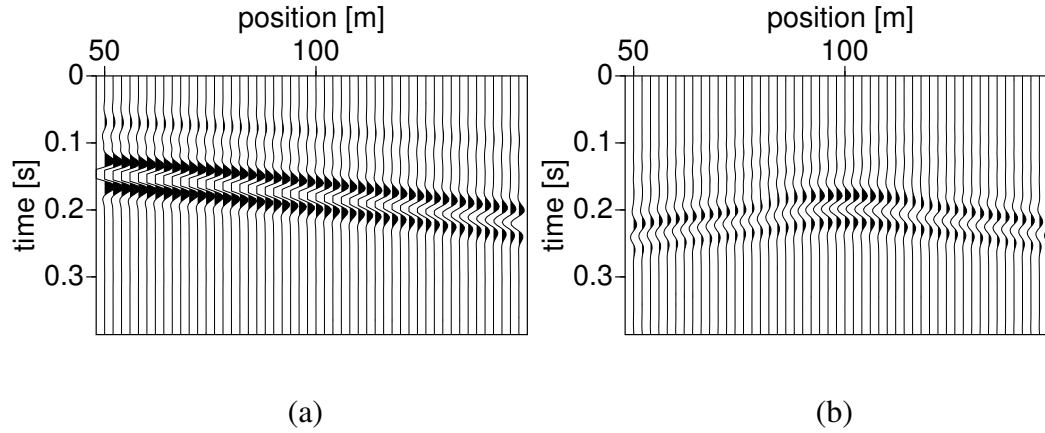


Figure 5.2: *The vertical velocity of the total wave field (a) and the scattered wave field (b). Note that the scale of the total wave field is 100 times larger than the scale of scattered wave field.*

5.1.2 Inversion Using a Single Frequency versus Several Frequencies

In the inversion, we consider the same size of scatterer domain used to generate the synthetic data (illustrated in Figure 5.1). The inversion domain is also divided into 3 grid points. Thus, we have 3 unknown contrasts (i.e. $\sigma_1, \sigma_2, \sigma_3$).

Employing our inversion algorithm, we want to estimate the contrast function in each cell. To do so, we consider inversion with a single frequency (i.e. the dominant frequency) and several frequencies (5 frequencies) in the inversion scheme.

In order to calculate the residual error between the actual scattered field and the modeled scattered field (using equation 4.4) in each iteration j , we use the residual error of the following form (see equation 4.18):

$$\|r^{(j)}\|_{\mathcal{S}}^2 = \frac{\|v^d - v^{sc,(j)}\|_{\mathcal{S}}^2}{\|v^d\|_{\mathcal{S}}^2} + \beta \|\sigma^j\|_{\mathcal{D}}^2, \quad (5.1)$$

where v^d is the actual scattered field, and $v^{sc,(j)} = \mathbf{G}_{\mathcal{S}}\sigma^{(j)}$ is the scattered field for the contrast $\sigma^{(j)}$ at iteration j . In this example, we choose the regularization parameter β equals 0.

The residual error between the actual data and the modeled data is shown in Figure 5.3(a) as a function of the number of iterations. We see from this figure that the residual error decreases for both the single-frequency and several-frequency cases.

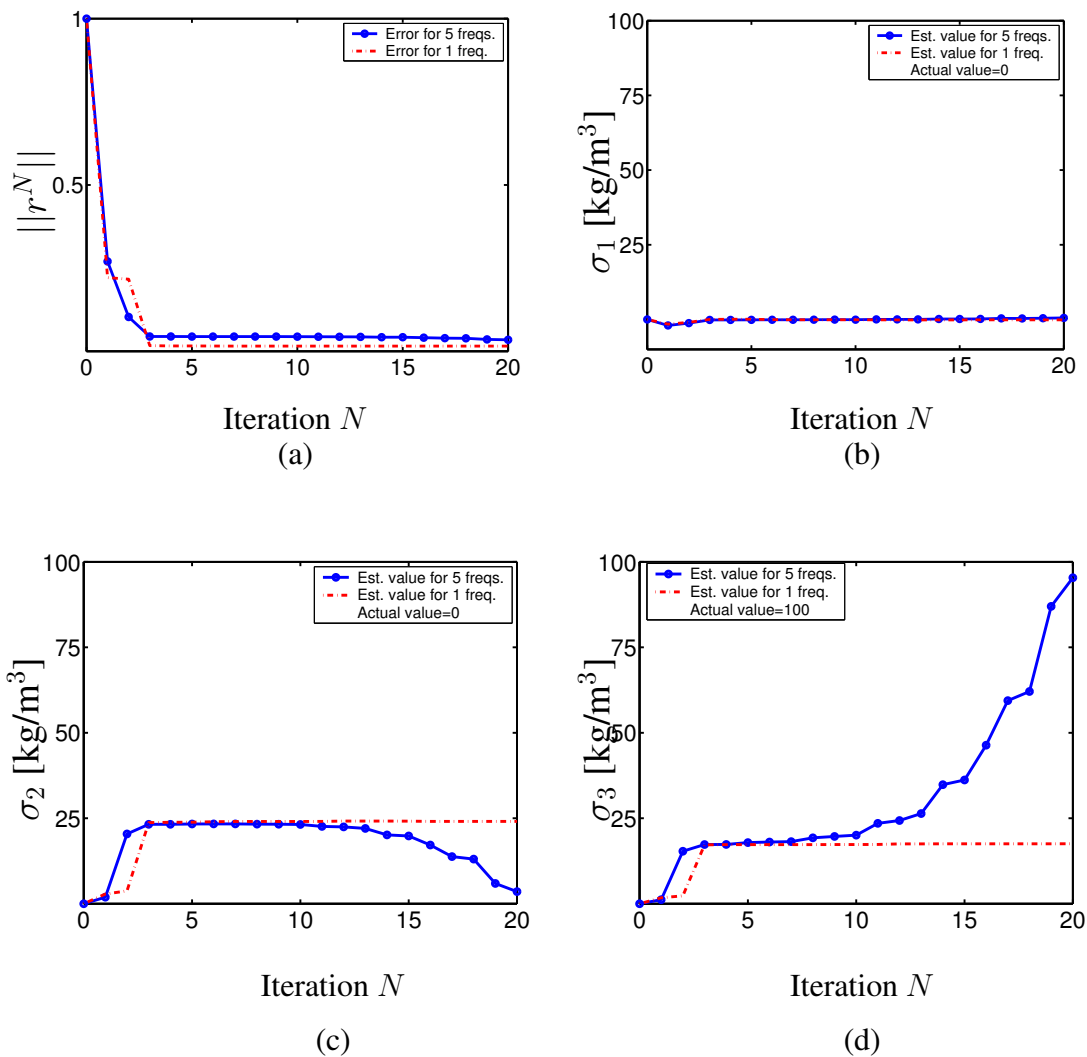


Figure 5.3: (a) The residual r^N as a function of the number of iterations for a single frequency and 5 frequencies. (b)-(d) The estimates of the contrast functions (σ_1 , σ_2 and σ_3) as a function of the number of iterations. Using a single frequency, the estimated values of the contrast do not approach the correct value although the residual error decreases. We also conclude that the deeper contrast converges slower.

The estimated values of the contrast using a single frequency and 5 frequencies as a function of the number iterations are displayed in Figure 5.3(b)-(d) for σ_1 , σ_2 and σ_3 , respectively.

If we now look at the estimated values of the contrast for the first estimated contrast σ_1 (Figure 5.3(b)) we get the same result for both the single frequency and several-frequency cases. However, if we look at the results for σ_2 and σ_3 , we observe that the results differ (Figure 5.3(c) and (d)). From these figures, we see that if we include 5 frequencies the estimated values converge to the actual values of the contrast in the cells. If we use one frequency, however, the value in σ_2 is overestimated, while the contrast in σ_3 is underestimated. This example demonstrates that with only one frequency we cannot resolve the depth of the scatterer. Including five frequencies we are able to get a good estimate of the contrast with depth. This is because the five frequencies sample different parts of the subsurface and, therefore, their combination is sensitive to the depth of the scatterer.

In Table 5.1, we give the estimated values of the contrast obtained after 20 iterations from both the single- frequency and five-frequency cases.

	Actual value	Est. value using 1 freq.	Est. value using 5 freqs.
σ_1 [kg/m ³]	0	-0.124	0.518
σ_2 [kg/m ³]	0	24.083	3.538
σ_3 [kg/m ³]	100	17.558	95.352

Table 5.1: Comparison between the actual values and the estimated values of the contrast function using a single frequency and 5 frequencies.

5.1.3 Effect of Parameterization

Our main aim in the previous examples was to investigate the depth dependence of the estimated contrasts. Because the inversion procedure is computationally expensive, we have used the fact that the spatial location of the scatterer was known. If this location is not known, we need to increase the lateral size of the image domain. In the following test, we increase the image domain and we shift the grid (to avoid the "inverse crime" (Colton and Kress, 1998)). The position of the inversion model is shifted 5 m in the vertical- and horizontal directions. The geometry of the model is depicted in Figure 5.4. In this figure, the inversion domain is represented by \mathcal{D}^{inv} and the actual domain is denoted by \mathcal{D} .

In the inversion, the size of the inversion domain \mathcal{D}^{in} is $30 \times 10 \times 30$ m³. The inversion domain is then subdivided into equal-sized cells, $\Delta x = \Delta y = \Delta z = 10$ m. The total amount of grid points is equal to 9 grid cells.

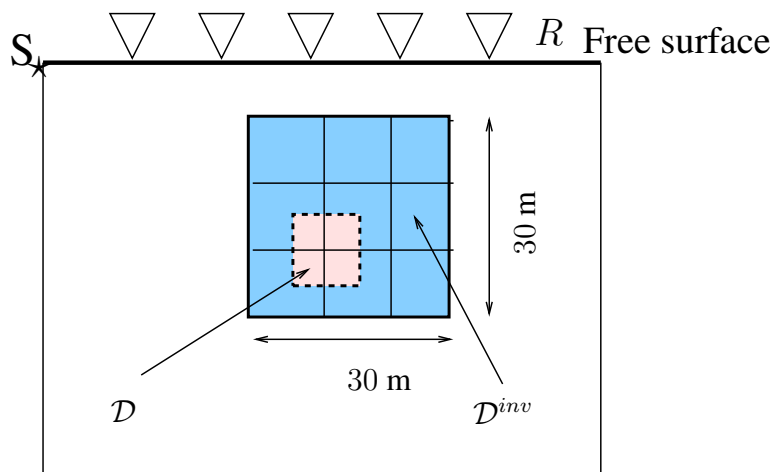


Figure 5.4: Cross section of 3D near-surface model with heterogeneity in (a layered) half space. The source S is located at the origin. The receivers R are located at the surface. The actual scatterer domain \mathcal{D} is illustrated by the dotted line (the same domain as in Figure 5.1). The scatterer domain used in the inversion is given by \mathcal{D}^{inv} with the size of $30 \times 10 \times 30 \text{ m}^3$.

We use a tolerance of the residual error (equation (5.1)) of 0.1 percent. We stop the iteration process when the error is smaller than the tolerance. After 40 iterations, the tolerance is attained. The results of the estimated values of the contrast function are given in Figure 5.5. The estimated values converge to the actual values of the contrast for cells with a depth of about one wavelength. We cannot completely resolve the contrast for the deeper cells. This is most probably due to the fact that the surface waves decay exponentially with depth and the decay depends on the Rayleigh wavelength (Aki and Richards, 2002). However, taking into account that the grid is coarse we obtain a reasonable estimate of the location of the scatterer and a good estimate of the actual contrast.

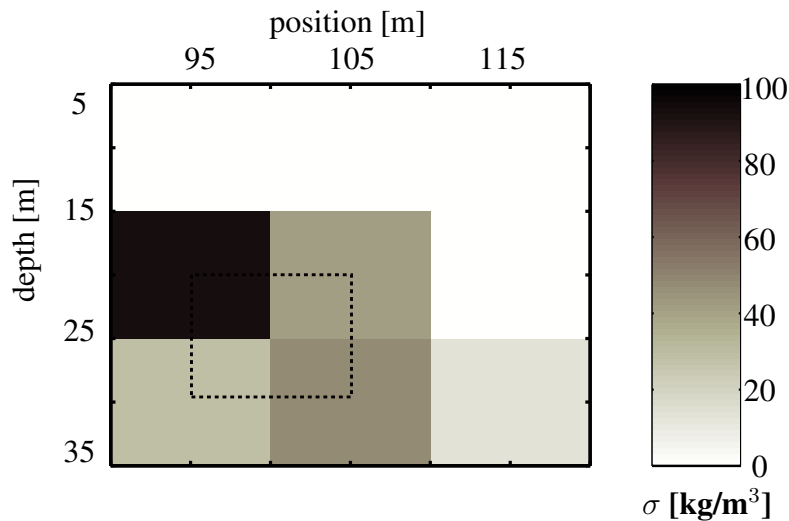


Figure 5.5: The estimated values of the contrast function after 40 iterations. The actual value of the contrast is 100 kg/m^3 .

5.2 Results for a Strong-Contrast Model

5.2.1 Description of the Model: Weak Contrast (Case 1) versus Strong Contrast (Case 2)

In this investigation, we consider a similar geometry as shown Figure 5.1, but now containing a weak contrast (case 1) and strong contrast (case 2). For weak contrast, the contrast functions are given by $\sigma_1 = \sigma_2 = \sigma_3 = 100 \text{ kg m}^{-3}$ while for the strong contrast, the contrast functions are given by $\sigma_1 = \sigma_2 = \sigma_3 = 2000 \text{ kg m}^{-3}$. The total wave fields for both cases are shown in Figure 5.6(a)-(b) as a function of time and receiver position. For the strong contrast given in Figure 5.6(b), we observe that the energy of the scattered Rayleigh waves is comparable to the incident wave field. After transforming to the frequency domain, the scattered wave fields serve as the input data in the inversion.

5.2.2 Inversion Using a Single Frequency versus Several Frequencies

In the inversion, it is assumed that the size of the inversion domain is the same as used to generate the synthetic data (as displayed in Figure 5.1). The inversion domain is also divided into 3 grid cells (σ_1, σ_2 and σ_3).

The results of the estimated values for different frequencies (for the same residual error, $r = 0.001$) are shown in Figure 5.7(a) for the weak contrast and in (b) for the strong contrast.

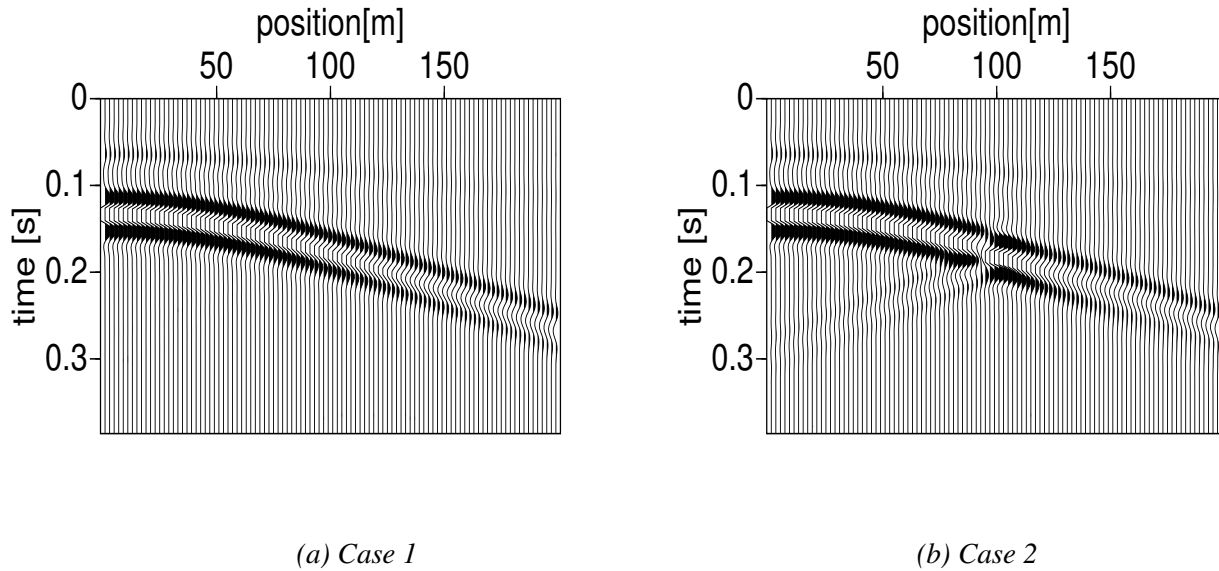


Figure 5.6: *The measured wave field for weak contrast (a) and for strong contrast (b). For the stronger contrast, the energy of the scattered Rayleigh waves is comparable to the incident field.*

In Figure 5.7(a), we see that by including 4 frequencies in the inversion scheme, the estimated values converge to the actual values of the contrast in the cells. Meanwhile, in Figure 5.7(b), we see that by including 10 frequencies in the inversion scheme, we obtain a good result of the estimated values in the cells. From these figures, we conclude that the strong contrast needs more frequencies and this dependence is stronger for the deeper contrasts.

Figure 5.8 shows the residual error between the actual data and the modeled data for the strong contrast case as a function of the number iterations. In this figure we see that after 11 iterations when the residual error equals $3 \cdot 10^{-3}$, we obtain the contrast value for the deeper cell to be equal to $\sigma_3 = 1102.74$. But after 12 iterations, the residual is equal to $1 \cdot 10^{-3}$, the contrast value jumps to $\sigma_3 = 1801.54$. This implies that a small decrease of the residual has a large influence on the deeper σ_3 .

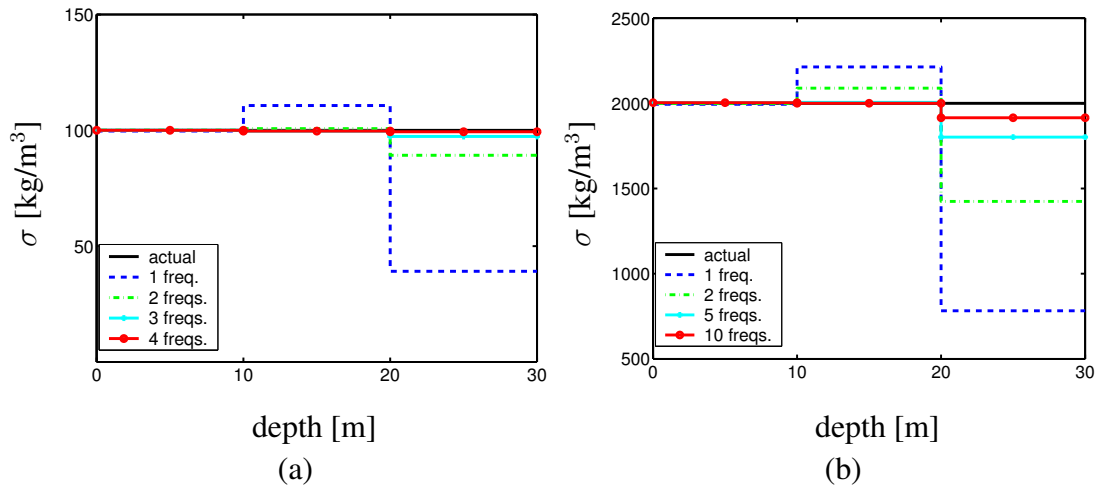


Figure 5.7: The results for different frequencies (for the same residual error, $r = 0.001$). (a) For weak contrast, and (b) for strong contrast. From this figure, we observe that the strong contrast needs more frequencies.

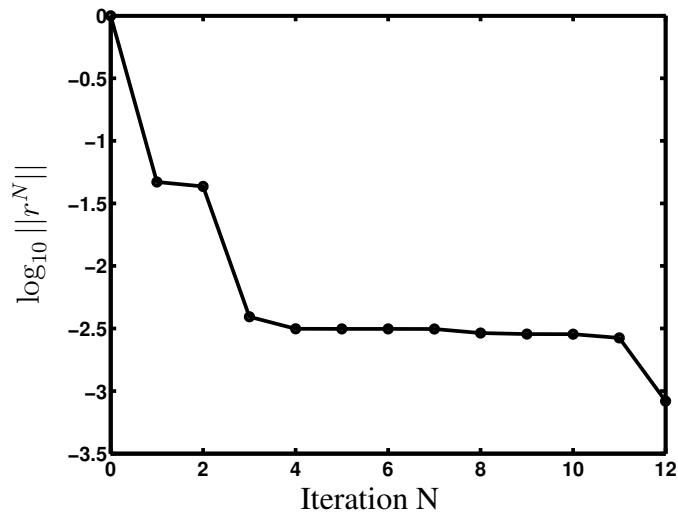


Figure 5.8: The residual error for the larger contrasts as a function of the number of iterations.

5.2.3 Effect of Parameterization

In the following test, we increase the size of the inversion domain to $50 \times 10 \times 30 \text{ m}^3$, while the size of the actual scattering domain is $10 \times 10 \times 30 \text{ m}^3$. The configuration of the model is depicted in Figure 5.9. In this Figure, the inversion domain is represented by \mathcal{D}^{inv} and the actual domain is denoted by \mathcal{D} . In order to estimate the contrast function, we subdivide the inversion domain \mathcal{D}^{inv} into equal-sized cells, $\Delta x = \Delta y = \Delta z = 10 \text{ m}$. The total amount of grid points is equal to 15 grid cells.

In Figure 5.10, we show the results of the contrast function for the weak contrast (Case 1).

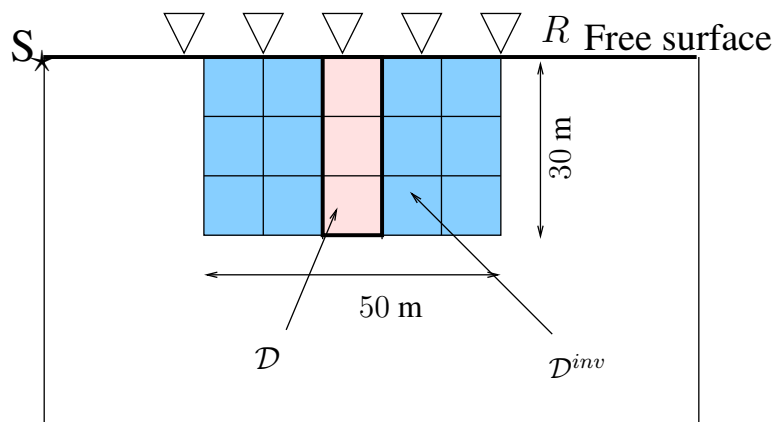


Figure 5.9: Configuration of the inversion model. The actual scattering domain is denoted by \mathcal{D} and the target scattering domain used in the inversion is denoted by \mathcal{D}^{inv} .

In the calculation, it takes 21 iterations to obtain the residual error of 0.1 %. From the figure, we see that we can obtain a good estimate of the contrast function at the correct location.

The results of the estimated values of the contrast function for the strong contrast case are shown in Figure 5.11. In the calculation, we need 115 iterations for obtaining a residual error of 0.1 %. From this figure, we also see that we can obtain a good estimate for the strong contrast case. The deeper scatterer is hardest to estimate. We conclude that the scatterer should not be deeper than about one Rayleigh wavelength.

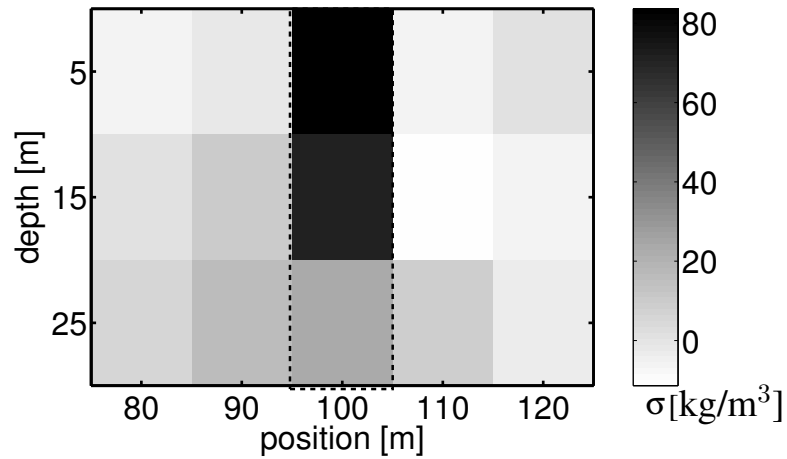


Figure 5.10: The results of the estimated values for weak contrast after 21 iterations a the residual error of $r = 0.1\%$. The correct value of the contrast is 100 kg/m^3 .

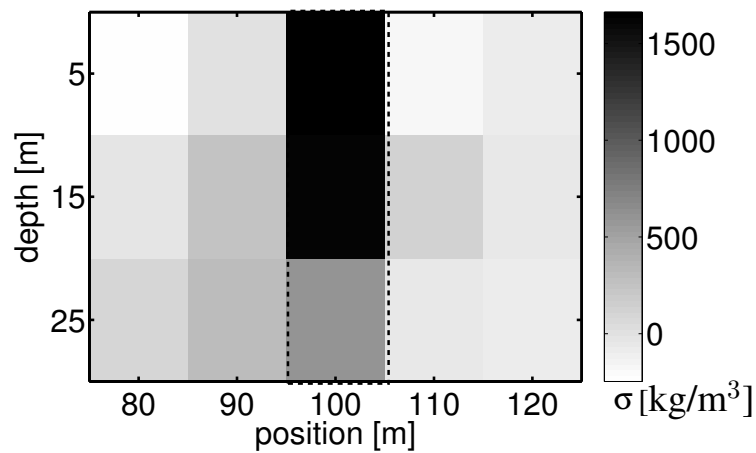


Figure 5.11: The results of the estimated values for strong contrast (b) after 115 iterations with the residual error of $r = 0.1\%$. The correct value of the contrast is 2000 kg/m^3 .

5.2.4 Comparing the Results to the Born Approximation and the Effect of Interaction Between Different Components

The integral representation of the vertical velocity of the modeled scattered wave field is given by:

$$v^{sc} = \mathbf{G}_S \sigma, \quad (5.2)$$

where the operator \mathbf{G}_S is defined by

$$\{\mathbf{G}_S \sigma\}(\mathbf{x}) = \omega^2 \int_{\mathbf{x}' \in \mathcal{D}} u_k^G(\mathbf{x}, \mathbf{x}') v_k(\mathbf{x}', \mathbf{x}^s) \sigma(\mathbf{x}') dV, \quad \mathbf{x} \in \mathcal{S}. \quad (5.3)$$

As mentioned in Chapter 4, the inverse problem is non linear since the wave field in the scattering domain depends on the properties of the contrast function. In the inversion, an approach can be used to linearize the representation, for example using the Born approximation (Snieder, 1986; Kleinman and van den Berg, 1991; Blonk and Herman, 1994; Kaslilar et al., 2005). Then, the inverse problem becomes a linear inverse problem.

In the Born approximation, it is assumed that the wave field in the scattering domain can be approximated by the incident wave field in the scattering domain if the contrast function is small. The integral representation given by equation (4.4) can then be rewritten as follows:

$$v^{sc} = W(\omega) \omega^2 \int_{\mathbf{x}' \in \mathcal{D}} u_k^G(\mathbf{x}, \mathbf{x}') v_k^G(\mathbf{x}', \mathbf{x}^s) \sigma(\mathbf{x}') dV, \quad \mathbf{x} \in \mathcal{S}, \quad (5.4)$$

where $W(\omega)$ is the source wavelet, u_k^G is the Green's tensor of the embedding and v_k^G is the incident wave field replacing the total wave field inside \mathcal{D} .

In this way the inversion becomes less time consuming because we do not have to update the wave field in the scatterer at each iteration.

From equation (5.3), we see that the integral consists of three components of the Green's tensor u_k^G , three components of the wave field acting on the scattering domain (v_k , $k = 1, 2, 3$) and the contrast itself.

Another way to make the inversion more efficient is to consider an approximation to the elastic wave field. To reduce the complexity of this equation one can assume that the vertical component of the displacement dominates the horizontal ones, and there is no interaction between the components at the scatterer. In that way, the integral representation consists of only one term left and it is then written as follows (see Los et al., 2001; Campman et al., 2004a,b):

$$\{\mathbf{G}_S \sigma\}(\mathbf{x}) = \omega^2 \int_{\mathbf{x}' \in \mathcal{D}} u_3^G(\mathbf{x}, \mathbf{x}') v_3^G(\mathbf{x}', \mathbf{x}^s) \sigma(\mathbf{x}') dV, \quad \mathbf{x} \in \mathcal{S}. \quad (5.5)$$

It is only a valid approximation, if the scatterer domain is close to the receivers (see Los et al., 2001; Campman et al., 2004b).

In order to investigate the performance of the inversion using these approximate solutions, we compare the contrasts obtained with our inversion scheme discussed in Chapter 4, to these

obtained using the Born approximation (equation 5.4) and considering only the vertical component of the Born approximation (equation 5.5).

In the inversion, we use the input data as given in Figure 5.6. The inversion domain is also divided into 3 grid cells (i.e. σ_1, σ_2 and σ_3). Again, we consider the cases of weak and strong contrast. Employing our inversion scheme, we estimate the contrast values for both cases. We then compare the estimated results using the Born approximation and considering only the vertical component of the Born approximation.

The results are tabulated in Table 5.2 for weak contrast and Table 5.3 for strong contrast. We can see from these tables that the estimated value of σ_1 (shallowest one) leads to the right value for all methods. If we consider the next cells (σ_2 and σ_3), we see that the estimated values using all components of the Born approximation and our inversion scheme (actual field) are also close to the actual contrast. But by considering only the vertical component of the Born approximation, we obtain inaccurate results for σ_2 and σ_3 . This result is consistent with the results of Campman et al. (2004a,b).

	Born Approx. all components	Born approx. only vertical component	our method all components	Actual value
σ_1 [kg/m ³]	100.48	96.02	100.05	100.00
σ_2 [kg/m ³]	99.33	-11.15	99.53	100.00
σ_3 [kg/m ³]	72.85	562.91	98.92	100.00

Table 5.2: Case 1: Comparison between the estimated values of the contrast function using the Born approximation, the vertical component of the Born approximation and our full inversion method.

	Born Approx. all components	Born approx. only vertical component	our method all components	Actual value
σ_1 [kg/m ³]	2010.24	1926.62	2003.64	2000.00
σ_2 [kg/m ³]	1999.12	-130.289	2005.58	2000.00
σ_3 [kg/m ³]	1410.64	10726.07	1801.54	2000.00

Table 5.3: Same as Table 5.2, but now for strong contrast (Case 2).

These cases illustrate that we cannot resolve the depth of the scatterer using only the vertical component of the Born approximation. Moreover, for the large contrast, we conclude that

accounting for the interaction between all components is more important than the Born approximation.

5.3 Imaging Examples Using the Born Approximation

In the previous section, we showed that reasonably good quantitative inversion results can be expected from using the Born approximation. Because inversion using this approximation is less time consuming than the full non-linear inversion, we applied the Born approximation method to synthetic data to obtain images of near-surface heterogeneities. Examples of applications are exploration for aquifers or archeological surveys. While we can also employ the full non-linear inversion to obtain images of the near-surface heterogeneities, the cpu-time needed becomes prohibitively large for the present example. This is because for each iteration we update both the wave field inside the scatterers and the contrast.

As an example, we consider synthetic data generated from the forward model. The model to generate the data is the same as the one used in Subsection 3.6.2. We use the Born approximation for the integral representation (5.4) (discussed by Kaslilar et al., 2005). In the inversion, we use the same model and geometry as used for the forward model and try to estimate the location of the scatterer and the actual contrast value. The configuration of the model is depicted in Figure 5.12.

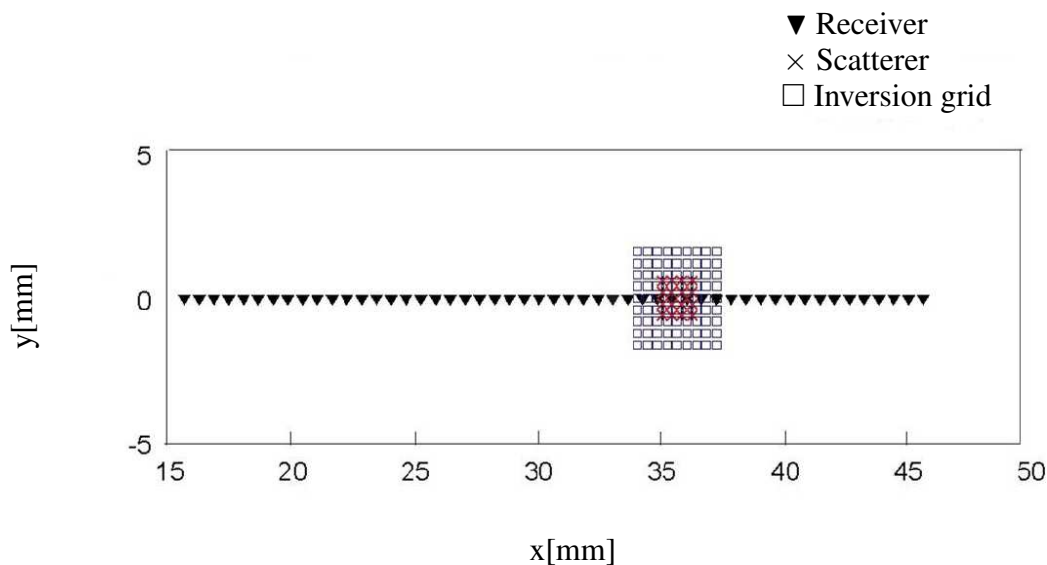


Figure 5.12: Configuration of the inversion model.

The image obtained from this computed data is shown in Figure 5.13. The dashed box shows the actual location of the scatterer. The receiver line is placed along a-b. Figure 5.13(i) is the top view of the image. The highest contrast, nearly the actual contrast value, is estimated along the receiver line. The contrast value decreases on both sides of the receiver lines (crossline c-d). The cross sections along lines a-b (Figure 5.13(ii)) and c-d (Figure 5.13(ii)) show the side view of the image. The image is blurred on both sides due to the finite resolution of the imaging method. The images of Figure 5.13 show that we can locate the scatterer accurately and obtain a fairly accurate estimate of the actual contrast value.

In the next test, we consider a model with two different densities in the vertical direction. Both layers have a thickness of about $\lambda/4$. The shallow and deep layers have density values of $\rho = 4.0 \times 10^{-6} \text{ kg/mm}^3$ and $\rho = 7.0 \times 10^{-6} \text{ kg/mm}^3$, respectively, while other parameters remain the same as in the first model. The top view of the image for the shallow and deep layer is shown in Figures 5.14(i) and (ii), respectively. We can locate the scatterer at both depths, although locating the deeper scatterer becomes more difficult. The estimated contrast values are approximately the average of both scatterers.

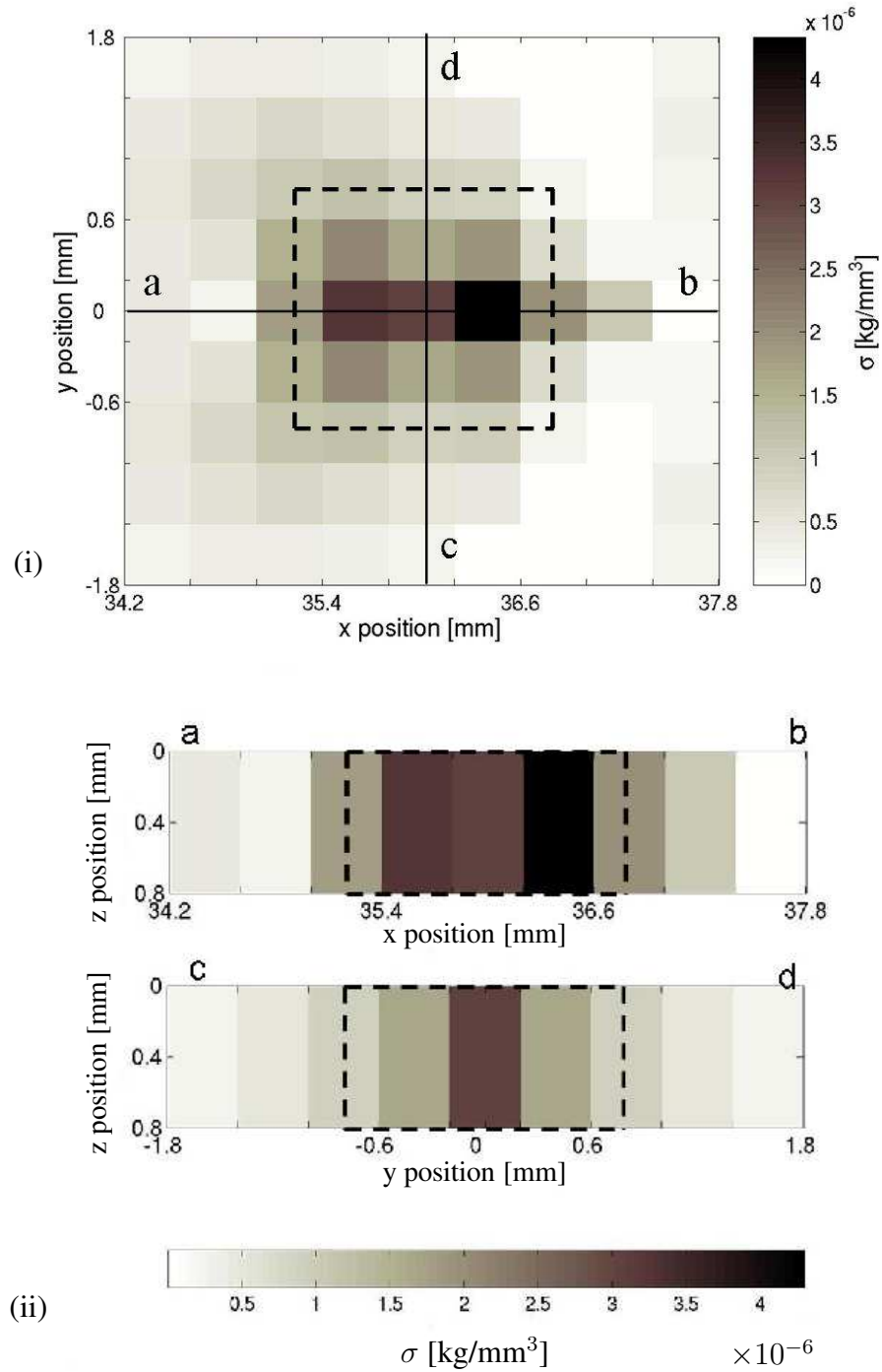


Figure 5.13: (i) Top view of the image. (ii) Cross sections a-b and c-d. The actual scatterer is indicated by the dashed line. The correct value of the contrast is 4.3×10^{-6} kg/mm³

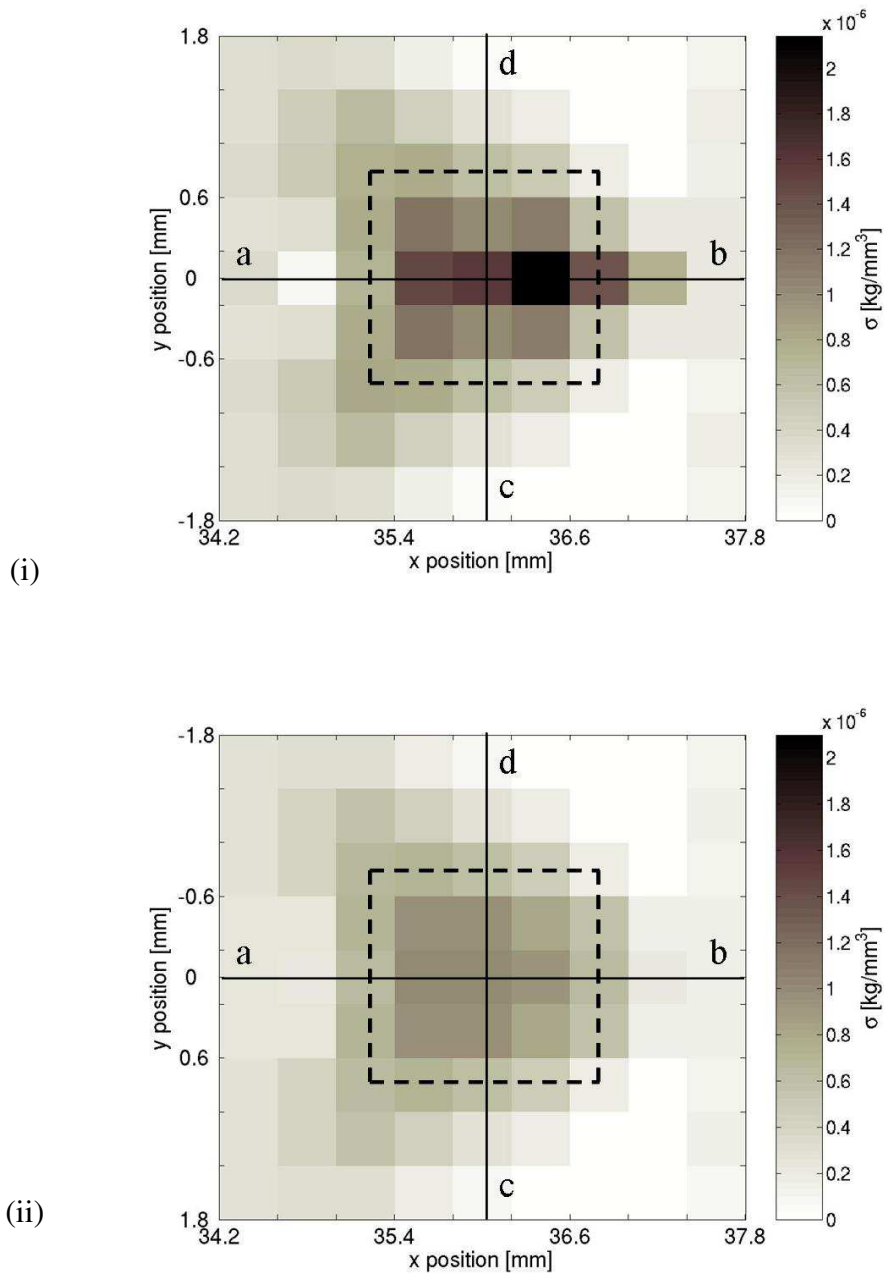


Figure 5.14: (i) Top view shallow layer. (ii) Top view deeper layer. The actual scatterer is indicated by the dashed line. The correct values of the contrast of the shallow and deep layers are $1.3 \times 10^{-6} \text{ kg/mm}^3$ and $4.3 \times 10^{-6} \text{ kg/mm}^3$, respectively.

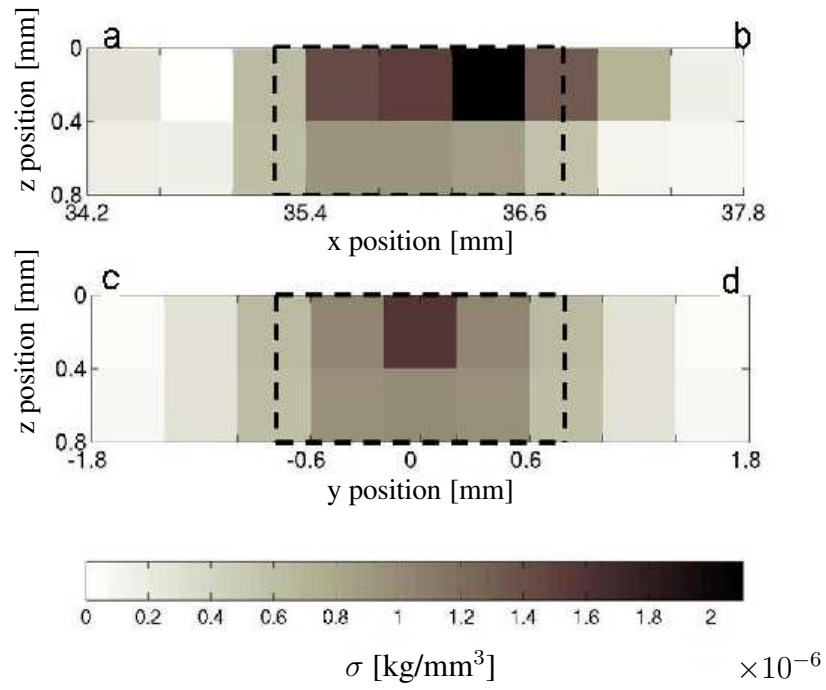


Figure 5.15: Cross sections a-b and c-d. The actual scatterer is indicated by the dashed line.

Conclusion and Discussion

In this thesis, we developed an efficient and accurate modeling method for the near-field scattering problem by 3D near-surface heterogeneities close to the receivers or sources. The method is based on a domain-type integral representation. The method is specifically tailored to model the wave field excited by an incident wave field impinging on inclusions close to the free surface of a layered embedding. In this case the dominant part of the secondary wave field consists of surface waves. Our method can handle large scatterers and strong contrasts when compared to ray/Born methods and also includes multiple scattering. The integral-equation method thus proves useful for modeling near-surface scattering problems which are relevant to both the exploration and the global seismology community.

For observation points inside the scattering domain, we obtain a domain integral equation of the second kind, involving the impulse response (Green's tensor) of the embedding, a contrast function and the unknown wave field in the domain occupied by the scatterer. We apply the method of moments to solve this domain integral equation. By dividing the scattering domain into a number of cells whose sizes are small enough when compared to the smallest wavelength, we approximate the unknown wave field by a set of basis functions.

We reduce the time of calculating the system matrix by considering the Green's tensor in terms of Bessel functions. We also present a method for accelerating the convergence of the computation of the Green's tensor by subtracting the free-space Green's tensor when the observation and the scatterer points are located close to each other. We furthermore improve the efficiency by implementing our method on a cluster of workstations (each frequency is computed independently).

In a number of model studies, we have analyzed the effect of the 3D near-surface heterogeneities close to the receivers. In the first models, we consider a horizontal plane-wave source to simulate an upcoming reflection from the deeper subsurface. From the results, we observe that the P wave is delayed above the anomaly. We conclude that the dominant effect on the vertical component is the excitation of Rayleigh waves. We also observe time shifts and interference due to scattered Rayleigh waves. By increasing the size of the scattering domain and considering a random model, the complexity of the interference patterns due to scattered Rayleigh waves in the coda following the P wave increases. Interference of these waves can cause irregularities in the wave front.

Two comparisons of the numerical results obtained using our modeling method with experimental data collected in Colorado School Mines (CSM) have also been made. In both comparisons, we consider a similar geometry for the horizontal plane-wave source and for the point source located at the surface. We show that both results are in a good qualitative and quantitative agreement. We observe in both results that the P wave is delayed above the anomaly. We also observe time shifts and interference due to scattered Rayleigh waves.

Based on the integral representation, we formulate the inverse problem for scattered surface waves. It is our objective to estimate the properties of near-surface heterogeneity, given the scattered field at the surface. The inversion is based on minimizing an error function consisting of the squared difference between the actual scattered field and the scattered field calculated with the integral representation. The inversion algorithm is aimed at the reconstruction of scattering medium parameters from scattered surface waves. We apply the inversion algorithm to synthetic data computed with the integral-equation method. The model used to generate the synthetic data contains a scatterer placed at different depths. Because the Rayleigh wave attenuates with depth, our main interest is to investigate up to what depth we can resolve the parameters. As the inversion is time consuming, we restrict ourselves to considering a small scattering object. We observe that we can obtain a good estimate of the contrast function at the correct depth upto about a depth of about one Rayleigh wavelength.

The computational complexity of our inversion scheme makes it less suitable for inversion of data sets from practical experiments. Nonetheless, our limited-sized inversion studies give insight in the inversion of scattered surface waves. Our inversion scheme is quite general as it takes into account the full elastic wave field and does not rely on the Born approximation. This makes it well-suited for comparing schemes that are based on the Born approximation or that use approximations to the elastic wave field. Such comparisons are also presented.

In the calculation of the integral-equation method, we derive the Green's tensor elements in terms of Bessel functions. Having such expressions of the Green's tensor, another efficient way to compute the Green's tensor elements can be achieved by considering radial symmetry of the Green's tensor and interpolating the Green's tensor elements in distance. This method has been proposed by Kaslilar et al. (2005). Combining this method and our method for calculating the Green's tensor, one can obtain a more efficient method for modeling and inversion of scattered surface waves.

In this thesis, we develop the integral equation method by considering a density contrast only. However, our method can be extended to contrast in Lamé parameters. By taking into account the Lamé parameters, we obtain a coupled system of equations based on the integral representation of the displacement and an integral representation of the stress. These equations can be solved with a similar computational method as the one we discussed in Chapter 2.

Bibliography

- Abma, R. (1994) *Techniques for determining the structure and properties of permafrost*, SEP-80.
- (2002) *Time corrections for high-velocity near-surface layers*, in: Exp. Abstr., 72nd Ann. Inter. Mtg., Soc. Expl. Geophys., Tulsa, OK, USA, pp. 2039–2042.
- Abramowitz, M. and Stegun, I. (1968) *Handbook of Mathematical Functions*, Dover Publications, NY, USA.
- Achenbach, J. D. (1973) *Wave propagation in elastic solid*, North-Holland Publishing Company.
- Aki, K. and Richards, P. G. (2002) *Quantitative seismology*, University Science Books.
- Bannister, S. C., Husebye, E. S., and Ruud, B. O. (1990) *Teleseismic P-code analyzed by three-component and array techniques-deterministic location of topographic P-Rg scattering near the Noress array*, Bull. Seis. Soc. Am., **80**, pp. 1969–1986.
- Berni, A. J. and Roeber, W. L. (1989) *Field-array performance: Theoretical study of spatially correlated variations in amplitude coupling and static shift in the Paris basin*, Geophysics, **32**, pp. 451–459.
- Blonk, B. and Herman, G. C. (1994) *Inverse scattering of surface waves : A new look at surface consistency*, Geophysics, **59**, pp. 963–972.
- Blonk, B., Herman, G. C., and Drijkoningen, G. G. (1995) *An elastodynamic inverse scattering method for removing scattered surface waves from field data*, Geophysics, **60**, pp. 1897–1905.
- Bodet, L., van Wijk, K., Bitri, A., Abraham, A., Cote, P., Grandjen, G., and Leparoux, D. (2004) *Surface wave dispersion inversion when the 1D assumption breaks down*, Submitted to Journal of Environmental & Engineering Geophysics.
- Brigham, E. (1988) *The Fast Fourier Transform and Its Application*, Prentice-Hall, Inc, New Jersey.
- Campman, X. H., van Wijk, K., Riyanti, C. D., Scales, J., and Herman, G. C. (2004a) *Imaging scattered seismic surface waves*, Near Surface Geophysics, **2**, **4**, pp. 223–230.
- Campman, X. H., van Wijk, K., Riyanti, C. D., Scales, J. A., and Herman, G. C. (2004b) *Shallow imaging with scattered seismic surface waves*, In: Ext. Abstr., Near Surface 2004, Eur. Assn. Geosci. Eng., Session: B-026.

- Campman, X. H., van Wijk, K., Scales, J. A., and Herman, G. C. (2005) *Imaging and suppressing near-receiver scattered waves*, *Geophysics*, **70**, **2**, pp. V21–V29.
- Carcione, M. C., Herman, G. C., and ten Kroode, A. P. E. (2002) *Seismic modeling*, *Geophysics*, **67**, pp. 1304–1325.
- Clouser, R. H. and Langston, C. A. (1995) *Modeling observed P-Rg conversions from isolated topographic features near the NORESS array*, *Bull. Seism. Soc. Am.*, **85**, pp. 859–873.
- Colton, D. and Kress, R. (1998) *Inverse Acoustic and Electromagnetic Scattering Theory*, Springer-Verlag, New York.
- Combee, L. (1994) *Wavefield scattering by a 2-D near-surface elliptic anomaly*, in: *Exp. Abstr.*, 64th Ann. Internat. Mtg., Soc. of Expl. Geoph., pp. 1306–1309.
- (1995) *Scattering of the source-generated wavefield by a 2-D near-surface elliptic anomaly*, in: *Exp. Abstr.*, 65th Ann. Internat. Mtg., Soc. of Expl. Geoph., pp. 1325–1328.
- Cox, M. J. G. (1999) *Static corrections for seismic reflection surveys*, Soc. of Expl. Geophys.
- De Hoop, A. T. (1995) *Handbook of radiation and scattering of waves*, Academic Press.
- Ditzel, A. (2003) *Train-induced ground vibrations: modeling and experiments*, PhD thesis, Delft, University of Technology.
- Ditzel, A., Herman, G. C., and Drijkoningen, G. G. (2001) *Seismograms of moving trains: comparison of theory and measurements*, *Journal of Sound and Vibration*, **248**, **4**, pp. 635–652.
- Ernst, F. E. and Herman, G. C. (1998) *Removal of guided waves from seismic data in laterally varying media*, *Wave Motion*, **28**, pp. 173–189.
- Fokkema, J. T. and Van den Berg, P. M. (1993) *Seismic applications of acoustic reciprocity*, Elsevier.
- Gilbert, F. and Knopoff, L. (1960) *Seismic scattering from topographic irregularities*, *Journal of Geophysical Research*, **65**, **10**, pp. 3437–3444.
- Gropp, W., Lusk, E., and Skjellum, A. (1994) *Using MPI: Portable Parallel programming with Message-Passing Interface*, The MIT Press, Cambridge, Massachusetts.
- Hansen, P. C. (1997) *Rank-deficient and discrete ill-posed problems: Numerical aspects of linear inversion*, SIAM.
- Harrington, R. F. (1968) *Field computation by moments method*, MacMillan, New York.

- Harris, J. (2001) *Linear Elastic waves*, Cambridge University Press, Cambridge.
- Herman, G. C. (1982) *Scattering of transient elastic waves by inhomogeneous obstacle: contrast in volume density of mass*, *J. Acoust. Soc. Am.*, **71**, pp. 264–472.
- Herman, G. C., Milligan, P. A., Huggins, R. J., and Rector, J. W. (2000) *Imaging shallow objects and heterogeneities with scattered guided waves*, *Geophysics*, **65**, pp. 247–251.
- Herman, G. C. and Perkins, C. (2004) *Predictive scattered noise removal*, in: *Ext. Abstr.*, 66th Eur. Assn. Geophys. Eng., Session: D027.
- Hestholm, S. and Ruud, B. (1998) *3-D finite-difference elastic wave modeling including surface topography*, *Geophysics*, **63**, **2**, pp. 613–622.
- Hisada, Y. (1994) *An efficient method for computing green's functions for a layered half-space with sources and receivers at close depths*, *Bull. of the Seismological Soc. of Am.*, **84**, **5**, pp. 1456–1472.
- Hudson, J. A. (1967) *Scattered surface waves from a surface obstacle*, *Geophys. J. R. astr. Soc.*, **13**, pp. 441–458.
- Hughes, T. J. R. (1987) *The finite element methods: linear static and dynamic finite element analysis*, Prentice-Hall International, Inc.
- Jarem, J. M. (1986) *Method of moments solution of a parallel-plate waveguide aperture system*, *J. Appl. Phys.*, **59**, **10**, pp. 3566–3570.
- Kaslilar, A., Riyanti, C. D., Campman, X. H., and Herman, G. C. (2005) *Forward and inverse scattering of surface waves*, In: *Ext. Abstr.*, 66th EAGE Conference Madrid, Spain.
- Kennett, B. L. N. (1983) *Seismic wave propagation in stratified media*, Cambridge University Press.
- (2001) *The seismic wavefield; Volume I: Introduction and theoretical development*, Cambridge University Press.
- (2002) *The seismic wavefield; Volume II: Interpretation of seismograms on regional and global scales*, Cambridge University Press.
- Kleinman, R. E. and van den Berg, P. M. (1991) *Iterative methods for solving integral equations*, *Radio Science*, **26**, pp. 175–181.
- Lee, J. and Mal, A. K. (1995) *A volume integral equation technique for multiple scattering problems in elastodynamics*, *Journal of Applied Mathematics and Computation*, **67**, pp. 135–159.

- Leparoux, D., Bitri, A., and Grandjean, G. (2000) *Underground cavity detection: a new method based on seismic rayleigh waves*, European Journal of Environmental and Engineering Geophysics, **5**, pp. 33–53.
- Los, H. S., Herman, G. C., and Hölscher, P. (2001) *Dynamic interaction between train wheels and the subsurface*, Journal of sound and vibration, **247**, **5**, pp. 917–926.
- Muijres, A. J. H. and Herman, G. C. (2000) *Derivation of smooth apparent models for media with small-scale cracks (scalar theory)*, Geophys. J. Int., **140**, pp. 587–597.
- Muyzert, E. and Vermeer, P. (2004) *The impact of acquisition perturbations on land seismic data*, In: Exp. Abstr., 74th Ann. Internat. Mtg., Soc. of Expl. Geoph., Session: ACQ-35.
- Nolet, G. (1977) *The upper mantle under Western Europe inferred from the dispersion of rayleigh modes*, Journal of geophysics, **43**, pp. 265–286.
- Pacheco, P. S. (1997) *Parallel programming with MPI*, Morgan Kaufmann Publishers, Inc., California.
- Padovani, E., Priolo, E., and Seriani, G. (1994) *Low- and high-order finite element method: experience in seismic modeling*, J. Comp. Acoust., **12**, –, pp. 371–422.
- Pao, Y. H. and Varatharajulu, V. (1976) *Huygen's principle, radiation conditions, and integral formulas for the scattering of elastic waves*, J. Acoust. Soc. Am., **59**, **6**, pp. 1361–1371.
- Polak, E. (1971) *Computational Methods in Optimization*, Academic Press, New York.
- Regone, C. J. (1998) *Suppression of coherent noise in 3-D seismology*, The Leading Edge, **17**, pp. 1584–1589.
- Richmond, J. H. (1965) *Scattering by a dielectric cylinder of arbitrary cross-section shape*, IEEE Trans. on antennas and propagation, pp. 334–341.
- Rius, J. M., Ubeda, E., and Mosig, J. R. (1997) *Integral equation MEI applied to three-dimensional arbitrary surfaces*, Electronic Letters, **33**, **24**, pp. 2029–2030.
- Riyanti, C. D. and Herman, G. C. (2003) *3-D elastic scattering by near-surface heterogeneities*, In: Ext. Abstr., 65th Eur. Assn. Geophys. Eng.
- Rizk, N. J. (2003) *Parallelization of IBD computation for determining genetic disease map*, Second IEEE Int. workshop on High Performance computational Biology.
- Robertsson, J. O. A., Blanch, J. O., and Symes, W. W. (1994) *Viscoelastic finite-difference modeling*, Geophysics, **59**, –, pp. 1444–1456.

- Robertsson, J. O. A. and Holliger, K. (1997) *Modeling of seismic wave propagation near the earth's surface*, Physics of the Earth and Planetary Interiors, **104**, –, pp. 193–211.
- Séron, F. J., Sanz, F. J., Kindelan, M., and Badal, J. (1990) *Finite element method for elastic wave propagation*, Comm. Appl. Numerical Methods, **6**, –, pp. 359–368.
- Snieder, R. K. (1986) *3D linearized scattering of surface waves and a formalism for surface wave holography*, Geophys. J. R. Astron. Soc., **84**, pp. 581–605.
- (1987) *Surface wave holography*, in: *Seismic Tomography, with applications in global seismology and exploration geophysics* (G. Nolet, ed.), D. Reidel Pub. Co.
- Stokoe, K. I., Wright, G., Bay, J., and Roesset, J. (1994) *Characterization of geotechnical sites by SASW method*, in: *Geophysical Characterization of sites* (R. Woods, ed.), Oxford.
- Tan, T. H. (1975) *Far-field radiation characteristic of elastic waves and the elastodynamic radiation condition*, Appl. Sci. Res., **31**, pp. 363–375.
- Taner, M. T., Koehler, F., and Alhilali, K. A. (1974) *Estimation and correction of near-surface time anomalies*, Geophysics, **39**, pp. 441–463.
- Tarantola, A. (1984) *Linearized inversion of seismic reflection data*, Geophysical Prospecting, **32**, pp. 998–1015.
- Van den Berg, P. M. (2002) *Nonlinear scalar inverse scattering: algorithms and applications*, in: *Scattering and inverse scattering in pure and applied science, 142-161*, Academic Press, San Diego.
- van Wijk, K., Haney, M., and Scales, J. A. (2002) *Energy propagation in a 1D attenuative medium in the laboratory*, pre-print.
- Wagner, G. S. and Langston, C. H. (1992) *Body-to-surface-wave scattered energy in teleseismic coda observed at the NORESS seismic array*, Bull. of the Seismological Soc. of Am., **82**, pp. 2126–2138.
- Yilmaz, O. (1988) *Seismic data processing*, Soc. of Expl. Geophys.
- Zhdanov, M. S. (2002) *Geophysical inverse theory and regularization problems*, Elsevier Science B.V, Amsterdam.
- Zwamborn, A. P. M. and Van den Berg, P. M. (1997) *The three-dimensional weak form of the conjugate gradient FFT method for solving scattering problems*, IEEE Trans. Microwave Theory Tech., **40**, pp. 1757–1766.

Fourier Transforms

In this Appendix, we first define the Fourier transform with respect to the horizontal variables x_1 and x_2 . Let f be some complex-valued function of $\mathbf{x} = (x_1, x_2, x_3)$. Its spatial Fourier transform \tilde{f} as a function of the horizontal wavenumbers k_1 and k_2 , is defined by

$$\tilde{f}(k_1, k_2, x_3) = \frac{1}{4\pi^2} \int_{-\infty}^{\infty} dx_1 \int_{-\infty}^{\infty} dx_2 f(x_1, x_2, x_3) e^{-j[k_1x_1 + k_2x_2]}, \quad (\text{A.1})$$

with $x_3 \geq 0$; $k_1, k_2 \in \mathcal{R}$.

The inverse Fourier transform is given by

$$f(x_1, x_2, x_3) = \int_{-\infty}^{\infty} dk_1 \int_{-\infty}^{\infty} dk_2 \tilde{f}(k_1, k_2, x_3) e^{j[k_1x_1 + k_2x_2]}, \quad (\text{A.2})$$

with $x_3 \geq 0$; $x_1, x_2 \in \mathcal{R}$ and j is the imaginary unit.

We now introduce the horizontal slownesses p_1, p_2 such that

$$k_1 = \omega p_1, \quad k_2 = \omega p_2, \quad (\text{A.3})$$

and equation (A.2) can be expressed as

$$f(x_1, x_2, x_3) = \omega^2 \int_{-\infty}^{\infty} dp_1 \int_{-\infty}^{\infty} dp_2 \tilde{f}(p_1, p_2, x_3) e^{j\omega[p_1x_1 + p_2x_2]}. \quad (\text{A.4})$$

Note the double integration over p_1 and p_2 in equation (A.4). We can reduce this to one single integration using rotational symmetry. We transform from Cartesian components (p_1, p_2) to polar slowness (p, θ) through the relations

$$p_1 = p \cos \theta \quad \text{and} \quad p_2 = p \sin \theta, \quad (\text{A.5})$$

where $0 \leq \theta \leq 2\pi$ and $p = \sqrt{p_1^2 + p_2^2}$.

After this change of variables, the integration over θ in equation (A.4) can be performed analytically using Bessel functions. Consequently, the double integration in equation (A.4) is reduced to a single integration over p .

Let g be a real-valued function of t , $t \in \mathcal{R}$. The temporal Fourier transform is defined by:

$$\hat{g}(\omega) = \int_{t=-\infty}^{\infty} dt g(t) e^{j\omega t}, \quad (\text{A.6})$$

and the inverse transform can be written as

$$g(t) = \frac{1}{\pi} \mathbf{Re} \left\{ \int_{\omega=0}^{\infty} d\omega \hat{g}(\omega) e^{-j\omega t} \right\}. \quad (\text{A.7})$$

Derivation of the Green's Tensor for a Layered Medium

In this appendix, we derive a representation of the displacement vector $u_j(\mathbf{x}, \mathbf{x}^s)$ for a horizontally layered medium (see equations (2.28) and (2.29)) with a source at location \mathbf{x}^s . We use the representation of the wave field in terms of one slowness and one spatial coordinate, $\tilde{u}_j(p, z)$, to describe wave propagation in a stratified medium. Once we have a representation of the displacement in the slowness domain, $\tilde{u}_j(p, z)$, for an arbitrary point source, we can also obtain the Green's tensor $\tilde{u}_{ij}^G(p, z)$, which is the wave field generated by an impulsive point force. This Green's tensor u_{ij}^G is used in Chapter 2 in the domain-integral equation. In order to find an expression for $\tilde{u}_{ij}^G(p, z)$, we represent the displacement vector in the cylindrical coordinate system and derive two sets of decoupled first-order differential equations, which can be solved recursively (Kennett, 1983, 2001). The derivation here is partly taken from Kennett (2001) Chapter 2, 3, and 5. Since our derivation is somewhat different and concentrates on the Green's tensor, it is included here briefly.

For each layer we have the following set of equations:

$$\partial_i \tau_{ij}(\mathbf{x}, \mathbf{x}^s) + \omega^2 \rho^{(l)} u_j(\mathbf{x}, \mathbf{x}^s) = -f_j(\mathbf{x}, \mathbf{x}^s), \quad (\text{B.1})$$

$$\tau_{ij}(\mathbf{x}, \mathbf{x}^s) = \lambda^{(l)} \delta_{ij} \partial_k u_k(\mathbf{x}, \mathbf{x}^s) + \mu^{(l)} (\partial_i u_j(\mathbf{x}, \mathbf{x}^s) + \partial_j u_i(\mathbf{x}, \mathbf{x}^s)), \quad (\text{B.2})$$

where u_j is the displacement. The point force f_j can be expressed as $a_j \delta(\mathbf{x} - \mathbf{x}^s)$, where $\delta(\mathbf{x} - \mathbf{x}^s)$ denotes a three-dimensional unit pulse at position \mathbf{x}^s and a_j is an arbitrary constant vector. The displacement and the traction are both continuous across planes of discontinuity in the medium that do not contain the source.

At the surface \mathcal{S} , the following boundary condition holds:

$$n_i \tau_{ji}(\mathbf{x}, \mathbf{x}^s) = 0 \quad (\mathbf{x} \in \mathcal{S}), \quad (\text{B.3})$$

where n_i is the unit vector along the normal pointing away from the medium.

In order to solve these equations, we use the fact that both layers and interfaces in the medium under consideration are plane and horizontal. A simple form of these equations (B.1 and B.2) can be found by introducing new elements, which are related to the decoupling between compressional and vertical shear ($P - SV$) waves or to the horizontal shear (SH) waves.

In the cylindrical coordinates (Hudson, 1969), these elements read:

$$u_V = 1/r [\partial_r(r u_r) + \partial_\phi u_\phi], \quad (\text{B.4})$$

$$\tau_{Vz} = 1/r [\partial_r(r \tau_{rz}) + \partial_\phi \tau_{\phi z}], \quad (\text{B.5})$$

$$u_H = 1/r [\partial_r(r u_\phi) - \partial_\phi u_r], \quad (\text{B.6})$$

$$\tau_{Hz} = 1/r [\partial_r(r \tau_{\phi z}) + \partial_\phi \tau_{rz}], \quad (\text{B.7})$$

$$(\text{B.8})$$

and

$$f_V = 1/r [\partial_r(r f_r) + \partial_\phi f_\phi], \quad (\text{B.9})$$

$$f_H = 1/r [\partial_r(r f_\phi) - \partial_\phi f_r], \quad (\text{B.10})$$

$$(\text{B.11})$$

where V indicates the $P - SV$ part and H stands for the SH . The vertical components, u_z , τ_{zz} and f_z , remain unchanged.

In terms of these quantities, we can rearrange the equations in a form where we can isolate the z derivatives, leading to six coupled equations which separate into two sets.

The first set is:

$$\partial_z u_z = -\frac{\lambda^{(l)}}{\lambda^{(l)} + 2\mu^{(l)}} u_V + \frac{1}{\lambda^{(l)} + 2\mu^{(l)}} \tau_{zz}, \quad (\text{B.12})$$

$$\partial_z u_V = -\nabla_1^2 u_z + \frac{1}{\mu^{(l)}} \tau_{Vz}, \quad (\text{B.13})$$

$$\partial_z \tau_{zz} = -f_z - \rho^{(l)} \omega^2 u_z - \tau_{Vz}, \quad (\text{B.14})$$

$$\partial_z \tau_{Vz} = \rho^{(l)} [-\omega^2 - \nu^{(l)} \nabla_1^2] u_V - \frac{\lambda}{\lambda^{(l)} + 2\mu^{(l)}} \nabla_1^2 \tau_{zz} - f_V, \quad (\text{B.15})$$

where $\nabla_1^2 = r^{-1} \partial_r(r \partial_r) + r^{-2} \partial_{\phi\phi}$ and $\rho^{(l)} \nu^{(l)} = 4 \frac{\mu^{(l)}(\lambda^{(l)} + \mu^{(l)})}{\lambda^{(l)} + 2\mu^{(l)}}$.

These equations couple P waves with local wavespeed $\alpha^{(l)}$ to SV shear waves, involving displacement vertical displacement, with wavespeed $\beta^{(l)}$.

The second set comprises shear disturbances entirely confined to a horizontal plane (SH) with the same wavespeed $\beta^{(l)}$:

$$\partial_z u_H = -\frac{\tau_{Hz}}{\mu^{(l)}}, \quad (\text{B.16})$$

$$\partial_z \tau_{Hz} = -\rho^{(l)} \omega^2 u_H - \mu^{(l)} \nabla_1^2 u_H - f_H. \quad (\text{B.17})$$

Both sets are valid for the l -th layer, characterized by $z^{(l-1)} < z < z^{(l)}$.

By applying the slowness transform to the above equations with respect to the horizontal coordinates, we derive two decoupled sets of equations, one for $P - SV$ waves and another for SH waves. Both sets of equations have the form

$$\partial_z \mathbf{b} = \omega \mathbf{A}^{(l)} \mathbf{b} - \mathbf{s}, \quad (z^{(l-1)} < z < z^{(l)}), \quad (\text{B.18})$$

where the superscript l denotes the layer index.

For $P - SV$ waves, the equation reads

$$\frac{\partial}{\partial z} \begin{bmatrix} U \\ V \\ P \\ S \end{bmatrix} = \omega \begin{bmatrix} 0 & p(1 - 2\{\frac{\beta^{(l)}}{\alpha^{(l)}}\}^2) & (\rho^{(l)}\alpha^{(l)^2})^{-1} & 0 \\ -p & 0 & 0 & (\rho^{(l)}\beta^{(l)^2})^{-1} \\ -\rho^{(l)} & 0 & 0 & p \\ 0 & \rho^{(l)}(v^{(l)}p^2 - 1) & -p(1 - 2\frac{\beta^{(l)^2}}{\alpha^{(l)^2}}) & 0 \end{bmatrix} \begin{bmatrix} U \\ V \\ P \\ S \end{bmatrix} - \begin{bmatrix} 0 \\ 0 \\ F_z \\ F_V \end{bmatrix}, \quad (\text{B.19})$$

where $v = 4\beta^{(l)^2}(1 - \frac{\beta^{(l)^2}}{\alpha^{(l)^2}})$, and $\alpha^{(l)}$ and $\beta^{(l)}$ are the compressional and shear-wave speeds, respectively.

For SH waves, we have the following equation:

$$\frac{\partial}{\partial z} \begin{bmatrix} W \\ T \end{bmatrix} = \omega \begin{bmatrix} 0 & (\rho^{(l)}\beta^{(l)^2})^{-1} \\ \rho^{(l)}(\beta^{(l)^2}p^2 - 1) & 0 \end{bmatrix} \begin{bmatrix} W \\ T \end{bmatrix} - \begin{bmatrix} 0 \\ F_H \end{bmatrix}. \quad (\text{B.20})$$

In the above equations, U, V, W, P, S, T and F_z, F_V, F_H are scaled variables (Kennett, 1983, p. 27-29). They are given by

$$\begin{aligned} U &= \tilde{u}_z^G, & V &= -\tilde{u}_V^G/(\omega p), & P &= \tilde{\tau}_{zz}^G/\omega, \\ S &= \tilde{\tau}_{Vz}^G/(\omega^2 p), & F_z &= -\tilde{f}_z^G/\omega, & W &= -\tilde{u}_H^G/(\omega p), \\ T &= \tilde{\tau}_{Hz}^G/(\omega^2 p), & F_V &= -\tilde{f}_V^G/(\omega^2 p), & F_H &= -\tilde{f}_H^G/(\omega^2 p), \end{aligned} \quad (\text{B.21})$$

where $p = k/\omega$ with k is the horizontal wavenumber.

In equations (B.19) and (B.20), the compressional-wave speed, $\alpha^{(n)}$, is given by

$$\alpha^{(l)} = \sqrt{\frac{\lambda^{(l)} + 2\mu^{(l)}}{\rho^{(l)}}}, \quad (\text{B.22})$$

and for the shear-wave speed, we have

$$\beta^{(l)} = \sqrt{\frac{\mu^{(l)}}{\rho^{(l)}}}. \quad (\text{B.23})$$

In order to take dissipation of the media into account, we assume the wave speeds to be complex:

$$\text{Re}\{\alpha^{(l)}\} \geq 0 \quad \text{and} \quad \text{Im}\{\alpha^{(l)}\} \geq 0, \quad (\text{B.24})$$

and similarly for $\beta^{(l)}$.

From equations (B.19) and (B.20), we derive the Green's tensor.

B.1 Solution of the Differential Equation

In this subsection, the boundary value problem, equations (B.18)-(B.21), together with the traction-free boundary condition of the surface, is solved by decomposing the wave field into up- and down-going waves. We use the scattering matrix method (Kennett, 1983) where the scattering matrix is constructed recursively and contains the transmission and reflection properties of each interface. We first calculate the scattering matrices of the region above and below the source. To do so, we decompose the wave field into up-going and down-going waves to obtain a relation between the waves above and below the source.

Multiplying equation (B.18) by the inverse eigenvector matrix of $\mathbf{A}^{(l)}$ yields:

$$\partial_z \mathbf{v} = j\omega \Lambda^{(l)} \mathbf{v}. \quad (\text{B.25})$$

Here $\mathbf{v} = \mathbf{D}^{(l)-1} \mathbf{b}$ with $\mathbf{D}^{(l)-1}$ the inverse eigenvector matrix of $\mathbf{A}^{(l)}$, and $\Lambda^{(l)}$ is a diagonal matrix consisting of the eigenvalues of $\mathbf{A}^{(l)}$. The matrix $\mathbf{D}^{(l)-1}$ is given by Kennett (1983) p. 48-51. The vector \mathbf{v} consists of up-going and down-going waves.

The solution of equation (B.25) can be written as:

$$\mathbf{v}(z) = \mathbf{Q}^{(l)}(z, z^s) \mathbf{v}(z^s), \quad \text{with } z^{(l-1)} < z^s, z < z^{(l)}, \quad (\text{B.26})$$

where $\mathbf{Q}^{(l)}(z, z^s)$ is the propagator matrix, which depends on the difference between the depths z and z^s .

For $P - SV$ waves, $\mathbf{Q}^{(l)}(z, z^s)$ is given by

$$\mathbf{Q}^{(l)}(z, z^s) = \text{diag}(e^{-j\omega q_{\alpha,l}(z-z^s)}, e^{-j\omega q_{\beta,l}(z-z^s)}, e^{j\omega q_{\alpha,l}(z-z^s)}, e^{j\omega q_{\beta,l}(z-z^s)}), \quad (\text{B.27})$$

and for SH waves

$$\mathbf{Q}^{(l)}(z, z^s) = \text{diag}(e^{-j\omega q_{\beta,l}(z-z^s)}, e^{j\omega q_{\beta,l}(z-z^s)}), \quad (\text{B.28})$$

with $z^{(l-1)} < z^s, z < z^{(l)}$, $q_{\alpha,l}(z, z^s) = \sqrt{\frac{1}{\alpha^{(l)2}} - p^2}$ and $q_{\beta,l}(z, z^s) = \sqrt{\frac{1}{\beta^{(l)2}} - p^2}$ are the vertical slowness for the l th layer. According to the way we have introduced the Fourier transform, both real and imaginary parts of these complex slownesses are positive: $\text{Re}(q_{\alpha,l}) \geq 0$ and $\text{Im}(q_{\alpha,l}) \geq 0$, and similarly for $q_{\beta,l}$.

Finally, after computing the wave field at the source level (see Ditzel et al., 2001, Appendix A.3-A.6, for details), the wave field at the receiver is evaluated by propagating the field from the source to receiver level. The wave field at the receiver level in terms of U , V , and W is then obtained by multiplying the wave field vector \mathbf{v} with the eigenvector matrix $\mathbf{D}^{(l)}$.

The component of the Green's displacement tensor for the embedding medium in the cylindrical coordinates is expressed in the following form:

$$u_z^G(r, \phi, z; \omega; z^s) = \omega^2 \int_0^\infty dp p \tilde{u}_z^G(p; z; \omega; z^s), \quad (\text{B.29})$$

$$u_r^G(r, \phi, z; \omega; z^s) = \omega^2 \int_0^\infty dp p \tilde{u}_r^G(p; z; \omega; z^s), \quad (\text{B.30})$$

$$u_\phi^G(r, \phi, z; \omega; z^s) = \omega^2 \int_0^\infty dp p \tilde{u}_\phi^G(p; z; \omega; z^s), \quad (\text{B.31})$$

where $\tilde{u}_r^G(p; z; \omega; z^s)$, $\tilde{u}_\phi^G(p; z; \omega; z^s)$, $\tilde{u}_z^G(p; z; \omega; z^s)$ are given by Kennett (1983; p. 34-35, equations (2.44)-(2.46)).

The above expressions are the solution of the system of equations (B.19) and (B.20) in the cylindrical coordinate system.

Since the representation of the displacement \tilde{u}_j^G for arbitrary point force $f_j(\mathbf{x}, \mathbf{x}^s)$ can be obtained, we can also find the Green's tensor \tilde{u}_{jk}^G , which is generated by an impulse force tensor. The wave field \tilde{u}_j^G and the Green's tensor \tilde{u}_{jk}^G are related in the following way

$$\tilde{u}_j^G(p; z; \omega; z^s) = \tilde{u}_{jk}^G(p; z; \omega; z^s) a_k, \quad (\text{B.32})$$

with a_k the strength of the k -component of the exerted force, f_k .

In this way, we have obtained expressions for all nine components of the Green's tensor \tilde{u}_{jk}^G . By means of the inverse slowness transform with respect to the slowness p , we can also find expressions for the Green's tensor in cylindrical coordinates:

$$u_{zk}^G(r, \phi, z; \omega; z^s) = \omega^2 \int_0^\infty dp p \tilde{u}_{zk}^G(p; z; \omega; z^s), \quad (\text{B.33})$$

$$u_{rk}^G(r, \phi, z; \omega; z^s) = \omega^2 \int_0^\infty dp p \tilde{u}_{rk}^G(p; z; \omega; z^s), \quad (\text{B.34})$$

$$u_{\phi k}^G(r, \phi, z; \omega; z^s) = \omega^2 \int_0^\infty dp p \tilde{u}_{\phi k}^G(p; z; \omega; z^s), \quad (\text{B.35})$$

where

$$\tilde{u}_{z3}^G(p; z; \omega; z^s) = U_3(p, z, z^s) J_0(\omega pr), \quad (\text{B.36})$$

$$\tilde{u}_{z1}^G(p; z; \omega; z^s) = -U_1(p, z, z^s) J_1(\omega pr) \cos \phi, \quad (\text{B.37})$$

$$\tilde{u}_{z2}^G(p; z; \omega; z^s) = -U_2(p, z, z^s) J_1(\omega pr) \sin \phi, \quad (\text{B.38})$$

$$\tilde{u}_{r1}^G(p; z; \omega; z^s) = \left[V_1(p, z, z^s) \frac{\partial J_1(\omega pr)}{\partial(\omega pr)} + W_1(p, z, z^s) \frac{J_1(\omega pr)}{\omega pr} \right] \cos \phi, \quad (\text{B.39})$$

$$\tilde{u}_{r2}^G(p, z; \omega; z^s) = \left[V_2(p, z, z^s) \frac{\partial J_1(\omega pr)}{\partial(\omega pr)} + W_2(p, z, z^s) \frac{J_1(\omega pr)}{\omega pr} \right] \sin \phi, \quad (\text{B.40})$$

$$\tilde{u}_{r3}^G(p, z; \omega; z^s) = -V_3(p, z, z^s) J_1(\omega pr), \quad (\text{B.41})$$

$$\tilde{u}_{\phi1}^G(p, z; \omega; z^s) = -\left[V_1(p, z, z^s) \frac{J_1(\omega pr)}{\omega pr} - W_1(p, z, z^s) \frac{\partial J_1(\omega pr)}{\partial(\omega pr)} \right] \sin \phi, \quad (\text{B.42})$$

$$\tilde{u}_{\phi2}^G(p, z; \omega; z^s) = \left[V_2(p, z, z^s) \frac{J_1(\omega pr)}{\omega pr} - W_2(p, z, z^s) \frac{\partial J_1(\omega pr)}{\partial(\omega pr)} \right] \cos \phi, \quad (\text{B.43})$$

$$\tilde{u}_{\phi3}^G(p, z; \omega; z^s) = 0, \quad (\text{B.44})$$

where r denotes the distance between the receiver and source positions, ϕ denotes the angle between the receiver and source positions in the horizontal plane; z and z^s are the vertical coordinates of the receiver and source points, respectively. In the above equations, subscripts 1, 2 and 3 correspond to the solution due to the point sources with vector components $(f_1, 0, 0)$, $(0, f_2, 0)$ and $(0, 0, f_3)$ in the Cartesian coordinate system, respectively. J_0 and J_1 are Bessel functions of orders 0 and 1, respectively (Abramowitz and Stegun, 1968).

The Green's tensor in the cylindrical coordinate system, given in equations (B.36)-(B.44), can be transformed to Cartesian coordinates as follows:

$$\tilde{u}_{1k}^G(p; z; \omega; z^s) = \tilde{u}_{rk}^G(p; z; \omega; z^s) \cos \phi - \tilde{u}_{\phi k}^G(p; z; \omega; z^s) \sin \phi, \quad (\text{B.45})$$

$$\tilde{u}_{2k}^G(p; z; \omega; z^s) = \tilde{u}_{rk}^G(p; z; \omega; z^s) \sin \phi + \tilde{u}_{\phi k}^G(p; z; \omega; z^s) \cos \phi, \quad (\text{B.46})$$

$$\tilde{u}_{3k}^G(p; z; \omega; z^s) = \tilde{u}_{zk}^G(p; z; \omega; z^s). \quad (\text{B.47})$$

Hence, the inverse slowness transform of equations (B.45)-(B.47), which are required in the computation of the matrix elements $\mathbf{G}_{ik}^{m,n}$, can be written as

$$u_{jk}^G(\mathbf{x}; \omega; \mathbf{x}') = \omega^2 \int_0^\infty dp p \tilde{u}_{jk}^G(p; z; \omega; z^s), \quad (\text{B.48})$$

with $j, k = 1, 2, 3$. This result is used in equation (2.67).

The Expression of the Free-Space Green's Tensor in the Spatial and the Slowness Domain

In equation (2.67), we need the expression of the free-space Green's tensor in the spatial and the slowness domain.

The free-space Green's tensor in the spatial domain is given by (Harris, 2001):

$$g_{ik}(\mathbf{x}^{(m)}; \omega; \mathbf{x}') = \frac{1}{\mu} \delta_{ik} G_\beta + \frac{1}{\rho \omega^2} \partial_i \partial_k (G_\beta - G_\alpha), \quad (\text{C.1})$$

with

$$G_\beta = \frac{1}{4\pi |\mathbf{x}^{(m)} - \mathbf{x}'|} e^{j \frac{\omega}{\beta} |\mathbf{x}^{(m)} - \mathbf{x}'|}, \quad (\text{C.2})$$

and

$$G_\alpha = \frac{1}{4\pi |\mathbf{x}^{(m)} - \mathbf{x}'|} e^{j \frac{\omega}{\alpha} |\mathbf{x}^{(m)} - \mathbf{x}'|}, \quad (\text{C.3})$$

where α and β denote the compressional- and the shear-wave speeds, respectively.

In order to obtain the analytical expression of the Green's tensor in the slowness domain, we transform equation (C.1)-(C.3) to the (p, z^m) domain. Using the elementary concepts of slowness transform with respect to derivation and the properties of the Bessel function, we obtain the elements of the free-space Green's tensor in the slowness domain as follows:

$$\begin{aligned} \tilde{g}_{11}(p; z^{(m)}; \omega; z') &= \frac{1}{\omega \rho} \left[\frac{1}{\beta^2} G_\beta J_0(\omega p r) + \frac{p^2}{2} (G_\alpha - G_\beta) (J_0(\omega p r) \right. \\ &\quad \left. - J_2(\omega p r) \cos 2\phi) \right], \end{aligned} \quad (\text{C.4})$$

$$\tilde{g}_{12}(p; z^{(m)}; \omega; z') = -\frac{p^2}{\omega \rho} \sin \phi \cos \phi [G_\alpha - G_\beta] J_2(\omega p r), \quad (\text{C.5})$$

$$\tilde{g}_{13}(p; z^{(m)}; \omega; z') = \frac{p}{\omega^2 \rho} \cos \phi [\partial_z G_\alpha - \partial_z G_\beta] J_1(\omega p r), \quad (\text{C.6})$$

$$\tilde{g}_{23}(p; z^{(m)}; \omega; z') = \frac{p}{\omega^2 \rho} \sin \phi [\partial_z G_\alpha - \partial_z G_\beta] J_1(\omega p r), \quad (\text{C.7})$$

$$\begin{aligned} \tilde{g}_{22}(p; z^{(m)}; \omega; z') &= \frac{1}{\omega \rho} \left[\frac{1}{\beta^2} G_\beta J_0(\omega p r) + \frac{p^2}{2} (G_\alpha - G_\beta) [J_0(\omega p r) \right. \\ &\quad \left. + J_2(\omega p r) \cos 2\phi \right], \end{aligned} \quad (\text{C.8})$$

$$\tilde{g}_{33}(p; z^{(m)}; \omega; z') = \frac{1}{\omega \rho} \left[\frac{1}{\beta^2} G_\beta J_0(\omega p r) - \frac{1}{\omega^2} (\partial_z^2 G_\alpha - \partial_z^2 G_\beta) J_0(\omega p r) \right], \quad (\text{C.9})$$

with

$$G_\alpha = \frac{j\omega}{4\pi q_\alpha} e^{j\omega q_\alpha |z^{(m)} - z'|}, \quad \text{and} \quad G_\beta = \frac{j\omega}{4\pi q_\beta} e^{j\omega q_\beta |z^{(m)} - z'|}, \quad (\text{C.10})$$

where $z^{(m)} \in \mathcal{D}_m$, $z' \in \mathcal{D}_n$, $q_\alpha = \sqrt{\frac{1}{\alpha^2} - p^2}$ and $q_\beta = \sqrt{\frac{1}{\beta^2} - p^2}$. Here, α and β denote the compressional- and the shear-wave speeds, respectively.

According to the way we have introduced the Fourier and slowness transform, both real and imaginary parts of these complex slownesses are positive : $\mathbf{Re}(q_\alpha) \geq 0$ and $\mathbf{Im}(q_\alpha) \geq 0$, and similarly for q_β .

Calculation of the Green Matrix

In this appendix, we show in detail how to calculate the elements of the Green matrix $\mathbf{G}_{ik}^{(m,n)}$, given by equation (2.67). For convenience, we rewrite equation (2.67) in the form

$$\mathbf{G}_{ik}^{(m,n)} = \mathbf{I}_{ik}^{(m,n)} - \mathbf{A}_{ik}^{(m,n)} + \mathbf{B}_{ik}^{(m,n)}, \quad (\text{D.1})$$

where

$$\mathbf{I}_{ik}^{(m,n)} = \delta_{ik} \delta_{mn}, \quad (\text{D.2})$$

$$\mathbf{A}_{ik}^{(m,n)} = \omega^2 \Delta \rho_n \int_{\mathbf{x}' \in \mathcal{D}_n} \int_0^\infty p \quad (\text{D.3})$$

$$\left[\tilde{u}_{ik}^G(p; z^{(m)}; \omega; z') - \tilde{g}_{ik}(p; z^{(m)}; \omega; z') \right] dp dx' dy' dz', \quad (\text{D.4})$$

and

$$\mathbf{B}_{ik}^{(m,n)} = \omega^2 \Delta \rho_n \int_{\mathcal{D}_n} g_{ik}(\mathbf{x}^m; \omega; \mathbf{x}') dx' dy' dz'. \quad (\text{D.5})$$

where δ_{ik} and δ_{mn} denote the Kronecker delta.

D.1 Evaluation of the Elements of $\mathbf{B}_{ik}^{(m,n)}$

We first consider the last term on the right hand side of equation (D.1), given by equation (D.5). It reads

$$\mathbf{B}_{ik}^{(m,n)} = \omega^2 \Delta \rho_n \int_{\mathcal{D}_n} g_{ik}(\mathbf{x}^{(m)}; \omega; \mathbf{x}') dx' dy' dz', \quad (\text{D.6})$$

where $g_{ik}(\mathbf{x}^m; \omega; \mathbf{x}')$ is given by equations (C.1)-(C.3).

We follow the computational approach by Richmond (1965) and Ditzel (2003) for evaluating the integral of the two-dimensional free-space Green's function by approximating the rectangular cells by a circular one with an equivalent radius that gives the same area as the

rectangular cells. The closed-form solution of the domain integration of the free-space Green's function can be then found analytically.

Zwamborn and Van den Berg (1997) use a similar approach for solving the problem of electromagnetic scattering by an inhomogeneous three-dimensional dielectric object, in order to calculate the integral of the three-dimensional free-space Green's function analytically.

To this end, we substitute the square block by a sphere which occupies a volume of the same size. The analytical solution of the above integral for the elastic Green's tensor can be obtained for each element of the $\mathbf{B}_{ik}^{(m,n)}$. It reads

$$\mathbf{B}_{ik}^{(m,n)} = \omega^2 \Delta \rho_n \left[\frac{1}{\mu} \delta_{ik} G_\beta^I + \frac{1}{\rho \omega^2} (\partial_i \partial_k G_\beta^I - \partial_i \partial_k G_\alpha^I) \right], \quad (\text{D.7})$$

where for $m \neq n$, one obtains

$$G_\beta^I = \frac{\exp(jk_\beta |\mathbf{x}^m|)}{jk_\beta^3 |\mathbf{x}^{(m)}|} \left[\sinh(jk_\beta \delta) - jk_\beta \delta \cosh(jk_\beta \delta) \right], \quad (\text{D.8})$$

$$\partial_i \partial_k G_\beta^I = \left[\sinh(jk_\beta \delta) - jk_\beta \delta \cosh(jk_\beta \delta) \right] \partial_i \partial_k \frac{\exp(jk_\beta |\mathbf{x}^{(m)}|)}{jk_\beta^3 |\mathbf{x}^{(m)}|}, \quad (\text{D.9})$$

and

$$\partial_i \partial_k G_\alpha^I = \left[\sinh(jk_\alpha \delta) - jk_\alpha \delta \cosh(jk_\alpha \delta) \right] \partial_i \partial_k \frac{\exp(jk_\alpha |\mathbf{x}^{(m)}|)}{jk_\alpha^3 |\mathbf{x}^{(m)}|}. \quad (\text{D.10})$$

For $m = n$, we have

$$G_\beta^I = \frac{(1 - jk_\beta \delta) \exp(jk_\beta \delta) - 1}{k_\beta^2}, \quad (\text{D.11})$$

$$\begin{aligned} \partial_i \partial_k (G_\beta^I - G_\alpha^I) &= \delta_{ik} \frac{4\pi}{3} \left\{ j\delta (k_\beta - k_\alpha) + \exp(jk_\beta \delta) \left(\frac{jk_\beta \delta}{2} - \frac{3}{2} \right) \right. \\ &\quad \left. - \exp(jk_\alpha \delta) \left(\frac{jk_\alpha \delta}{2} - \frac{3}{2} \right) \right\}, \end{aligned} \quad (\text{D.12})$$

where $k_\beta = \frac{\omega}{\beta}$, $k_\alpha = \frac{\omega}{\alpha}$, $\delta = \Delta \left(\frac{3}{4\pi} \right)^{1/3}$ with $\Delta = \Delta x = \Delta y = \Delta z$.

D.2 Evaluation of the Elements of $\mathbf{A}_{ik}^{(m,n)}$

Next, we consider the second term on the right hand side of equation (D.1), given by equation (D.3). We can interchange the order of integration for the spatial (\mathbf{x}') and p -integrations. The expression of equation (D.3) then becomes

$$\begin{aligned} \mathbf{A}_{ik}^{(m,n)} &= \omega^2 \Delta \rho_n \int_0^\infty p \int_{\mathbf{x}' \in \mathcal{D}_n} \left[\tilde{u}_{ik}^G(p; z^{(m)}; \omega; z') \right. \\ &\quad \left. - \tilde{g}_{ik}(p; z^{(m)}; \omega; z') \right] dx' dy' dz' dp, \end{aligned} \quad (\text{D.13})$$

where $\tilde{u}_{ik}^G(p; z^{(m)}; \omega; z')$ and $\tilde{g}_{ik}(p; z^{(m)}; \omega; z')$ are found in Appendix B and Appendix C, respectively.

In the next subsection, we first calculate the integration over the z -direction that can be done analytically.

D.2.1 The Integration of the Green Matrix over the z -Direction.

In this subsection, we evaluate the integration of the Green matrix equation(D.13) over the z -direction. We can rewrite equation (D.13) as follows:

$$\begin{aligned} \mathbf{A}_{ik}^{(m,n)} &= \omega^2 \Delta \rho_n \int_0^\infty \int_{\mathcal{D}_H} \int_{z^{(n)-}}^{z^{(n)+}} [\tilde{u}_{ik}^G(p; z^{(m)}; \omega; z') \\ &\quad - \tilde{g}_{ik}(p; z^{(m)}; \omega; z')] p dz' dx' dy' dp, \end{aligned} \quad (\text{D.14})$$

with

$$\begin{aligned} \mathcal{D}_H &= \left\{ (x, y) \in \mathcal{R}^2 \mid x^{(n)} - \frac{\Delta x}{2} < x < x^{(n)} + \frac{\Delta x}{2}, \right. \\ &\quad \left. y^{(n)} - \frac{\Delta y}{2} < y < y^{(n)} + \frac{\Delta y}{2} \right\}, \end{aligned} \quad (\text{D.15})$$

and

$$z^{(n)+} = z^{(n)} + \frac{\Delta z}{2}, z^{(n)-} = z^{(n)} - \frac{\Delta z}{2}. \quad (\text{D.16})$$

The expression of $\tilde{u}_{ik}^G(p; z^{(m)}; \omega; z')$ is composed of the propagator matrix and the wave field at the source position. The propagator matrix only depends on the depth of the source, z' , and receiver, $z^{(m)}$.

The free-space Green's tensor $\tilde{g}_{ik}^G(p; z^{(m)}; \omega; z')$ as shown in Appendix C is expressed independently as the exponential function of z' and $z^{(m)}$ and a function containing only the horizontal variables.

It is straightforward (but tedious) then to evaluate the integral over the z -direction, yielding the following expression:

$$\begin{aligned} \mathbf{A}_{ik}^{(m,n)} &= \omega^2 \Delta \rho_n \int_0^\infty \int_{\mathbf{x}'_H \in \mathcal{D}_H} [\mathcal{U}_{ik}^G(p; z^{(m)}; \omega; z^{(n)}) \\ &\quad - \mathcal{G}_{ik}(p; z^{(m)}; \omega; z^{(n)})] p dx' dy' dp. \end{aligned} \quad (\text{D.17})$$

The \mathcal{U}_{ik}^G functions are given by:

$$\begin{aligned} \mathcal{U}_{11}^G(p; z^{(m)}; \omega; z^{(n)}) &= A_\alpha V_1(p, z^{(m)}, z^{(n)}) \\ &\times \left\{ \frac{\partial J_1(\omega pr)}{\partial(\omega pr)} \cos^2 \phi + \frac{J_1(\omega pr)}{\omega pr} \sin^2 \phi \right\} \\ &+ A_\beta W_1(p, z^{(m)}, z^{(n)}) \\ &\times \left\{ \frac{J_1(\omega pr)}{\omega pr} \cos^2 \phi - \frac{\partial J_1(\omega pr)}{\partial(\omega pr)} \sin^2 \phi \right\}, \end{aligned} \quad (\text{D.18})$$

$$\begin{aligned} \mathcal{U}_{12}^G(p; z^{(m)}; \omega; z^{(n)}) &= A_\alpha V_2(p, z^{(m)}, z^{(n)}) \sin \phi \cos \phi \left\{ \frac{\partial J_1(\omega pr)}{\partial(\omega pr)} - \frac{J_1(\omega pr)}{\omega pr} \right\} \\ &+ A_\beta W_2(p, z^{(m)}, z^{(n)}) \sin \phi \cos \phi \left\{ \frac{J_1(\omega pr)}{\omega pr} \right. \\ &\left. + \frac{\partial J_1(\omega pr)}{\partial(\omega pr)} \right\}, \end{aligned} \quad (\text{D.19})$$

$$\mathcal{U}_{13}^G(p; z^{(m)}; \omega; z^{(n)}) = -A_\alpha V_3(p, z^{(m)}, z^{(n)}) J_1(\omega pr) \cos \phi \quad (\text{D.20})$$

$$\begin{aligned} \mathcal{U}_{21}^G(p; z^{(m)}; \omega; z^{(n)}) &= A_\alpha V_1(p, z^{(m)}, z^{(n)}) \sin \phi \cos \phi \left\{ \frac{\partial J_1(\omega pr)}{\partial(\omega pr)} - \frac{J_1(\omega pr)}{\omega pr} \right\} \\ &+ A_\beta W_1(p, z^{(m)}, z^{(n)}) \sin \phi \cos \phi \left\{ \frac{J_1(\omega pr)}{\omega pr} \right. \\ &\left. + \frac{\partial J_1(\omega pr)}{\partial(\omega pr)} \right\}, \end{aligned} \quad (\text{D.21})$$

$$\begin{aligned} \mathcal{U}_{22}^G(p; z^{(m)}; \omega; z^{(n)}) &= A_\alpha V_2(p, z^{(m)}, z^{(n)}) \left\{ \frac{\partial J_1(\omega pr)}{\partial(\omega pr)} \sin^2 \phi + \frac{J_1(\omega pr)}{\omega pr} \cos^2 \phi \right\} \\ &+ A_\beta W_2(p, z^{(m)}, z^{(n)}) \left\{ \frac{J_1(\omega pr)}{\omega pr} \sin^2 \phi \right. \\ &\left. - \frac{\partial J_1(\omega pr)}{\partial(\omega pr)} \cos^2 \phi \right\}, \end{aligned} \quad (\text{D.22})$$

$$\mathcal{U}_{3k}^G(p; z^{(m)}; \omega; z^{(n)}) = A_\alpha \tilde{u}_{3k}^G(p, z^{(m)}, z^{(n)}), \quad (\text{D.23})$$

with $k = 1, 2, 3$ and

$$A_\alpha = \frac{\sin(\omega q_\alpha \Delta_z / 2)}{\omega q_\alpha / 2}, \quad A_\beta = \frac{\sin(\omega q_\beta \Delta_z / 2)}{\omega q_\beta / 2}. \quad (\text{D.24})$$

For $z^{(m)} \neq z^{(n)}$, the \mathcal{G}_{ik} functions are given by:

$$\begin{aligned} \mathcal{G}_{11}(p; z^{(m)}; \omega; z^{(n)}) &= \frac{1}{\omega \rho} \left(\frac{1}{\beta^2} \mathcal{G}_\beta J_0(\omega pr) \right. \\ &\left. + \frac{\rho^2}{2} (\mathcal{G}_\alpha - \mathcal{G}_\beta) (J_0(\omega pr) - J_2(\omega pr) \cos 2\phi) \right), \end{aligned} \quad (\text{D.25})$$

$$\mathcal{G}_{12}(p; z^{(m)}; \omega; z^{(n)}) = -\frac{p^2}{\omega\rho} \sin\phi \cos\phi (\mathcal{G}_\alpha - \mathcal{G}_\beta) J_2(\omega pr), \quad (\text{D.26})$$

$$\mathcal{G}_{13}(p; z^{(m)}; \omega; z^{(n)}) = \text{sign}(z^{(n)}, z^{(m)}) \frac{j p}{\omega\rho} \cos\phi (q_\beta \mathcal{G}_\beta - q_\alpha \mathcal{G}_\alpha) J_1(\omega pr), \quad (\text{D.27})$$

$$\begin{aligned} \mathcal{G}_{22}(p; z^{(m)}; \omega; z^{(n)}) &= \frac{1}{\omega\rho} \left(\frac{1}{\beta^2} \mathcal{G}_\beta J_0(\omega pr) \right. \\ &\quad \left. + \frac{p^2}{2} (\mathcal{G}_\alpha - \mathcal{G}_\beta) (J_0(\omega pr) + J_2(\omega pr) \cos 2\phi) \right), \end{aligned} \quad (\text{D.28})$$

$$\mathcal{G}_{23}(p; z^{(m)}; \omega; z^{(n)}) = \text{sign}(z^{(n)}, z^{(m)}) \frac{j p}{\omega\rho} \sin\phi (q_\beta \mathcal{G}_\beta - q_\alpha \mathcal{G}_\alpha) J_1(\omega pr), \quad (\text{D.29})$$

$$\mathcal{G}_{33}(p; z^{(m)}; \omega; z^{(n)}) = \frac{1}{\omega\rho} \left(\frac{1}{\beta^2} \mathcal{G}_\beta J_0(\omega pr) + (q_\alpha^2 \mathcal{G}_\alpha - q_\beta^2 \mathcal{G}_\beta) J_0(\omega pr) \right), \quad (\text{D.30})$$

with

$$\mathcal{G}_\alpha = A_\alpha \frac{j\omega}{4\pi q_\alpha} e^{j\omega q_\alpha |z^{(n)} - z^{(m)}|}, \quad \mathcal{G}_\beta = A_\beta \frac{j\omega}{4\pi q_\beta} e^{j\omega q_\beta |z^{(n)} - z^{(m)}|}, \quad (\text{D.31})$$

In equations (D.27)-(D.29), *sign* represents the *sign*-function, defined as

$$\text{sign}(z^{(n)}, z^{(m)}) = \begin{cases} -1 & z^{(n)} < z^{(m)}, \\ 1 & z^{(n)} > z^{(m)}. \end{cases} \quad (\text{D.32})$$

For $z^{(m)} = z^{(n)}$, we have the following expression for $\mathcal{G}_{ik}(p; z^{(m)}; \omega; z^{(m)})$:

$$\begin{aligned} \mathcal{G}_{11}(p; z^{(m)}; \omega; z^{(m)}) &= \frac{1}{\omega\rho} \left(\frac{1}{\beta^2} \mathcal{C}_\beta J_0(\omega pr) + \frac{p^2}{2} (\mathcal{C}_\alpha - \mathcal{C}_\beta) (J_0(\omega pr) \right. \\ &\quad \left. - J_2(\omega pr) \cos 2\phi) \right), \end{aligned} \quad (\text{D.33})$$

$$\mathcal{G}_{12}(p; z^{(m)}; \omega; z^{(m)}) = -\frac{p^2}{\omega\rho} \sin\phi \cos\phi (\mathcal{C}_\alpha - \mathcal{C}_\beta) J_2(\omega pr), \quad (\text{D.34})$$

$$\mathcal{G}_{13}(p; z^{(m)}; \omega; z^{(m)}) = \frac{j p}{\omega\rho} \cos\phi (q_\beta \mathcal{C}_\beta - q_\alpha \mathcal{C}_\alpha) J_1(\omega pr), \quad (\text{D.35})$$

$$\begin{aligned} \mathcal{G}_{22}(p; z^{(m)}; \omega; z^{(m)}) &= \frac{1}{\omega\rho} \left(\frac{1}{\beta^2} \mathcal{C}_\beta J_0(\omega pr) + \frac{p^2}{2} (\mathcal{C}_\alpha - \mathcal{C}_\beta) (J_0(\omega pr) \right. \\ &\quad \left. + J_2(\omega pr) \cos 2\phi) \right), \end{aligned} \quad (\text{D.36})$$

$$\mathcal{G}_{23}(p; z^{(m)}; \omega; z^{(n)}) = \frac{jp}{\omega\rho} \sin \phi(q_\beta \mathcal{C}_\beta - q_\alpha \mathcal{C}_\alpha) J_1(\omega pr), \quad (\text{D.37})$$

$$\mathcal{G}_{33}(p; z^{(m)}; \omega; z^{(n)}) = \frac{1}{\omega\rho} \left(\frac{1}{\beta^2} \mathcal{C}_\beta J_0(\omega pr) + (q_\alpha^2 \mathcal{C}_\alpha - q_\beta^2 \mathcal{C}_\beta) J_0(\omega pr) \right), \quad (\text{D.38})$$

where

$$\mathcal{C}_\alpha = \frac{1}{2\pi q_\alpha^2} (e^{j\omega q_\alpha \frac{\Delta z}{2}} - 1) \quad \text{and} \quad \mathcal{C}_\beta = \frac{1}{2\pi q_\beta^2} (e^{j\omega q_\beta \frac{\Delta z}{2}} - 1). \quad (\text{D.39})$$

Thus, we arrive at

$$\begin{aligned} \mathbf{A}_{ik}^{(m,n)} &= \omega^2 \Delta \rho_n \\ &\times \int_0^\infty \int_{x_n^-}^{x_n^+} \int_{y_n^-}^{y_n^+} \left[\mathcal{U}_{ik}^G(p; z^{(m)}; \omega; z^{(n)}) - \mathcal{G}_{ik}(p; z^{(m)}; \omega; z^{(n)}) \right] p dx' dy' dp, \end{aligned} \quad (\text{D.40})$$

where $\mathcal{U}_{ik}^G(p; z^{(m)}; \omega; z^{(n)})$ and $\mathcal{G}_{ik}(p; z^{(m)}; \omega; z^{(n)})$ are given by equations (D.18)-(D.39), and

$$x_n^- = x^{(n)} - \frac{\Delta x}{2}, \quad x_n^+ = x^{(n)} + \frac{\Delta x}{2}, \quad (\text{D.41})$$

$$y_n^- = y^{(n)} - \frac{\Delta y}{2}, \quad y_n^+ = y^{(n)} + \frac{\Delta y}{2}. \quad (\text{D.42})$$

In Section 2.5, we discussed the acceleration of the convergence of the numerical calculation of the Green's tensor. We observed that for small distance between the observation and source point, the free-space Green's tensor approaches the actual Green tensor well for large p -values.

Let p_{max} be the maximum value for non-vanishing values of the difference between the free-space and the actual Green tensor. Consequently, we can rewrite the expression of (D.40) as:

$$\begin{aligned} \mathbf{A}_{ik}^{(m,n)} &= \omega^2 \Delta \rho_n \\ &\times \int_0^{p_{max}} \int_{x_n^-}^{x_n^+} \int_{y_n^-}^{y_n^+} \left[\mathcal{U}_{ik}^G(p; z^{(m)}; \omega; z^{(n)}) - \mathcal{G}_{ik}(p; z^{(m)}; \omega; z^{(n)}) \right] p dx' dy' dp. \end{aligned} \quad (\text{D.43})$$

The above integral cannot be performed analytically, but has to be evaluated numerically. To evaluate the above integral, we distinguish between diagonal and non-diagonal elements.

D.2.2 Evaluation of the Non-Diagonal Elements of $\mathbf{A}_{ik}^{(m,n)}$

In order to calculate the non-diagonal elements of $\mathbf{A}_{ik}^{(m,n)}$ ($m \neq n$), we apply the midpoint rule. The interval $[0, p_{max}]$ in the p -domain is divided by P subintervals with width of Δ_p . We then

obtain the following expression:

$$\mathbf{A}_{ik}^{(m,n)} = \omega^2 \Delta \rho_n \Delta_x \Delta_y \Delta_p \sum_{l=1}^P p_l \left[\mathcal{U}_{ik}^G(p_l; z^{(m)}; \omega; z^{(n)}) - \mathcal{G}_{ik}(p_l; z^{(m)}; \omega; z^{(n)}) \right], \quad (\text{D.44})$$

where $\mathcal{U}_{ik}^G(p_l; z^{(m)}; \omega; z^{(n)})$ and $\mathcal{G}_{ik}(p_l; z^{(m)}; \omega; z^{(n)})$ are given by equations (D.18)-(D.30), and p_l is the center of the p -subintervals (for $l = 1, 2, \dots, P$).

D.2.3 Evaluation of the Diagonal Elements of $\mathbf{A}_{ik}^{(m,m)}$

In order to evaluate the diagonal elements of the Green matrix in which $m = n$, we substitute $m = n$ into equation (D.5), yielding

$$\begin{aligned} \mathbf{A}_{ik}^{(m,m)} &= \omega^2 \Delta \rho_m \\ &\times \int_0^\infty \int_{x_m^-}^{x_m^+} \int_{y_m^-}^{y_m^+} \left[\mathcal{U}_{ik}^G(p; z^{(m)}; \omega; z^{(m)}) - \mathcal{G}_{ik}(p; z^{(m)}; \omega; z^{(m)}) \right] p \, dx \, dy \, dp. \end{aligned} \quad (\text{D.45})$$

We can calculate the integral by approximating the rectangular cells by a circular one with an equivalent radius that gives the same area as the rectangular cells (Richmond, 1965).

It then reads

$$\begin{aligned} \mathbf{A}_{ik}^{(m,m)} &= \omega^2 \Delta \rho_m \\ &\times \int_0^\infty p \int_0^{r_o} \int_0^{2\pi} \left[\mathcal{U}_{ik}^G(p; z^{(m)}; \omega; z^{(m)}) - \mathcal{G}_{ik}(p; z^{(m)}; \omega; z^{(m)}) \right] r \, dr \, d\phi \, dp, \end{aligned} \quad (\text{D.46})$$

with $r_o = \sqrt{\frac{\Delta_x \Delta_y}{\pi}}$ and $0 \leq \phi \leq 2\pi$.

The inner two integrals can then be determined analytically. It yields

$$\begin{aligned} \mathbf{A}_{ik}^{(m,m)} &= \omega^2 \Delta \rho_m \\ &\times \int_0^\infty p \left[\tilde{\mathcal{U}}_{ik}^G(p; z^{(m)}; \omega; z^{(m)}) - \tilde{\mathcal{G}}_{ik}(p; z^{(m)}; \omega; z^{(m)}) \right] dp, \end{aligned} \quad (\text{D.47})$$

where the expression of $\tilde{\mathcal{U}}_{ik}^G(p; z^{(m)}; \omega; z^{(m)})$ is given by

$$\begin{aligned} \tilde{\mathcal{U}}_{11}^G(p; z^{(m)}; \omega; z^{(m)}) &= \frac{\pi}{\omega^2 p^2} \left(V_1(p, z^{(m)}, z^{(m)}) \left[r_o (J_1(\omega p r_o) \omega p - 1) + J_0(\omega p r_o) \right. \right. \\ &\quad \left. \left. (r_o + 1) - 1 \right] + W_1(p, z^{(m)}, z^{(m)}) \left[1 + J_0(\omega p r_o) (1 - r_o) \right. \right. \\ &\quad \left. \left. - r_o (J_1(\omega p r_o) \omega p - 1) \right] \right), \end{aligned} \quad (\text{D.48})$$

$$\begin{aligned} \tilde{\mathcal{U}}_{22}^G(p; z^{(m)}; \omega; z^{(m)}) &= \frac{\pi}{\omega^2 p^2} \left(V_2(p, z^{(m)}, z^{(m)}) \left[r_o (J_1(\omega p r_o) \omega p - 1) - J_0(\omega p r_o) \right. \right. \\ &\quad \left. \left. (1 - r_o) + 1 \right] + W_2(p, z^{(m)}, z^{(m)}) \left[1 - J_0(\omega p r_o) (r_o + 1) \right. \right. \\ &\quad \left. \left. - r_o (J_1(\omega p r_o) \omega p - 1) \right] \right), \end{aligned} \quad (\text{D.49})$$

$$\tilde{\mathcal{U}}_{33}^G(p; z^{(m)}; \omega; z^{(m)}) = \frac{2\pi r_o}{\omega} J_1(\omega p r_o) U_3(p, z^{(m)}, z^{(m)}), \quad (\text{D.50})$$

$$\tilde{\mathcal{U}}_{12}^G(p; z^{(m)}; \omega; z^{(m)}) = \tilde{\mathcal{U}}_{21}^G(p; z^{(m)}; \omega; z^{(m)}) = 0, \quad (\text{D.51})$$

$$\tilde{\mathcal{U}}_{13}^G(p; z^{(m)}; \omega; z^{(m)}) = \tilde{\mathcal{U}}_{31}^G(p; z^{(m)}; \omega; z^{(m)}) = 0, \quad (\text{D.52})$$

$$\tilde{\mathcal{U}}_{23}^G(p; z^{(m)}; \omega; z^{(m)}) = \tilde{\mathcal{U}}_{32}^G(p; z^{(m)}; \omega; z^{(m)}) = 0, \quad (\text{D.53})$$

with V_1, V_2, W_1, W_2 and U_3 correspond to the solution due to the point force $f_j, j = 1, 2, 3$ in equation B.1.

The six independent elements of $\tilde{\mathcal{G}}_{ik}(p; z^{(m)}; \omega; z^{(m)})$ are given by

$$\tilde{\mathcal{G}}_{11}(p; z^{(m)}; \omega; z^{(m)}) = \frac{r_o}{\omega^2 \rho \beta^2} J_1(\omega p r_o) (-2\mathcal{C}_\beta - p^2 \beta^2 (\mathcal{C}_\alpha - \mathcal{C}_\beta)), \quad (\text{D.54})$$

$$\tilde{\mathcal{G}}_{22}(p; z^{(m)}; \omega; z^{(m)}) = \frac{r_o}{\omega^2 \rho \beta^2} J_1(\omega p r_o) (-2\mathcal{C}_\beta - p^2 \beta^2 (\mathcal{C}_\alpha - \mathcal{C}_\beta)), \quad (\text{D.55})$$

$$\tilde{\mathcal{G}}_{33}(p; z^{(m)}; \omega; z^{(m)}) = \frac{2r_o}{\omega^4 \rho \beta^2} J_1(\omega p r_o) (\omega^2 \mathcal{C}_\beta + \beta^2 \omega^2 (q_\alpha^2 \mathcal{C}_\alpha - q_\beta^2 \mathcal{C}_\beta)), \quad (\text{D.56})$$

$$\tilde{\mathcal{G}}_{12}(p; z^{(m)}; \omega; z^{(m)}) = \tilde{\mathcal{G}}_{21}(p; z^{(m)}; \omega; z^{(m)}) = 0, \quad (\text{D.57})$$

$$\tilde{\mathcal{G}}_{13}(p; z^{(m)}; \omega; z^{(m)}) = \tilde{\mathcal{G}}_{31}(p; z^{(m)}; \omega; z^{(m)}) = 0, \quad (\text{D.58})$$

$$\tilde{\mathcal{G}}_{23}(p; z^{(m)}; \omega; z^{(m)}) = \tilde{\mathcal{G}}_{32}(p; z^{(m)}; \omega; z^{(m)}) = 0, \quad (\text{D.59})$$

with

$$\mathcal{C}_\alpha = \frac{1}{2q_\alpha^2} (e^{j\omega q_\alpha \frac{\Delta z}{2}} - 1) \quad , \quad \mathcal{C}_\beta = \frac{1}{2q_\beta^2} (e^{j\omega q_\beta \frac{\Delta z}{2}} - 1), \quad (\text{D.60})$$

and $J_0(\omega p r_o), J_1(\omega p r_o)$ are Bessel functions of orders 0 and 1, respectively.

Finally, the results of $\mathbf{A}_{ik}^{(m,n)}$ and $\mathbf{B}_{ik}^{(m,n)}$ give us the matrix elements of $\mathbf{G}_{ik}^{(m,n)}$ given by equation (2.67). These elements are needed to solve the system in equation (2.56).

Derivation of the Adjoint Operator $\mathbf{G}_{\mathcal{D}}^{\dagger}$

The adjoint operator is defined in equation (4.13). We now show how an expression for the adjoint operator $\mathbf{G}_{\mathcal{D}}^{\dagger}$ is obtained. From equation (4.13), we write

$$\begin{aligned}
 \langle \mathcal{E}, \mathbf{G}_S \sigma \rangle_S &= \int_{\omega \in \mathcal{W}} \int_{\mathbf{x} \in \mathcal{S}} \mathcal{E}(\mathbf{x}) \overline{\mathbf{G}_S \sigma(\mathbf{x})} d\mathbf{x} d\omega, & (E.1) \\
 &= \int_{\omega \in \mathcal{W}} \int_{\mathbf{x} \in \mathcal{S}} \mathcal{E}(\mathbf{x}) \omega^2 \overline{\int_{\mathbf{x}' \in \mathcal{D}} u_k^G(\mathbf{x}, \mathbf{x}') v_k(\mathbf{x}', \mathbf{x}^s) \sigma(\mathbf{x}') d\mathbf{x}' d\mathbf{x} d\omega}, \\
 &= \int_{\omega \in \mathcal{W}} \int_{\mathbf{x} \in \mathcal{S}} \mathcal{E}(\mathbf{x}) \omega^2 \overline{\int_{\mathbf{x}' \in \mathcal{D}} u_k^G(\mathbf{x}, \mathbf{x}') v_k(\mathbf{x}', \mathbf{x}^s) \sigma(\mathbf{x}') d\mathbf{x}' d\mathbf{x} d\omega}, \\
 &= \int_{\omega \in \mathcal{W}} \int_{\mathbf{x}' \in \mathcal{D}} \left[\omega^2 \bar{v}_k(\mathbf{x}', \mathbf{x}^s) \int_{\mathbf{x} \in \mathcal{S}} \mathcal{E}(\mathbf{x}) \bar{u}_k^G(\mathbf{x}, \mathbf{x}') d\mathbf{x} \right] \bar{\sigma}(\mathbf{x}') d\mathbf{x}' d\omega, \\
 &= \langle \mathbf{G}_{\mathcal{D}}^{\dagger} \mathcal{E}, \sigma \rangle_{\mathcal{D}}, & (E.2)
 \end{aligned}$$

such that $\mathbf{G}_{\mathcal{D}}^{\dagger} \mathcal{E}$ is found as

$$\{\mathbf{G}_{\mathcal{D}}^{\dagger} \mathcal{E}\}(\mathbf{x}') = \omega^2 \bar{v}_k(\mathbf{x}', \mathbf{x}^s) \int_{\mathbf{x} \in \mathcal{S}} \bar{u}_k^G(\mathbf{x}, \mathbf{x}') \mathcal{E}(\mathbf{x}) d\mathbf{x}, \quad \mathbf{x}' \in \mathcal{D}. \quad (E.3)$$

List of Symbols

Mathematical Model

$\mathbf{x} = (x_1, x_2, x_3) = (x, y, z)$	spatial coordinates	[m]
H	depth of the scatterer	[m]
W_x	length of the scatterer	[m]
W_y	width of the scatterer	[m]
u_i	particle displacement	[m]
τ_{ij}	stress tensor	[Pa]
f_i	volume force	N/m ³
s_{ijpq}	compliance	[Pa ⁻¹]
v_i	particle velocity	[m/s]
t	time	[s]
ω	angular frequency	[rad/s]
ρ	mass density	[kg/m ³]
$\mathbf{x}^s = (x^s, y^s, z^s)$	source coordinates	[m]
$\mathbf{x}^r = (x^r, y^r, z^r)$	receiver coordinates	[m]
$\mathbf{x}' = (x', y', z')$	scatterer coordinates	[m]
$\Delta\rho, \sigma$	density contrast	[kg/m ³]
$\delta(\mathbf{x})$	Dirac delta function	[m ⁻¹]
p_1, p_2	Cartesian slowness coordiantes	[s/m]
$p = \sqrt{p_1^2 + p_2^2}$	Polar slowness coordinate	[s/m]
\mathcal{D}	scattering domain	
Ω	half space	
\mathcal{S}	free surface	
h_{ij}	deformation rate	
δ_{ij}	Kronecker delta	

$\mathbf{i}_1, \mathbf{i}_2, \mathbf{i}_3$	unit vector	
\mathbf{n}	normal vector	
j	imaginary unit, $j^2 = -1$	
c_S	compressional wave	[m/s]
c_P	compressional wave	[m/s]
c_R	Rayleigh wave	[m/s]
α	compressional wave	[m/s]
β	shear wave	[m/s]
λ, μ	Lamé parameter	[Pa]
λ_s	shear wavelength	[m]
h	layer thickness	[m]
P	number of processors	
P_0	master	
P_s	slave	
$\mathcal{D}^{(n)}$	subdomain of \mathcal{D}	
Δ_x, Δ_y	the width of the subdomain $\mathcal{D}^{(n)}$	
Δ_z	the length of the subdomain $\mathcal{D}^{(n)}$	
superscript l	layer index	
superscript e	embedding medium	
superscript G	Green's state	
superscript m, n	grid point	

Summary

Modeling and inversion of scattered surface waves

Christina Dwi RIYANTI

Seismic waves provide important information on the interior of the Earth which can be used for the exploration of oil and gas or to study the evolution of the Earth, or to predict earth quakes. In seismic exploration, the objective is to obtain a detailed image or map of the sub-surface in order to locate possible hydrocarbon-bearing layers, using information contained in body waves. However, upcoming body waves that have been reflected by deeper layers can be scattered by 3D near-surface heterogeneities directly beneath the surface. This results in a complex interference pattern that can seriously distort the continuity of reflectors. This type of noise is considered one of the factors that diminishes the maximum resolution in seismic images. New acquisition techniques that make it possible to measure the wave field at significantly more locations than in conventional seismic surveys have provided new insight in this scattering process. We present a modeling method for seismic waves that propagate along the surface of the Earth and have been scattered in the vicinity of the source or the receivers. Using this model as starting point, we formulate an inversion scheme to estimate properties of scattering objects close to the surface of the Earth. Therefore, we have two main objectives:

1. to develop an efficient and accurate modeling method for scattering of seismic waves by 3D near-surface heterogeneities close to the receivers or sources;
2. To develop an inversion algorithm to reconstruct scattering-medium parameters from scattered surface waves.

We have chosen a modeling method based on a domain-type integral representation of the wave field. The integral representation of the wave field can be expressed as superposition of the wave field in the background without heterogeneities (the incident wave field) and a term that accounts for the presence of the heterogeneity (the scattered wave field) consisting of the impulse response (Green's tensor) of the embedding, a contrast function and the unknown wave field in the domain occupied by the scatterer. For observation points inside the near-surface heterogeneities, we obtain a domain-integral equation of the second kind. We apply the method of moments to solve this integral equation. To obtain an efficient and accurate method, we use two techniques: first of all, we accelerate the convergence of the computation of the Green's tensor by subtracting the free-space Green's tensor when the observation and the scatterer points are located close to each other. Secondly, we implement the method on a cluster of workstations, where each frequency is computed independently.

From a number of model studies, we conclude that we can accurately model near-surface

scattering effects, which can seriously distort the wave fronts of upcoming reflections. We observe a time delay in the wavefront above the scatterers and also scattered Rayleigh waves. We have compared our modeling method with experimental data collected with similar geometries at the Colorado School Mines (CSM). We found that both results are in a good qualitative and quantitative agreement. We observed in both results that the P wave is delayed above the anomaly. We also observed that most of the body wave energy was converted into scattered Rayleigh waves, causing interference with the body wave.

The final objective of this research was to reconstruct the medium parameters from scattered surface waves. The inversion is based on minimizing an error function consisting of the squared difference between the actual scattered field and the scattered field calculated with our method. We have applied our inversion algorithm to several synthetic data sets computed with the integral-equation method. The model used to generate synthetic data contains a scatterer placed at different depths. Because the Rayleigh wave attenuates with depth, our main interest is to investigate up to what depth we can resolve the model. We find that we can get a good estimate of the contrast function up to a depth of about one Rayleigh wavelength. The computational complexity of our inversion scheme makes it less suitable for inversion of actual data sets. Nonetheless, the results of our inversion studies can be used to assess the validity of approximations made in efficient imaging schemes for scattered surface waves.

Samenvatting

Modellering en inversie van verstrooide oppervlaktegolven

Christina Dwi RIYANTI

Seismische golven bevatten belangrijke informatie over de structuur van de Aarde. Deze informatie wordt gebruikt voor de opsporing van olie, om de evolutie van de Aarde te bestuderen of om aardbevingen te voorspellen. Het doel van seismische exploratie is om met behulp van de informatie in 'body' golven een gedetailleerd beeld van de ondergrond te krijgen om mogelijke olie of gas reserves te lokaliseren. 'Body' golven die door dieper gelegen lagen gereflekteerd zijn en naar boven lopen kunnen echter verstrooid worden door onregelmatigheden vlakbij het oppervlak van de Aarde. Dit leidt tot een interferentie patroon dat de continuïteit van een reflectie ernstig kan aantasten. In het algemeen wordt dit type ruis gezien als een van de redenen die de resolutie in seismische afbeeldingen beperken. Nieuwe acquisitietechnieken hebben het mogelijk gemaakt om het golfveld op veel meer plaatsen te meten dan tot nu toe gebruikelijk was in seismische exploratie. Deze fijnere bemonstering heeft tot nieuwe inzichten in het verstrooiingsproces dichtbij het aardoppervlak geleid. We presenteren een modeleringsmethode voor seismische golven die langs het aardoppervlak propageren en dichtbij de bron of ontvangers zijn verstrooid. Met dit model als uitgangspunt, formuleren we een inversiemethode om eigenschappen van verstrooiingsobjecten in de ondiepe ondergrond te bepalen. Er zijn dus twee doelen:

1. Een efficiënte en nauwkeurige methode om verstrooiing van seismische golven door drie dimensionale onregelmatigheden dichtbij het oppervlak van de Aarde en dichtbij de bron of ontvangers uit te rekenen.
2. Een inversiemethode om parameters van een ondiep verstrooiingsobject te bepalen met behulp van verstrooide oppervlaktegolven.

We hebben voor een modeleringsmethode gekozen die op een domein-integraal representatie van het golfveld is gebaseerd. Het golfveld kan worden uitgedrukt als de som van het golfveld in het achtergrondmedium zonder verstrooiers en een term die het verstrooide veld voorstelt. De integraal-representatie bestaat uit de impulsrespons van het achtergrondmedium (de Greense tensor), een contrastfunctie en het golfveld in het verstrooiingsobject. Als de observatiepositie zich in de verstrooiër bevindt, leidt dit tot een domein-integraal vergelijking van de tweede soort. Om deze vergelijking op te lossen gebruiken we de momenten methode, waarbij het golfveld gediscrètiseerd wordt. We gebruiken twee technieken om deze methode efficiënter te maken met behoud van de nauwkeurigheid: ten eerste versnellen we de convergentie van de

berekening van de Greense tensor door de vrije-ruimte Greense functie van de gelaagde halfruimte Greense tensor af te trekken als de observatiepunten zich in de verstrooiers bevinden. Ten tweede implementeren we ons programma op een cluster van pc's. Hiervoor hebben we onze methode zo ingericht dat we het golfveld per frequentie parallel kunnen uitrekenen.

Uit de bestudering van verschillende voorbeelden concluderen we dat we nauwkeurig de verstrooiingseffecten van ondiepe onregelmatigheden kunnen modelleren. Uit deze voorbeelden blijkt ook dat de verstrooiingseffecten de continuïteit van de naar boven lopende golf aantast. Boven de anomalie ontstaat een tijdverschuiving in het golffront en verstrooide oppervlakte (Rayleigh) golven. We hebben de resultaten verkregen met onze modelleringen, vergeleken met experimentele data gemeten op de Colorado School of Mines (CSM). Uit deze vergelijking blijkt dat de gemodelleerde data zowel kwantitatief als kwalitatief overeenkomen met de data gemeten in het laboratorium. In zowel de numeriek verkregen data als de gemeten data onderscheiden we een vertraging in het (P-) golffront boven de anomalie. Verder stellen we vast dat een groot deel van de 'body' golf energie wordt omgezet in verstrooide (Rayleigh) golven die op hun beurt weer voor interferentie met het golffront zorgen.

Uiteindelijk is het doel van dit proefschrift om parameters van onregelmatigheden dichtbij het oppervlak van de Aarde te bepalen met behulp van verstrooide oppervlaktegolven. We hebben dit inversie-algoritme op data van verschillende modellen toegepast. In deze modellen hebben we de verstrooier op verschillende dieptes geplaatst om de gevoeligheid van het algoritme met betrekking tot de diepte van de anomalie te kunnen onderzoeken. Met behulp van deze tests stellen we vast dat we goede resultaten voor het contrast van de verstrooier krijgen als deze zich minder diep dan een Rayleigh-golflengte van het aardoppervlak bevindt. Aangezien ons inversie-algoritme erg veel rekentijd in beslag neemt is het tot nu toe nog niet erg geschikt voor inversie van velddata. Echter, een toepassing van het algoritme is het testen van verschillende benaderingen in meer efficiënte inversiemethoden voor verstrooide oppervlakte golven.

Acknowledgments

This thesis is the result of four years of work in the Mathematical Physics group of the Delft Institute of Applied Mathematics of Delft University of Technology. It is my pleasure that I have to thank so many people. This thesis would not have been possible without their help and support. Here, I would like to express my sincere thanks to all those who have contributed directly and indirectly to the completion of this thesis.

First of all, I would like to extend my most sincere appreciation to my supervisor Dr. Ir. Gérard C. Herman for his great guidance during my research and for his suggestions, corrections, encouragement and help in bringing this thesis to completion. He has introduced me to the subject of seismics and the application of mathematics in general. Many thanks also go to my promotor, Prof. Dr. Ir. Aad J. Hermans, for his encouragement, careful reading of the manuscript and for his suggestions for improvement.

I would like to thank all the people in the Department of Applied Mathematics. In particular, I thank my officemates Maria and Jelle for the comfortable atmosphere, as well as "the lunch group (Alex, Daria, Svetlana, Remus)" for sharing many stories and discussing the situation in the world during lunch, and for going out in the weekend sometimes to get "fresh air" and to get away from research for a moment. Thanks also go to Asye for very useful discussions, support and suggestions, and to Auke for the Fortran program of the Green's tensor and discussions. I wish to thank Kees Lemmens and Eef Hartman for helping me with computer problems. I would like to thank Kasper van Wijk and John Scales of the Colorado School of Mines for providing the experimental data and Everhard for giving me permission to put the picture of the Schlumberger data in my thesis.

This research has been supported and funded by STW and CICAT. Many thanks go to the committee members of "STW project DTW.4820". From these meetings, I have learned a lot about seismics. In this respect, I would also like to thank to Paul Althuis, Durk Jellema, Rene Tamboer and Manon Post of CICAT TU Delft for smoothly taking care of all the paperwork. I would like to thank the Department of Mathematics at Sebelas Maret University for giving me permission to do this PhD research.

Thanks to all Indonesian students in Delft, all members of "wingkobabat group" and the International Student Chaplaincy, especially Fr. Ben and Rev. Stroh. They have made my stay in Holland feel like home. Thanks go to my housemates Tanti and Dini for their kindness in sharing an appartement and for cooking and having "makan malam" together in the KVZ 160-161's kitchen. Thanks to Diah, Julius and Siti for having shared many experiences in life and thoughts with me throughout the last few years. Thanks to the Campman family for their hospitality, as I really feel it is "gezellig" visiting their house. Bedankt voor alles.

Finally, warmest thanks must go to my parents for their support, praying, understanding and allowing me to come here, and to my brother and his family, my sisters and my nephew and niece. Special thanks go to Xander for his support, encouragement and patience.

Curriculum Vitae

Christina Dwi Riyanti was born in Bantul, Yogyakarta, Indonesia on 12 December 1969. From 1985, she attended secondary school at 'SMA NEGERI I' in Bantul, Yogyakarta, Indonesia, where she graduated in 1988. In the same year, she started her studies at the Department of Mathematics, the Faculty of Mathematics and Natural Sciences, Gadjah Mada University, Yogyakarta, Indonesia and received her Bachelor's degree in 1993. After graduation she joined as a staff member of the Department of Mathematics at the Faculty of Mathematics and Natural Sciences, Sebelas Maret University, Surakarta, Central Java, Indonesia. In September 1997 she obtained a grant of the 'DUE Project' to continue her studies through the Master's program in Applied Mathematics at Bandung Institute of Technology in Bandung, West Java. She finished her Master's degree in October 1999. In February 2000, she visited the Department of Applied Mathematics, Delft University of Technology to do research as part of cooperation between Indonesia and the Netherlands. She worked under the supervision of Dr. Ir. Gérard C. Herman for 4 months. Afterwards, she started her PhD research in September 2000 at the Department of Applied Mathematics, Delft University of Technology with Dr. Ir. Gérard C. Herman and her promoter Prof. Dr. Ir. A.J. Hermans. The research was financed by the Dutch Technology Foundation (STW) in the framework of the project "Techniques for shallow imaging and removal of near-surface effects" (project DTW. 4820). Her work focused on the modeling of the near-field scattering problem and the inversion of scattered surface waves. This research has led to the present Ph.D thesis. She has published several papers in international journals and in proceedings of international conferences.

In March 2005, she started as a post-doctorate researcher at the Numerical Analysis group of the Delft Institute of Applied Mathematics, Delft University of Technology in the project "Rigorous modelling of 3D wave propagation in inhomogeneous media for geophysical and optical problems".

